Petrographic and geochemical characteristics of upper mantle xenoliths of the southwestern United States

by
Jessica C. Cox

An Independent Study Submitted in Partial Fulfillment of the Requirements for
Master of Science in Geology
May, 2003

New Mexico Institute of Mining and Technology
Socorro, New Mexico

Abstract

Upper mantle xenoliths of spinel lherzolite used in this study come from various sites throughout the southwestern U.S. including Potrillo Maar volcanic field, San Carlos, Mt. Taylor volcanic field, Navajo (Four Corners) volcanic field, Grand Canyon, and Lunar Crater Maar. These sites include a variety of tectonic provinces such as the Rio Grande Rift, the Basin and Range, Colorado Plateau, Great Basin, and the transition zones between these. The spinel lherzolites are composed chiefly of olivine, orthopyroxene, clinopyroxene, spinel, and may contain minor amounts of garnet, chromite, and apatite.

Major element geochemical results interpreted in light of experimental studies indicate three groupings based on depth and amounts of melt extraction. The groupings are as follows: Southern Basin and Range xenoliths have less then 20% batch melt extraction with pressures of about 1 GPa; Colorado Plateau and northern Basin and Range xenoliths show 20 – 40% batch melt extraction and pressures up to 4 GPa; and Lunar Crater Maar and San Carlos xenoliths have 30% batch melt extraction and 1 GPa pressure.

The xenoliths are divided into four mantle sources based on their incompatible and rare earth element distributions (REE). Group I shows a strong depletion in the most incompatible elements (and LREE) and is located in the southern Basin and Range and Rio Grande Rift Provinces. Group II shows a progressive depletion as incompatibility increases and is limited to the Mt. Taylor volcanic field in New Mexico. Group III is similar in composition to primitive mantle and it occurs in the southern Basin and Range and Rio Grande Rift Provinces and overlaps regions

covered by Groups I and IV. Group IV shows relative enrichment in the most incompatible elements (and LREE) and occurs in the Great Basin, the Colorado Plateau, and the Basin and Range Provinces. Enrichment / depletion amongst these xenoliths cannot be related to the amount of melt extracted.

Incompatible element distributions and in particular plots based on Ti distribution suggest that xenoliths from Lunar Crater Maar are affected by Ti- metasomatism, and Grand Canyon xenoliths appear to have undergone one or more metasomatic or enrichment events as reflected by their irregular element distributions. There is no evidence for carbonatite metasomatism based on element distributions and Ca/Al and Ti/Eu ratios. The inferred mantle sources of the spinel lherzolite xenolithsare not exclusive to singular sites and singular sites show evidence for multiple mantle sources, such as Kilbourne Hole and San Carlos. Geochemical signatures of xenoliths are variable in samples from the Rio Grande Rift and the southern Basin and Range while signatures from the Colorado Plateau and the Great Basin provinces are rather uniform. There is no clear correlation of xenolith composition to present-day tectonic setting.

Table Of Contents

List of Tables

List of Figures

I: Introduction

In this study, geochemical characteristics of upper mantle xenoliths are used to aid in the characterization of the upper mantle within the southwestern United States. Geochemical characteristics of spinel lherzolites are compared from various xenolith sites in the southwestern United States. Only spinel lherzolites are used due to their being common to many xenolith localities and as a means of standardizing the effects of mineralogy on geochemistry.

This study includes both major element and trace element distributions. Major element studies include ratio comparisons, Al_2O_3 versus other major elements, Mg number studies, and oxide variance diagrams. Trace element studies consist of trace element distributions using both incompatible elements and rare earth elements (REE) normalized to primitive mantle or to average chondrite.

Seventeen samples from nine localities were chosen to include several Tertiary and Quaternary basaltic lava fields and two basaltic dykes. These sites include the Basin and Range Province, the Colorado Plateau Province, the Rio Grande Rift, and the Transition Zone between the Colorado Plateau and the Basin and Range. This allows comparison of results from various modern tectonic settings.

One of the main concerns and problems in these types of geochemical studies is the effects of metasomatism. Metasomatism is the geochemical alteration of a rock generally related to elevated temperatures and the presence of a fluid source that can introduce or

extract various elements from the rock. One problem with metasomatism is recognizing it. As an example, it could appear from the REE distributions that a sample came from an enriched mantle source when in reality it was enriched through secondary mineralization. Another problem with metasomatism is that it can overprint geochemical source signatures. For example, after a rock has been enriched by secondary processes, it is very difficult to distinguish between primary and secondary minerals. Even when the primary and secondary minerals are identified, it is difficult to know if metasomatic alteration has pervasively altered the composition of the primary minerals.

Thin section petrography was used in this study to constrain geochemical variations due to mineralogic differences. Two samples in this study have no spinel, while another has spinel and garnet; these differences are evident in some of the geochemical results. Petrographic analysis also allows recognition of modal metasomatism through the occurrence of secondary minerals such as carbonates or oxides in veins or along grain boundaries.

II: Geologic Setting

Introduction

Mantle xenoliths occur in association with volcanics from many tectonic settings, allowing sampling from several tectonic provinces in the southwestern United States (Rudnick, 1992; Mattie et al., 1997). This study uses seventeen samples collected from nine localities throughout the Southwest (Fig. 1). Samples come from areas that are representative of both athenospheric and lithospheric mantle sources (Livacarri & Perry, 1993). The tectonic provinces that these samples represent are the Basin and Range, the Colorado Plateau, and the Transition Zone (Fig. 2). All localities sampled are common collection sites for upper mantle xenoliths within the Southwest. Table 1 contains sample characteristics such as rock type, sample size, and site characteristics. Samples were chosen on the basis of lithology, being of a sufficient size to allow proper analysis, and a lack of apparent alteration. Appendix A shows geologic maps of the collection sites.

Basin and Range Sites

The formation of the Basin and Range Province (Fig. 2) in the southwestern United States is generally attributed to extensional processes in the last 30 My. The extensional environment is the probable cause for the thinned crust that is 25 – 35 km thick in the southern and central Basin and Range region (Pazzaglia et al., 1999). This area has also experienced a thinning of the lithosphere to less than 80 km (Livicarri & Perry,1989; Roden et al., 1990).

One frequently studied area within the Basin and Range Province is the Rio Grande Rift in south central New Mexico (Fig. 2). Rifting is believed to have commenced at about 32 Ma (Padovani & Reid, 1989). The rift shows recent volcanic activity and magmatism that is related to faulting, basin formation, and high heat flow in the region (Padovani & Reid, 1989). Most of the Rio Grande Rift has average crustal thicknesses of about 40 – 45 km; however the southern rift zone has averages less than 40 km in thickness (Pazzaglia et al., 1999). The southern Rio Grande Rift is part of the southern Basin and Range Province and both continue southeast into Texas and Mexico (Seager & Morgan, 1979; Olsen et al., 1987).

As part of this study, upper mantle xenoliths were sampled from five Tertiary and Quaternary basaltic volcanic fields in the Basin and Range Province (Fig. 2). These sites were chosen for having abundant spinel lherzolite xenoliths.

Potrillo Maar

Potrillo Maar is part of the Potrillo volcanic field located in south-central New Mexico in the southern part of the Rio Grande Rift (Fig. 1 & 2). The Potrillo volcanic field also includes the Afton-Aden basalt field, the West Potrillo Mountains, the Santo Tomas – Black Mountains, as well as Kilbourne and Hunt's Holes (Hoffer, 1971, 1975, 1976). Potrillo Maar borders the western edge of the Rio Grande Rift and occurs along the Fritzgerald – Robledo fault within the Pleistocene La Mesa Surface on the border of Mexico (Chapin, 1971; Reeves & De Hon, 1965; Hawley & Kottlowski, 1969; Hoffer, 1976).

A large variety of both mantle and crustal xenoliths occur at Potrillo Maar. Lower crustal xenoliths include amphibolites and both mafic and felsic, partially melted, granulites (Padovani & Carter, 1977; Scherer et al., 1997). Mantle xenoliths from this locality are mainly spinel lherzolites along with various wehrlites and pyroxenites (Wilshire et al., 1988; Bussod & Williams, 1991). The two samples of spinel lherzolite for this study from Potrillo Maar are PM-1 and PM-2.

Kilbourne Hole

Kilbourne Hole (Fig. 1 & 2) is a maar crater in the Potrillo volcanic field located in the southern Basin and Range Province area west of El Paso (Chapin, 1971). Kilbourne Hole is the most northerly of the maar craters in the volcanic field (Padovani & Reid, 1989). Similar to Potrillo Maar it lies along the Fritzgerald – Robledo fault line (Reeves & De Hon, 1965; Hawley & Kottlowski, 1969; Hoffer, 1976).

Kilbourne Hole contains a variety of crustal and mantle xenoliths similar to those common at Potrillo Maar. Common lithologies for xenoliths in the area include anorthosite, granulite, garnet orthopyroxenite, and spinel lherzolite (Padovani & Carter, 1977; Reid & Woods, 1978). The two spinel lherzolite samples for this study from Kilbourne Hole are KH-1 and KH-2.

Elephant Butte

The Elephant Butte locality is a dyke accessible at a road-cut along Route 51 east of Elephant Butte Dam, near Truth or Consequences, NM (Fig. 1 & 2). It is located in the southern Rio Grande Rift (Wilshire et al., 1988).

The lower crustal xenoliths found at this locality are rare and show high degrees of alteration. The mantle xenoliths from this area are generally spinel lherzolites, augite pyroxenites, and granulites (Baldridge, 1979; Wilshire et al., 1988). The two spinel lherzolite samples for this study from Elephant Butte are EB-1 and EB-2.

Geronimo Volcanic Field

The Geronimo volcanic field is located in southeastern Arizona approximately 20 miles northeast of Douglas, Arizona along Route 80 (Fig. 1 & 2). It is located in a graben in the southern Basin and Range Province near the intersection of San Bernardino Valley and San Simon Valley (Kempton & Dungan, 1989).

Mafic volcanics in the area range in age from 9 Ma to recent and consist of both flows and cinder cones (Kempton et al., 1984). The xenoliths in the area show large variations in composition and both crustal and mantle xenoliths are common (Kempton & Dungan, 1989; Kempton et al., 1990). Lower crustal xenoliths are composed mainly of mafic to intermediate granulites and amphibolites (Kempton et al., 1984). Mantle xenoliths include spinel lherzolites, augite pyroxenites, and lherzolites (some containing kaersutite) (Kempton et al.,

al., 1986). The spinel lherzolite sample for this study from the Thumb, Navajo Volcanic Field is NVFTT-1.

Transition Zone Sites

The Transition Zone is the region between the Colorado Plateau and the Basin and Range or the Rio Grande Rift (Fig. 2). These regions tend to be tectonically active, vary in crustal and lithosperic thicknesses and heat flow, and xenoliths exhibit a large range in geochemical characteristics.

Grand Canyon: Mount Emma

Mount Emma is located near the northern rim of the western Grand Canyon area in northern Arizona (Fig. 1 & 2). Our samples came from a mafic dyke 2.5 miles north of Mount Emma on the Uinkaret Plateau (Best, 1970; Best & Brimhall, 1974). The Transition Zone in this area is between the Colorado Plateau and the southern Great Basin (Best & Brimhall, 1974).

The volcanics along the northern rim of the Grand Canyon are composed of Quaternary basanite and olivine basalt flows, and basaltic cinder cones. These volcanics contain amphibole – bearing mantle xenoliths and megacrysts (Best, 1970, 1974,1975). Mantle xenoliths from the area include wehrlites and lherzolites (Best, 1970). The two spinel lherzolites for this study from Mount Emma are GCME-1 and GCME-2.

Table 1: SW Xenoliths with Localities, Xenolith Axes Length, and Site Characteristics

Locality	Sample#	Rock Type	Minimum Long Axis Length (cm)	Collection Site Characteristics
Potrillo Maar	PM-1	Spinel (garnet) lherzolite	3	Eroded basalt field
	PM-2	Spinel lherzolite	3	
Kilbourne Hole	KH-1	Spinel lherzolite	3	Eroded crater
	KH-2	Spinel lherzolite	4	
Elephant Butte	EB-1	Spinel lherzolite	4	Dyke
	EB-2	Lherzolite	3	
Geronimo VF	GVF-1	Spinel lherzolite	5	Eroded volcanic field
	GVF-2	Spinel lherzolite	3	
Lunar Crater Maar	LCM-1	Lherzolite	3	Eroded basalt field
	LCM-2	Lherzolite	4	
The Thumb	NVFTT-1	Lherzolite	3	Eroded volcanic neck
Mount Emma	GCME-1	Spinel lherzolite	9	Eroded basalt flow
	GCME-2	Spinel lherzolite	9	
San Carlos	SC-1	(Spinel) lherzolite	4	Dyke
Mt. Taylor VF	RPCN-1	Spinel lherzolite	5	Eroded volcanic neck
	RPCN-2	Spinel lherzolite	5	
	RPSR-1	Spinel lherzolite	4	

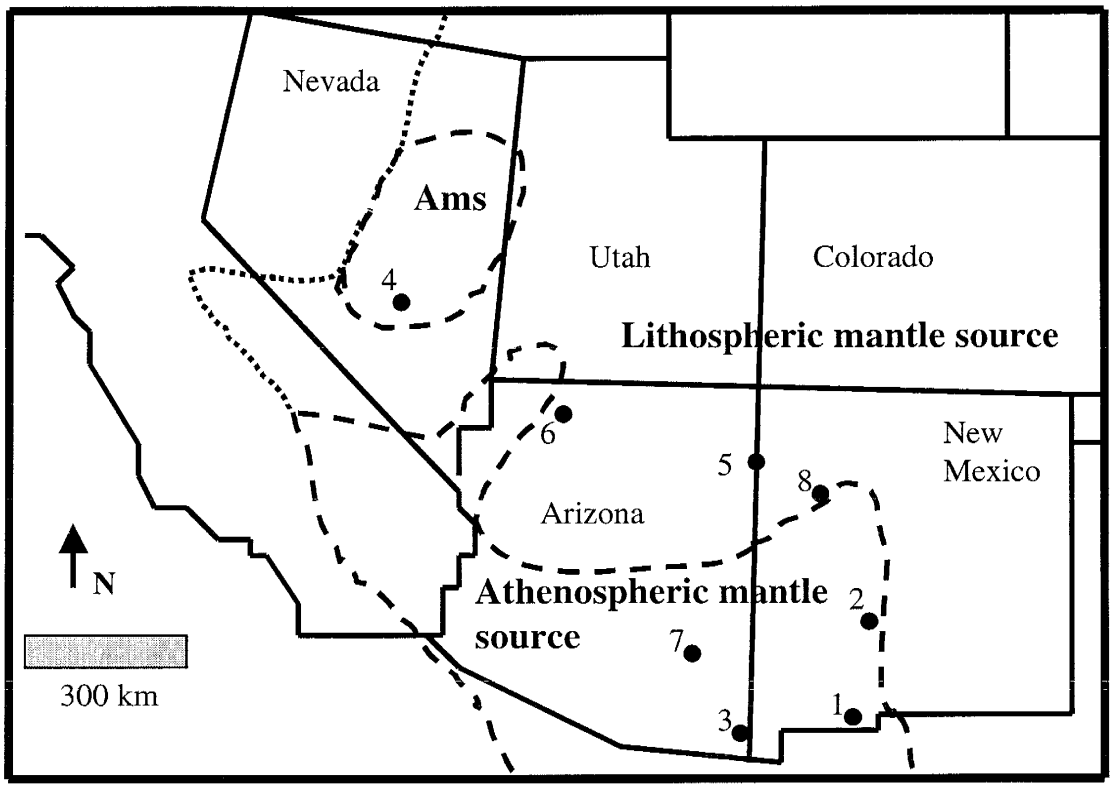

Figure 1: Map of xenolith sites in Southwest United States.
Large dashed lines indicate boundaries of athenospheric mantle source and small dashed lines indicate boundary of lithospheric mantle source Ams is athenospheric mantle source(from Livacarri & Perry, 1993).

1. Potrillo Maar & Kilbourne Hole, Potrillo volcanic field
2. Elephant Butte
3. Geronimo volcanic field
4. Marcath Flow, Lunar Crater Maar
5. The Thumb, Navajo volcanic field
6. Mount Emma, Grand Canyon
7. San Carlos
8. Rio Puerco Necks, Mount Taylor volcanic field

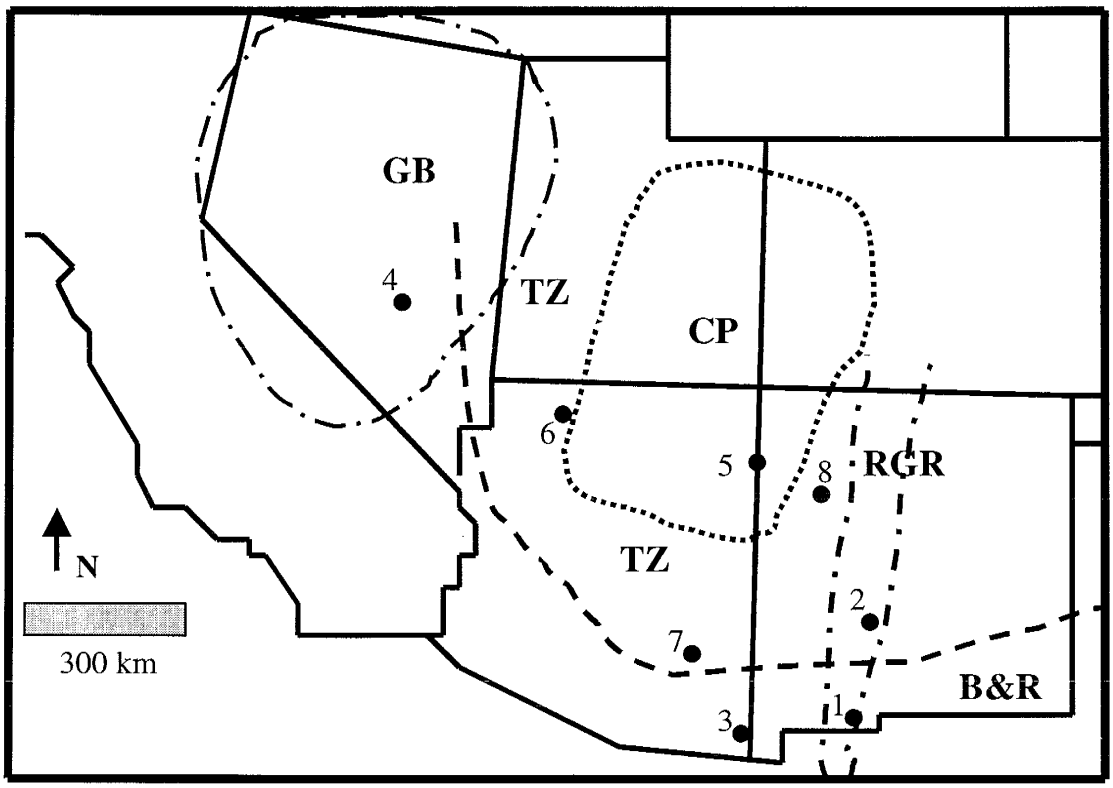

Figure 2: Map of xenolith sites in Southwest United States showing tectonic provinces.
CP = Colorado Plateau, RGR = Rio Grande Rift,
B&R = Basin and Range, GB = Great Basin, TZ = Transition Zone

1. Potrillo Maar & Kilbourne Hole, Potrillo volcanic field
2. Elephant Butte
3. Geronimo volcanic field
4. Marcath Flow, Lunar Crater Maar
5. The Thumb, Navajo volcanic field
6. Mount Emma, Grand Canyon
7. San Carlos
8. Rio Puerco Necks, Mount Taylor volcanic field

1984). The two spinel lherzolite samples for this study from the Geronimo Volcanic Field are GVF-1 and GVF-2.

Lunar Crater: Marcath Flow

The Marcath Flow (which is also known as the Black Rock Summit) is located in the Lunar Crater Volcanic Field (Fig. 1 & 2) in the Pancake Range of south-central Nevada (Trask, 1969). The area consists of a basalt flow surrounded by older Tertiary ignimbrite flows and is located in the center of the southern Great Basin (Scott, 1969; Menzies et al., 1987).

The Marcath flow exhibits a north-northeast trend and ranges in composition from alkaline olivine to subalkaline basalt (Scott, 1969; Scott & Trask, 1971; Pike, 1976; Bergman, 1982; Bergman & Debessy, 1984; Bergman et al., 1981). The Lunar Crater Maar xenolith population contains of suites of cumulates that include gabbros, clinopyroxenites, and anorthosites (Wilshire et al., 1985). Spinel peridotites together with harzburgites, lherzolites, wehrlites, and websterites are only found at the Marcath Flow, the Easy Chair Flow, and the Maggie Eye Flow (Menzies et al., 1987). For this study the two spinel lherzolite samples from the Marcath Flow, Lunar Crater Maar are LCM-1 and LCM-2.

Colorado Plateau Site

The Colorado Plateau extends from the Uinta Mountains in the north to central Arizona in the south. On the west and south it is surrounded by the Basin and Range Province and part of the eastern margin is the Rio Grande Rift (Fig. 2). Uplift of the Plateau is thought to have

occurred during the Quaternary in response to normal faulting along its margins (Cross & Pilger, 1978; Christiansen & Lipman, 1972). The Colorado Plateau is generally believed to be underlain by Proterozoic Basement (1.4 –1.8 Ga) (Condie, 1982; De Paolo, 1981; Alibert et al., 1986). Colorado Plateau lithospheric thicknesses range from 80 to 100 km. However, at the time volcanism was active in the Navajo Volcanic Field the lithosphere may have been up to 120 km thick (Roden et al., 1990; Bodell & Chapman, 1982; Thompson & Zoback, 1979; Chapman & Pollock, 1977).

Navajo Volcanic Field: The Thumb

The Navajo Volcanic Field occurs in NE Arizona and adjacent areas in Utah and New Mexico (Laughlin & Charles, 1992). It is a highly eroded volcanic field, located within the Colorado Plateau Province that erupted between 28 and 19 Ma (Laughlin & Charles, 1992). The Thumb is one of many volcanic necks located in the Navajo Volcanic Field on the Navajo Reservation near the Four Corners area, along the Arizona and New Mexico border (Fig. 1 & 2).

Volcanic centers in the Navajo Volcanic Field are of two types: most generally, minette diatremes such as Shiprock, Agathla Peak and the Thumb; and more infrequently, serpentized ultramafic breccias (kimberlite-like bodies) (Menzies et al., 1987). There are both crustal and mantle xenoliths that occur in the Navajo Volcanic Field, but crustal xenoliths are more common. The Thumb is a minette diatreme. The known upper mantle xenoliths from the Thumb include both garnet and spinel lherzolites (Mercier, 1977; Ehrenberg, 1982; Alibert et

San Carlos

San Carlos is located about 20 miles east of Globe, Arizona on Peridot Mesa within the San Carlos Apache Reservation (Frey & Prinz, 1978). The San Carlos volcanic field is within the transition zone between the Colorado Plateau and the Southern Basin and Range Provinces of east-central Arizona (Fig. 1 & 2).

Peridot Mesa is about 3 km in diameter and is covered by 3 to 6 m thick Tertiary or Quaternary lava from a basalt flow erupted from a cone in the SW corner of the San Carlos volcanic field (Frey & Prinz, 1978). Mantle xenoliths in the area include kaersutite-bearing pyroxenites and wehrlites, spinel lherzolites, websterites, and orthopyroxenites (Frey & Prinz, 1978). The spinel lherzolite sample for this study from the San Carlos volcanic field is SC-1.

Rio Puerco Necks: Cerro Negro & Santa Rosa

The Rio Puerco volcanic necks are part of the Mount Taylor volcanic field west of Albuquerque, New Mexico that erupted at approximately 2.7 Ma (Hallet, 1992). The Mount Taylor volcanic field is located within the transition zone between the Colorado Plateau Province and the Rio Grande Rift (Fig. 1 &2).

In the Mount Taylor volcanic field, about 60% of the necks bear xenoliths, mostly mantle but some crustal xenoliths (Hallet, 1992). The mantle xenoliths include lherzolites, websterites, dunites, harzburgites, and various pyroxenites; however spinel lherzolites are most common (Hallet, 1992). Samples RPCN-1 and RPCN-2 were collected from the Cerro

Negro Volcanic Neck that is located near Cibola County Route 1. The Santa Rosa Volcanic Neck is located on the L-Bar Ranch was the collection site for sample RPSR-1.

III: Petrography

Introduction

Thin sections were made for the seventeen samples used in this study and they are listed in Table 2 along with their locations. The xenolith samples are all either spinel lherzolite or lherzolite; the basic mineralogy of the samples is olivine, ortho- and clinopyroxene, and accessory minerals such as spinel, garnet, and opaques. The samples are divided into two classes based on their textural characteristics: granular and deformed. There are nine granular samples and eight deformed samples. The deformed class is subdivided into two subclasses: structurally deformed and compositionally deformed. The general characteristics of the basic xenolith types are given below, while thin section specifics are given in Appendix B.

The classification of xenoliths is based on textures in thin section. The textures are either primary as seen in the granular samples, or secondary as seen in the deformed samples. Structurally deformed xenoliths exhibit evidence for physical deformation, such as grain size variation or recrystallization of mineral grains. Compositionally deformed xenoliths exhibit compositional banding or preferential mineral clustering. Equilibrium triple junctions and a lack of structural or compositional deformation characterize granular xenoliths.

Table 2: SW Xenolith Samples with Textural Class and Modal Amount of Spinel

Sample #	Locality	Xenolith Textural Class	% Spinel
PM-1	Potrillo Maar	Granular	5
PM-2	Potrillo Maar	Structurally Deformed	<5
KH-1	Kilbourne Hole	Granular	3
KH-2	Kilbourne Hole	Granular	<5
EB-1	Elephant Butte	Granular	<5
EB-2	Elephant Butte	Granular	0
SC-1	San Carlos	Granular	<2
NVFTT-1	Navajo Vol. Field	Compositionally Deformed	0
LCM-1	Lunar Crater Maar	Compositionally Deformed	<1
LCM-2	Lunar Crater Maar	Compositionally Deformed	<1
GVF-1	Geronimo Vol. Field	Structurally Deformed	<5
GVF-2	Geronimo Vol. Field	Granular	3
GCME-1	Grand Canyon	Granular	<4
GCME-2	Grand Canyon	Compositionally Deformed	<4
RPCN-1	Mt. Taylor Vol. Field	Compositionally Deformed	<4
RPCN-2	Mt. Taylor Vol. Field	Granular	<4
RPSR-1	Mt. Taylor Vol. Field	Structurally Deformed	<4

Granular Xenoliths

Introduction

The granular xenoliths are characterized by equilibrium triple junctions (crystal grains formed simultaneously resulting in 120° angles on grain boundaries) and a lack of deformation (Microphoto#1). These xenoliths have poikiloblastic pyroxene grains containing both pyroxene and olivine inclusions (larger crystal grains that postdate and surround smaller crystals and have undergone later metamorphism). Decompression reaction rims and grain size variance are also common among these rocks. Decompression reaction rims may occur around both olivine and pyroxene grains and seem to be the same mineral as the host grain (Microphoto#2). Although the reaction rims are in optical continuity, they appear to have experienced deformation and alteration (which may involve the inclusion of secondary minerals).

Primary Minerals

The primary modal distributions range from 45 – 60% olivine, 15 – 40% orthopyroxene, <5 – 23% clinopyroxene, and 0 –5% spinel. Secondary minerals include various amounts of carbonate, opaques, serpentine, and garnet, that totally constitute up to 5%. In some cases spinel is secondary. The olivine (1/2 – 1/4 cm long axis length) tends to have fractures, twins, and sometimes shows poikiloblastic texture with pyroxene and spinel inclusions. Some olivine grains have decompression reaction rims (Microphoto#2). Orthopyroxene (1/2 – 1/4 cm) exhibits fracturing, twinning, and some grains show exsolution (a sign of slow cooling). Orthopyroxene grains are commonly poikiloblastic, and some grains have decompression reaction

rims. Clinopyroxene (1/2 – 1/4 cm) commonly has fractures and twinning, and some grains have poikiloblastic texture. Spinel ($\leq$ 1/4 cm) generally occurs as intercumulus grains (Microphoto#3), inclusions, or as fracture fill. Intercumulus grains are characteristic of spinel (in this case) crystallizing out of the melt after the other mineral grains had already formed.

Secondary Minerals

The secondary features in the granular xenoliths include micro-fractures, fracture veining (Microphoto#4), alteration along grain boundaries (Microphoto#5), pseudomorphic replacement of olivine by serpentine, and melt inclusions (Microphoto#6). Micro-fractures are small (less than 1 mm across) and they are restricted to solitary grains and generally widespread throughout many of the samples. Larger-scale ($\geq$ 1 mm across) fracture veining occurs across grain boundaries; fractures are filled with secondary minerals such as carbonate, oxides, and silicate phases. These fracture-filled veins appear to be the most recent alteration in the xenoliths. EB-1 shows a fracture vein that contains two phases of carbonate crystallization: a clean $CaCO_3$ and then a Mg-rich spherule-bearing carbonate that may be related to a carbonate melt (Microphoto#7) (Ionov et al., 1993). Fluids traveling along grain boundaries produce alteration and fine grain retrograde minerals. Pervasive fluid flow within a sample can result in pseudomorphic replacement of mineral grains by retrograde minerals such as serpentine. Based on the morphology, most of the inclusions are probably melt inclusions due to their frequency, general aligned arrangement, and irregular shape (Microphoto#6), though some may be

secondary fluid inclusions. The inclusions are small and form lineations along micro-fractures and crystal planes; this is indicative of melt inclusions. Fluid inclusions tend to be circular or oval in thin section.

Deformed Xenoliths

Introduction

The deformed xenoliths are of two types: compositionally deformed and structurally deformed. Compositionally deformed xenoliths exhibit either compositional banding or clustering of primary minerals (Microphoto#8). The structurally deformed xenoliths show either alignment of mineral grains and/or deformational banding.

Compositionally Deformed Xenoliths

Introduction

The compositionally deformed xenoliths (Samples RCPN-1, GCME-2, NVFTT-1, LCM-1, and LCM-2) are characterized by banding in which olivine and pyroxene segregate into bands. Some xenoliths show clustering of spinel grains (Microphoto#8). Compositionally deformed xenoliths show the highest frequency of twinned minerals grains among olivine and the pyroxenes. They also tend to show poikiloblastic texture, equilibrium triple junctions, and some decompression reaction rims.

Primary Minerals

The primary modal distributions in the compositionally deformed xenoliths range from 60 – 65% olivine, 10 – 25% clinopyroxene, and 5 – 25% orthopyroxene. Two samples (RPCN-1 & GCME-2) have about 5% spinel (the remaining have only up to three spinel grains per thin section, therefore < 1% spinel per thin section), and minor primary opaques. Secondary minerals consist collectively of up to 5% carbonates, sericite, opaques, and a clear isotropic mineral as yet unidentified. The olivine (>1 – 1/4 cm long axis length) often shows fractures, twinning, and poikiloblastic texture with included pyroxenes. Clinopyroxene (1/2 – 1/4 cm) exhibits fracturing, twinning, and poikiloblastic texture with olivine and pyroxenes included. Orthopyroxene (1/2 – 1/4 cm) shows fractures, twinning, exsolution, and poikiloblastic texture with included olivine and pyroxenes. Spinel (~1/4 cm) occurs clustered generally within the pyroxene rich bands and as intercumulus grains.

Secondary Minerals

Secondary minerals in the compositionally deformed xenoliths include carbonate, sericite, opaques, and a clear isotropic mineral species. Carbonate in samples RPCN-1, LCM-1, and LCM-2 occurs in various modes such as in micro-fractures within singular grains, within larger- scaled fracture veining, and along grain boundaries. Sericite retrograde alteration occurs within fracture veins in sample RPCN-1. Sericite retrograde alteration tends to be associated with low temperature and pressure regimes with ample fluids for chemical alteration, transportation, and deposition. In general, opaques tend to be either sulfides or oxides (however, they are hard to distinguish

without using reflected light). In some of these samples (LCM-2 and RPCN-1), the opaques are secondary due to their occurrence in the fracture veins and along grain boundaries. There is evidence for possible secondary fluid inclusions or melt inclusions in samples LCM-2 and RPCN-1. The fluid inclusions have a high frequency and occur in a linear manner as one would expect from secondary fluid inclusions or melt inclusions; primary fluid inclusions would more likely be solitary, larger in size, and only occur along crystal growth planes. Possible fluorite occurs in sample RPCN-1. The phase exhibits isotropy and some grains have a cubic crystal habit (<1/4 cm) and only occur in larger fracture veins.

Structurally Deformed Xenoliths

Introduction

The structurally deformed xenoliths exhibit two types of deformation: long axes alignment (samples PM-2 & GVF-1) (Microphoto#9) or deformational banding (RPSR-1). Long axes alignment refers to elongated minerals resulting from deformation. Alignment of both olivine and pyroxene grains are observed in the xenoliths. Banded zones of recrystallized grains characterize deformational banding. The bands are up to 1 cm thick and show little or no compositional banding. The structurally deformed xenoliths show more decompression reaction rims than the other xenolith classes, less poikiloblastic textures, variation in grain boundary style, and no compositional differentiation.

Primary Mineralogy

The modal distributions of the structurally deformed xenoliths range from 50 – 60% olivine, 10 – 35% orthopyroxene, and 10 – 20% clinopyroxene. In addition the xenoliths contain up to 5% spinel, and 0 – 5% combined secondary minerals such as carbonate, opaques, quartz, and spinel. Olivine (1 – 1/4 cm long axis length) is commonly fractured, contains decompression reaction rims, shows twinning, and in some cases has poikiloblastic texture with pyroxenes included. Orthopyroxene (1/2 – 1/4 cm) is also fractured, shows decompression reaction rims, has twinning, exhibits exsolution, and has poikiloblastic texture with olivine and pyroxenes included. Clinopyroxene (1/2 – 1/4 cm) exhibits fracturing, decompression reaction rims, and twinning. Spinel (generally 1/4 cm) occurs as intercumulus grains, veins, and within pyroxene grains.

Secondary Minerals

Secondary minerals present in the structurally deformed xenoliths include carbonates and opaques. Sample RPSR-1, the sample bearing deformational banding, shows the greatest amount of secondary mineralization among the samples in this group. It exhibits a zone of pervasive carbonate alteration (Microphoto#10). The carbonate appears to partially replace primary mineral grains, in some cases may completely replace primary mineral grains. RPSR-1 also has opaques (likely oxides) along grain boundaries (Microphoto#11) and in larger-scale fracture veins. Samples RPSR-1 and PM-2 also contain possible secondary fluid or melt inclusions in olivine

and pyroxenes. Sample GVF-1 has melt pockets of glass within vein-like structures (Microphoto#12).

Photomicrographs

Photomicrographs that follow were taken with conventional 35mm camera photomicrograph equipment and then scanned in and printing was added digitally.

Abbreviations for the printing on the photos are as follows:

ol = olivine, px = pyroxene, opx = orthopyroxene, cpx = clinopyroxene, alt = alteration, sp = spinel, carb = carbonate, rt = rutile, rxn rim = reaction rim, ox = oxide, and gl = glass.

IV: Geochemical Results

Introduction

The geochemical results for this study were made using X-ray fluorescence for major elements and ICP mass spectrometry for trace elements. The detectability limits of the trace and major elements for the geochemical processes used for elemental determination are given in Table 3. The procedures for both techniques are included in Appendix C and major and trace element data are in Appendix D.

Major Elements

Magnesium Number

The Mg number (Mg # = Mg / (Mg + Fe)) is a molar ratio generally used with peridotites as a measure of depletion (Lee et al., 2001). Depletion refers to the composition of a rock after a portion of melt has been extracted (thus leaving the system restitic in nature). The Mg # is basically an inverse measure of the amount of Fe left in the rock after a melt has been extracted since Fe is more likely to enter the melt than Mg as a result of the melt sequence for minerals in which Fe and/or Mg are commonly housed (Lee et al., 2001). Iron-rich minerals generally enter the melt before the Mg-rich mineral species. Figure 3 shows the distribution of Mg #'s among the SW xenoliths. On the graph, the higher the Mg # the more restitic the sample (for example, a sample without any Fe would be most restitic and would have a Mg # = 100%). Samples from the Colorado Plateau and surrounding Transition Zone are most restitic while southern Basin and Range samples are least restitic. Samples plot on each side of the accepted value for primitive mantle (Sun & McDonough, 1989) and all values plot above the value for the convecting mantle (athenosphere).

Table 3: Detectability Limits for Major and Trace Elements

Provided by Quainli Xie, Department of Geological Sciences, University of Saskatchewan

Major Element	Limit (wt.%)	Trace Element	Limit (ppm)
SiO_2	0.01	Rb	0.154
TiO_2	0.001	Ba	0.093
Al_2O_3	0.01	Th	0.006
Fe_2O_3	0.01	Nb	0.004
MgO	0.01	Ta	0.001
CaO	0.01	La	0.004
Na_2O	0.01	Ce	0.01
K_2O	0.01	Nd	0.02
MnO	0.01	Zr	0.013
P_2O_5	0.01	Sm	0.018
		Hf	0.01
		Eu	0.01
		Gd	0.019
		Tb	0.005
		Dy	0.004
		Ho	0.004
		Er	0.01
		Yb	0.009
		Lu	0.005
		Pr	0.003
		Tm	0.002

Al_2O_3 Comparisons

One method to evaluate chemical variation is comparisons showing relationships between various major elements and with trace elements. These graphs are commonly used to show the effects of partial melting and fractional crystallization (Weichert et al., 1997). However, it is also possible to observe the effects of alteration from data points that do not correspond with expected magmatic trends.

Al_2O_3 versus Mg# (Fig. 4a) shows a relatively consistent negative correlation as Al_2O_3 drops the Mg# increases. The xenoliths containing little or no modal spinel show the highest Mg# and the lowest Al_2O_3. PM-1, the xenolith bearing garnet, has the lowest Mg# and the highest percentage of Al_2O_3. GVF-1 has an anomalously low Mg# for its Al_2O_3 and does not fit the trend formed by the other xenoliths.

In the Al_2O_3 versus FeO plot (Fig. 4b), the values generally correlate in a positive linear trend. The linear trend is likely due to pyroxene content since the trend increases as olivine decreases and pyroxenes can house Al and Fe. There are three exceptions to the linear trend. These samples plot with higher FeO values than expected from their Al_2O_3 content. The Lunar Crater Maar xenoliths contain secondary oxide that may be affecting the FeO. San Carlos is the other sample grouped with the Lunar Crater Maar samples. PM-1 lies along the trend of the majority of xenoliths but elevated in both Al_2O_3 and FeO, probably due to the presence of garnet that implies this sample is less restitic then the majority of the xenoliths.

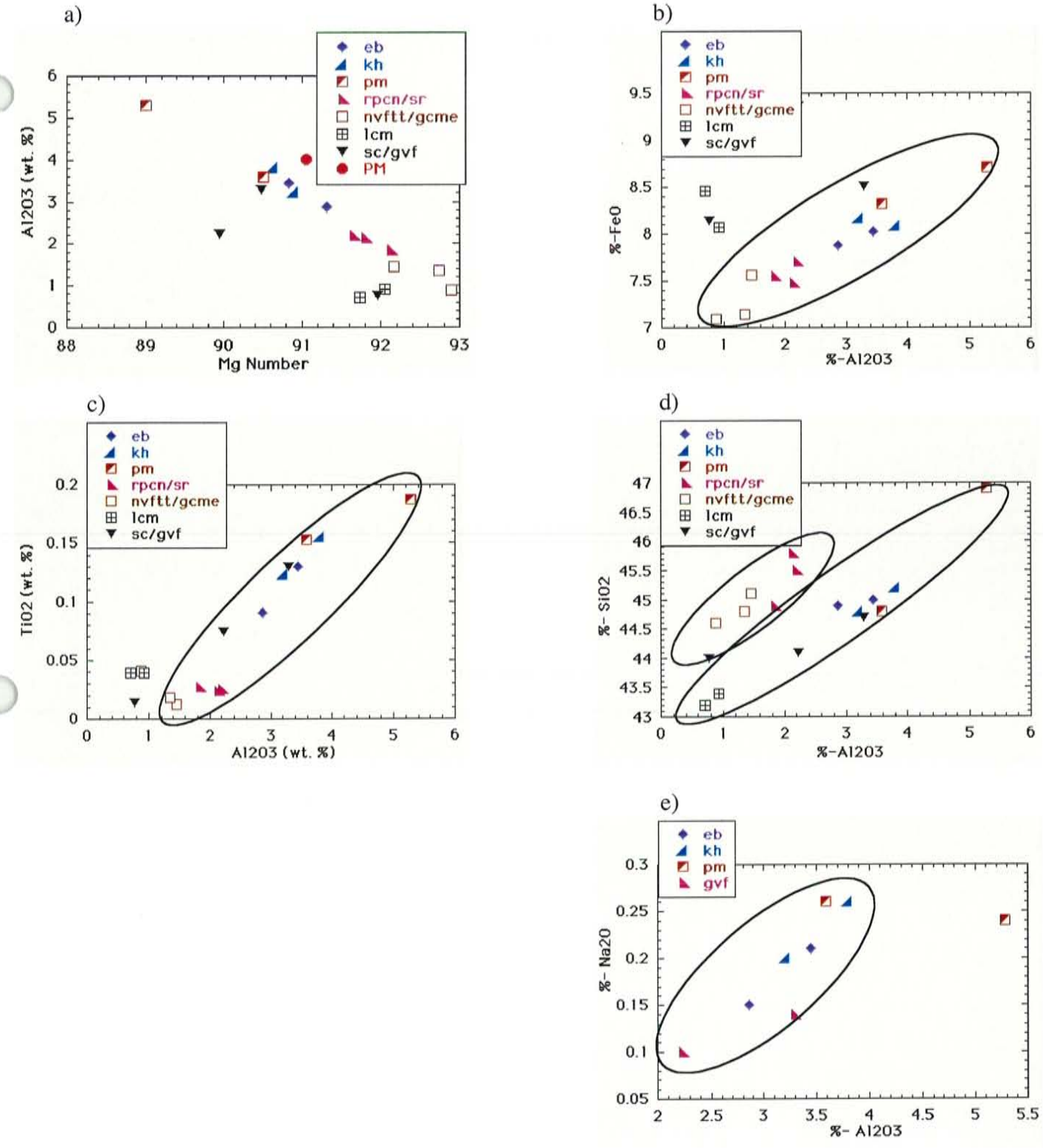

Figure 4: Al_2O_3 weight percent diagrams of major elements.
Discussed trends are circled for clarity.

eb = Elephant Butte, kh = Kilbourne Hole, pm = Potrillo Maar
rpcn/sr = Rio Puerco Necks, nvftt = The Thumb
lcm = Lunar Crater Maar, sc = San Carlos
gvf = Geronimo Volcanic Field
PM = primitive mantle

The Al_2O_3 versus TiO_2 plot (Fig. 4c) exhibits a generally positive correlation among most of the samples. The linear trend is due to clinopyroxene content, the xenoliths with the lowest olivine content have the highest Al and Ti values due to increased clinopyroxene content; and clinopyroxenes house Al and Ti. Three samples have values for Al_2O_3 higher than expected from their TiO_2. Conversely, three other samples have elevated TiO_2 compared to their Al_2O_3. The Lunar Crater Maar xenoliths have secondary oxides that may be affecting their whole rock TiO_2. The Navajo xenolith lies in a group with Lunar Crater Maar and San Carlos, which lies off of the trend formed by the majority of the xenoliths. PM-1 lies of the trend of the other xenoliths as it is relatively enriched in both Al_2O_3 and TiO_2, probably due to being less restitic then the other xenoliths.

On the Al_2O_3 versus SiO_2 plot (Fig. 4d), the data suggest two trends. The samples with higher SiO_2 to Al_2O_3 ratios are from the Colorado Plateau and surrounding Transition Zone. Whereas, the samples with lower SiO_2 to Al_2O_3 ratios are from the Basin and Range Province.

The Al_2O_3 versus Na_2O plot (Fig. 4e) shows a positive linear trend for most of the xenoliths. Most xenoliths, however, have Na_2O values below the detectability level. Sample PM-1 contains greater Al_2O_3 due to its garnet content.

Trace Elements

Introduction

Normalized incompatible or rare earth elemental distribution graphs are produced by normalizing trace element (ppm) data against a common accepted value for a possible source material such as primitive mantle (PM), mid ocean ridge basalt (N-MORB), or chondrites. These graphs are commonly used to depict various enrichment or depletion of trace element groupings such as rare earth elements (REE), which can be light rare earth elements (LREE), middle rare earth elements (MREE), or heavy rare earth elements (HREE), or large ion lithophile elements (LILE). The elements are arranged in order of their relative incompatibilities. The most incompatible elements are those most likely to go into a melt. These graphs are set up in such a manner that the most incompatible elements are on the left side of the graph and progress towards the least incompatible elements on the right side of the graph.

Incompatible Element and Rare Earth Element Distributions

The incompatible element distributions (Fig. 5) show the xenoliths normalized values for incompatible elements ranging from Rb to Lu with Na added to the right to aid in evaluation of certain metasomatic styles. Primitive mantle normalized graphs (PMn) presented are normalized to primitive mantle values from Sun and McDonough (1989) and the relative incompatibilities are similar to those from Ionov et al. (1993) and Wood (1979). The rare earth element distributions (Fig. 6) are normalized to chondrite values from Haskin (1969).

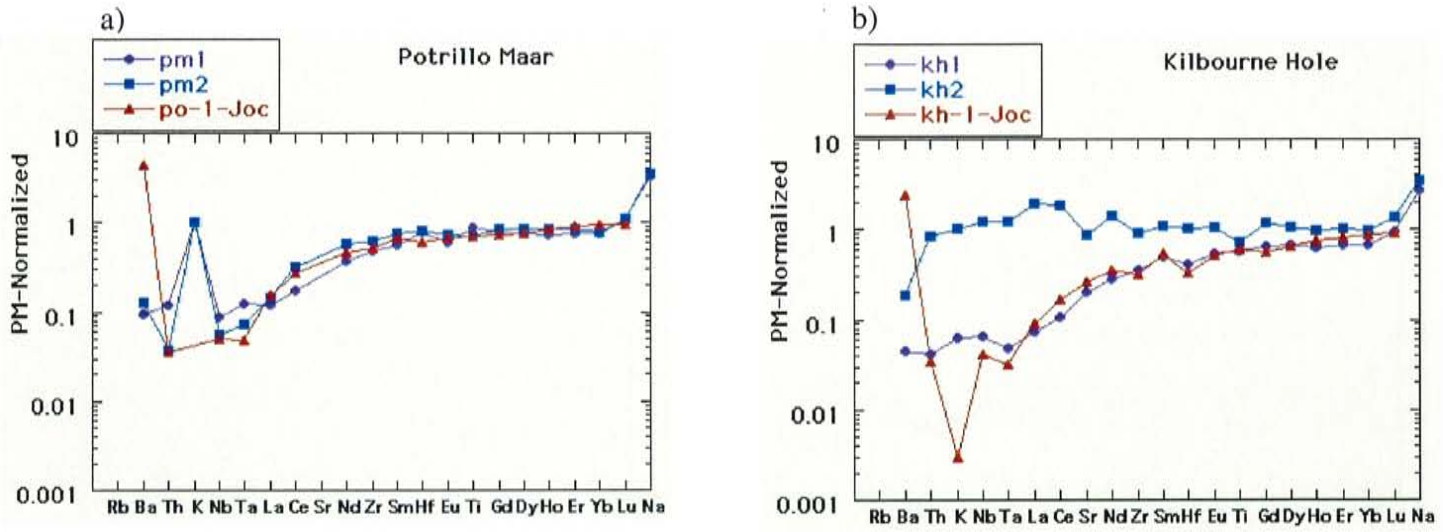

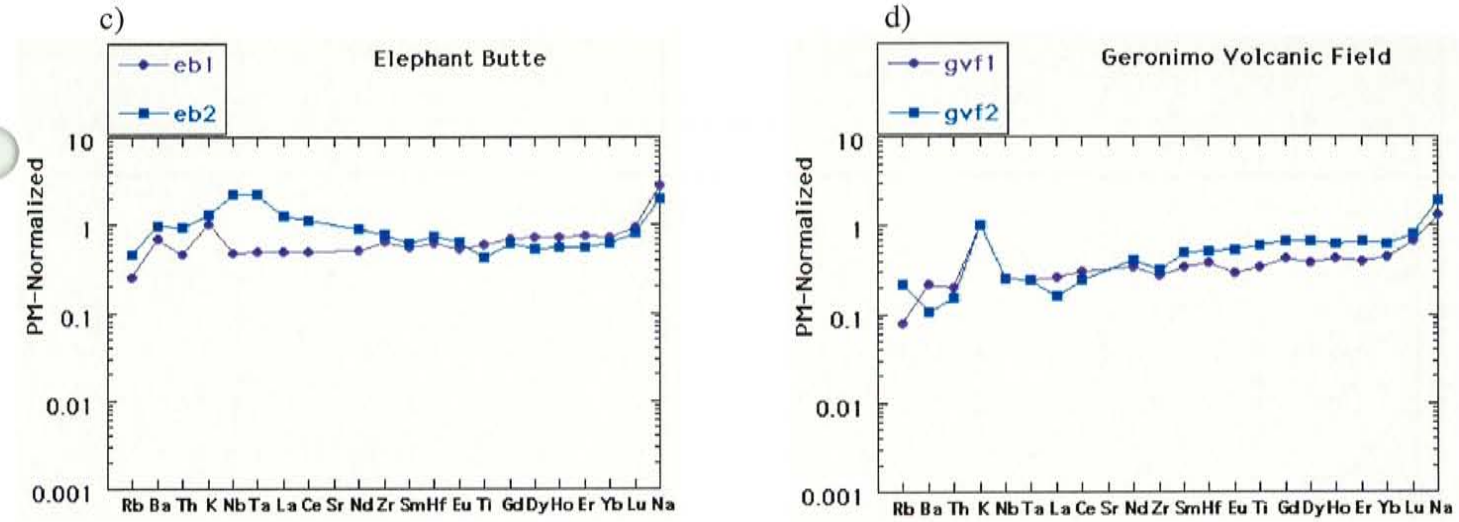

Figure 5: Incompatible element distributions. PM-Normalized with values from Sun and McDonough (1989)

Southern Basin and Range

a) pm1 &2 = Potrillo Maar, po-1-Joc = Potrillo Maar, Jochum et al., 1989
b) kh1 & 2 = Kilbourne Hole, kh-1-Joc = Kilbourne Hole, Jochum et al., 1989
c) eb1 & 2 = Elephant Butte
d) gvf1 & 2 = Geronimo Volcanic Field

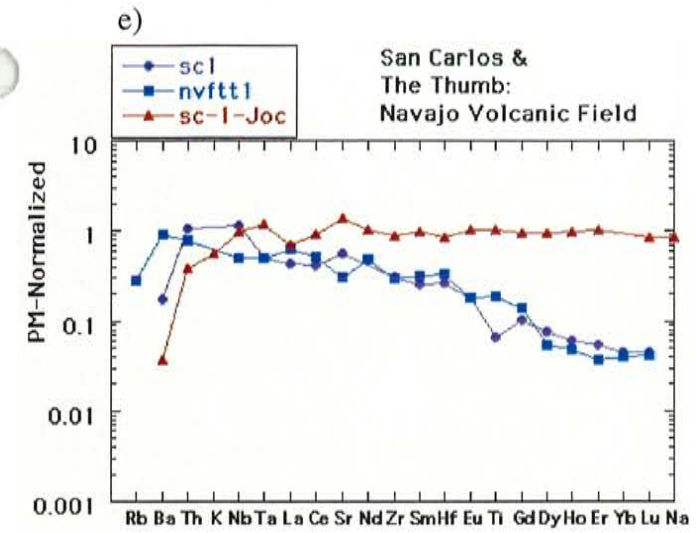

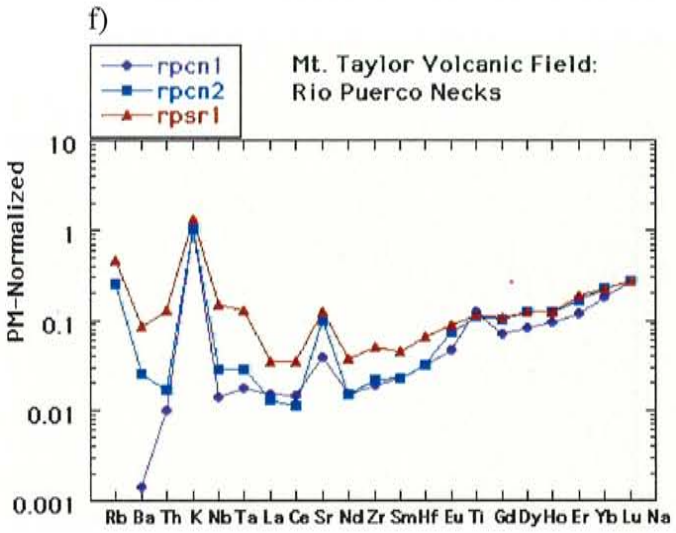

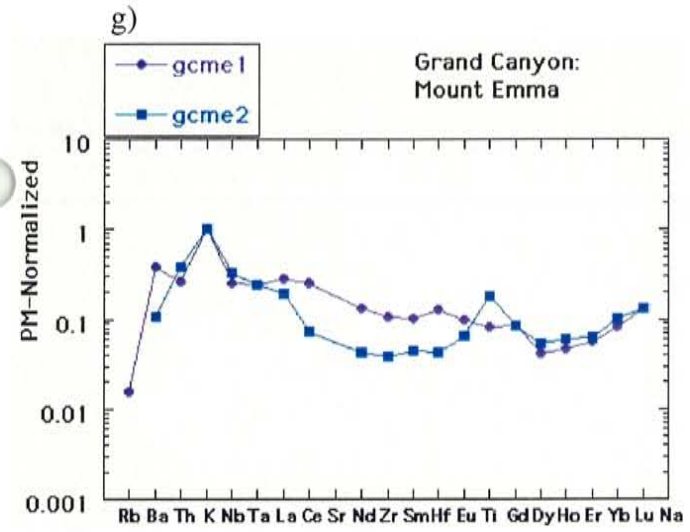

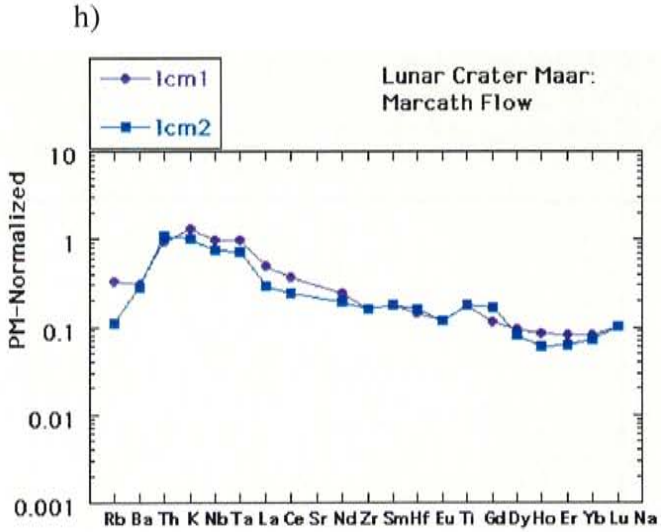

Figure 5 (continued): Incompatible element distributions. PM-Normalized with values from Sun and McDonough (1989)

Colorado Plateau and adjacent Transition Zone

e) nvftt1 = The Thumb, sc1 = San Carlos & sc-1-Joc = San Carlos Jochum et al., 1989

f) rpcn1 & 2 = Rio Puerco: Cerro Negro, rpsr1 = Rio Puerco: Santa Rosa

g) gcme1 & 2 = Grand Canyon: Mount Emma

h) lcm1 & 2 = Lunar Crater Maar: Marcath Flow

Within- Site Comparisons

Potrillo Maar

There are three samples available for Potrillo Maar (Fig. 5a), two collected for this study and a third sample from Jochum et al. (1989). These samples all show a very similar trend marked by a general depletion in the most incompatible elements. There are positive potassium anomalies in the samples collected for our study. These anomalies may not be real, however, since the values for potassium are low and near the detectability level (Table 3). Jochum et al. (1989) did not report potassium values, but their sample does have a positive Ba anomaly.

The REE distributions (Fig. 6a) are very similar for the xenoliths analyzed from Potrillo Maar. They are all relatively strongly depleted in LREE and show slight negative Eu anomalies.

Kilbourne Hole

There are also three samples available from Kilbourne hole (Fig. 5b), two collected for this study and a third sample from Jochum et al. (1989). There are two distinct trends in the incompatible elements at Kilbourne Hole. Sample KH-1 and the Jochum et al. (1989) sample show a relative depletion in the most incompatible elements. Th eJochum et al. sample shows a positive Ba and a negative K anomaly. Both of these samples have negative Hf anomalies. KH-2 has an incompatible element distribution close to that of primitive mantle. This sample however, shows some anomalies such as negative Ba and Ti anomalies, and positive Ta – La and Sr anomalies.

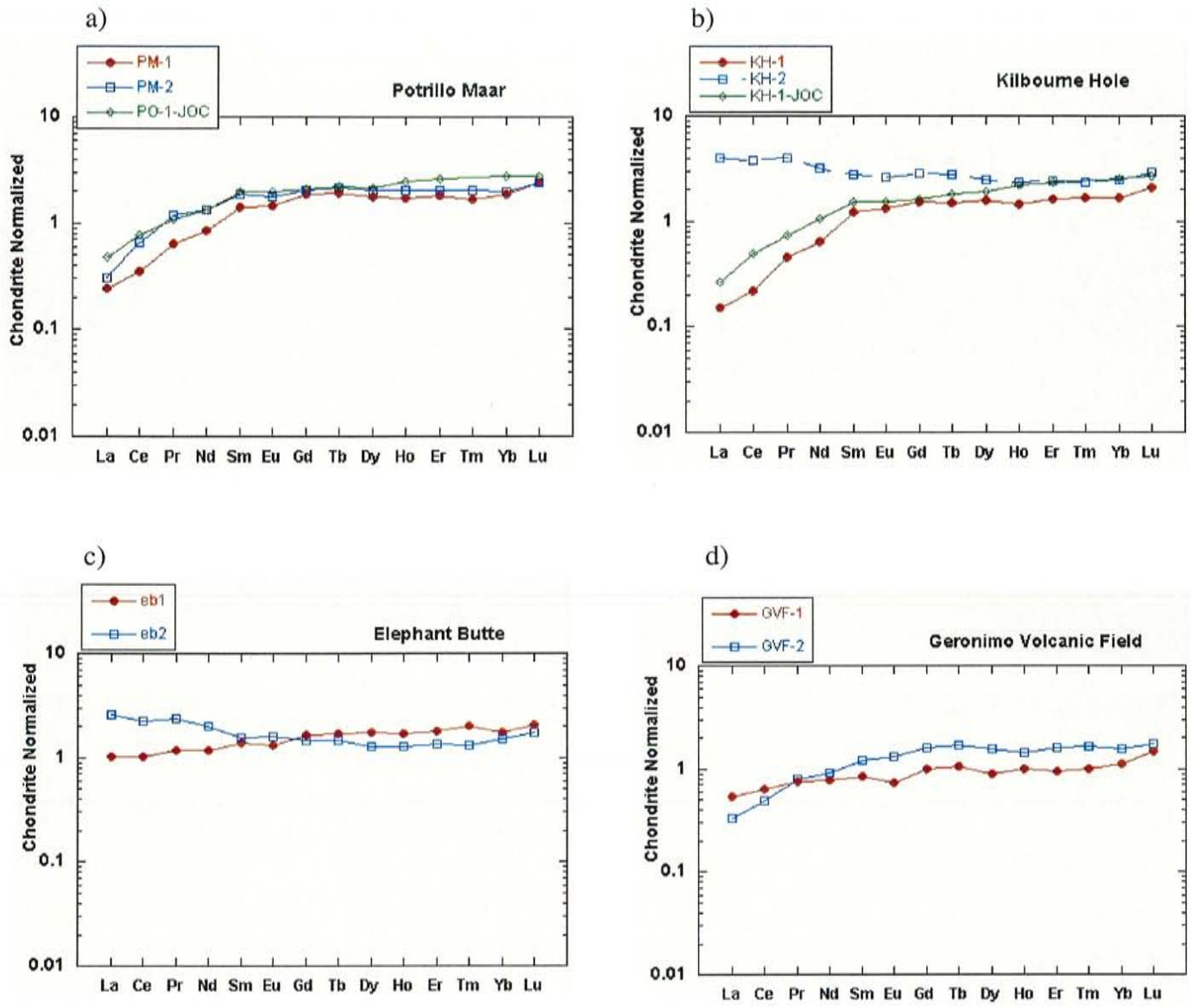

Figure 6 (a - d): Rare earth element distributions. Chondrite normalized with values from Haskin et al. (1968)

Southern Basin and Range

PM = Potrillo Maar, PO-1-JOC = Potrillo Maar Jochum et al. (1989) sample

KH = Kilbourne Hole, KH-1-JOC = Kilbourne Hole Jochum et al. (1989) sample

EB = Elephant Butte

GVF = Geronimo Volcanic Field

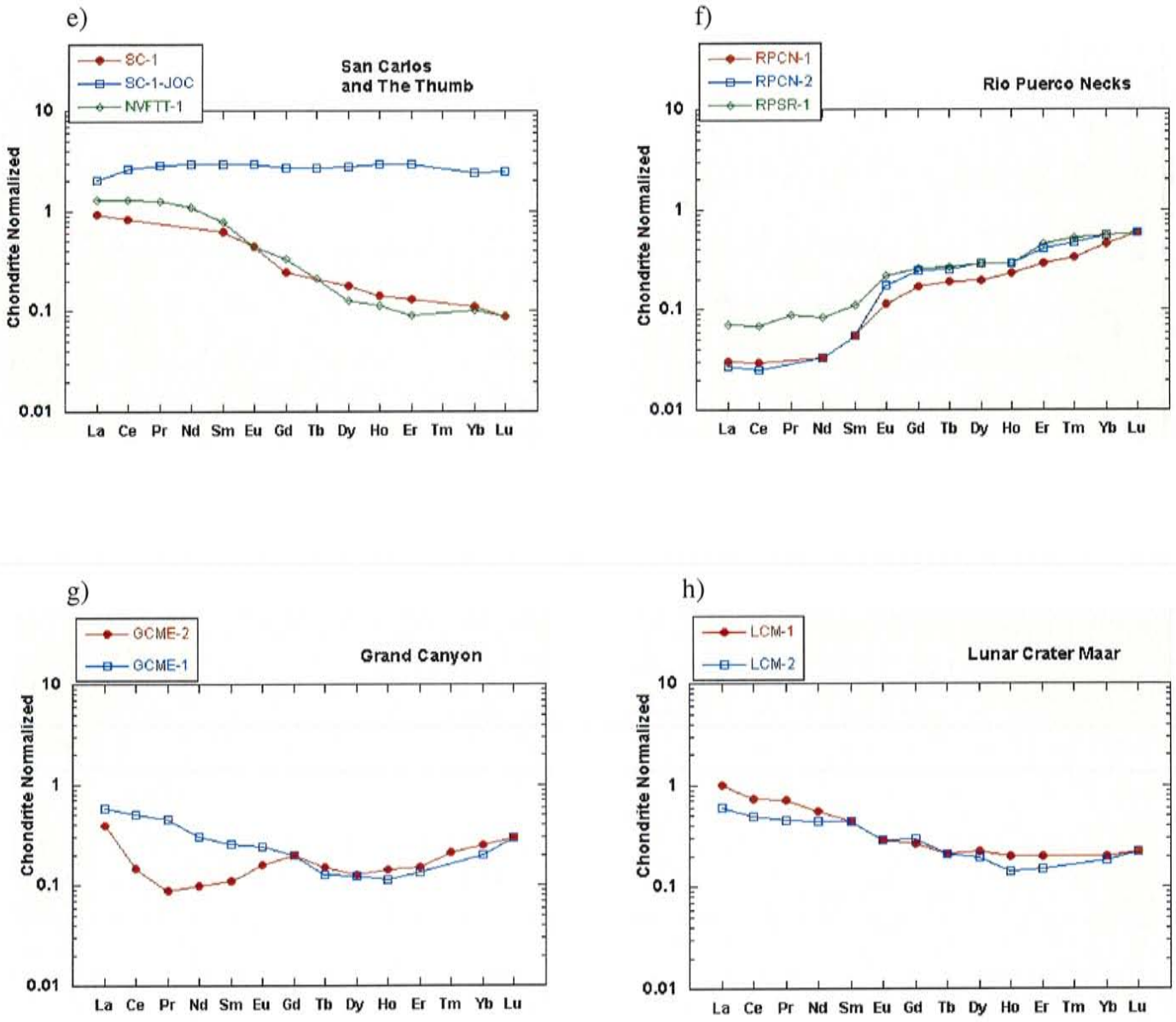

Figure 6 (e - h): Rare earth element distributions. Chondrite normalized with values from Haskin et al. (1968)
Colorado Plateau and adjacent Transition Zone
SC= San Carlos, SC-1-JOC= San Carlos Jochum et al. (1989) sample
NVFTT = Navajo volcanic field: the Thumb
RPCN = Rio Puerco Cerro Negro, RPSR = Rio Puerco Santa Rosa
GCME = Grand Canyon Mount Emma
LCM = Lunar Crater Maar

The REE distributions (Fig. 6b) for Kilbourne Hole have two trends that are distinct from each other. Sample KH-1 and the Jochum et al. (1989) sample are strongly depleted in the LREE. Sample KH-2 has a trend that is slightly enriched in LREE. All samples show a slight enrichment in Lu and slight negative Ho anomalies.

Elephant Butte

The xenoliths from Elephant Butte have different incompatible element distributions (Fig. 5c). EB-2 shows depletion in the most incompatible elements and a negative Ti anomaly. EB-1 also shows variation in the most incompatible elements having positive anomalies for Ba and K, and a slightly positive anomaly for Sr. Although the trends vary in respect to the most incompatible elements, the rest of the distributions are very close to each other.

The REE distributions (Fig. 6c) for Elephant Butte are also distinct from each other. Xenolith EB-1 shows a trend that is depleted in LREE. EB-1 also has a negative Yb anomaly and a slightly positive Sm anomaly. Sample EB-2 is enriched in LREE and it has a slight negative Ce anomaly.

Geronimo Volcanic Field

The two xenoliths from the Geronimo volcanic field have very similar incompatible element distributions (Fig. 5d). The both show a general depletion in the most incompatible elements. They both have positive K anomalies that may not be real since the values for K are low and near the detectability levels (Table 3). They also have slightly negative Zr anomalies.

These xenoliths appear to be samples of the same mantle sources beneath the Geronimo volcanic field.

The xenoliths from the Geronimo volcanic field also have similar REE distributions (Fig. 6d). They are both generally depleted in LREE. Xenolith GVF-2 shows greater depletion in LREE and is relatively more enriched in the HREE. GVF-2 also has slight negative Ho and Yb anomalies. Sample GVF-1 has negative Eu and Dy anomalies.

The Navajo Volcanic Field: The Thumb

The sample from the Thumb has an almost linear distribution with enrichment increasing with incompatibility (Fig. 5e). Therefore, the trend shows depletion in the least incompatible elements and enrichment in the most incompatible elements. There are no anomalies that are well developed.

The REE distribution (Fig. 6e) for the Thumb is enriched in LREE. The trend curves down from La to Gd and then up to Lu.

San Carlos

Our sample from San Carlos has an erratic incompatible element distribution (Fig. 5e). The general positive trend of the distribution is almost linear increasing as incompatibility increases. Therefore, the trend shows depletion in the least incompatible elements and relative enrichment in the most incompatible elements. The San Carlos xenolith has negative Ba, Nb, Sr, and Ti anomalies. The Jochum et al. (1989) xenolith from San Carlos also shows some erratic

nature in the most incompatible elements. Otherwise, the distribution is quite different from our sample. The xenolith of Jochum et al. has a nearly horizontal element distribution, similar to primitive mantle.

The REE distribution (Fig. 6e) of the San Carlos xenolith shows enrichment in LREE. The trend shows enrichment from La to Gd and depletion to Lu. The sample of Jochum et al. (1989) has a REE distribution nearly horizontal with a slight depletion in the LREE.

Rio Puerco Necks

The three xenoliths from the Rio Puerco volcanic necks all have very similar incompatible element distributions (Fig. 5f). The trends are generally depleted in respect to the most incompatible elements and form an upward curve. They all show positive K, Sr, Y, and Ti (slight) anomalies. The K anomalies may not be real since values are low and close to the detectability level (Table 3) and are therefore unreliable. Two out of three samples show a positive Rb anomaly. All the samples from the Rio Puerco volcanic necks seem to have come from the same upper mantle source material.

The three xenoliths from the Rio Puerco volcanic necks show very similar REE distributions (Fig. 6f). They are all rather strongly depleted in LREE, showing a stepwise depletion trend. The first depletion is from Lu to Er, then from Er to Sm, and lastly from Sm to La. RPSR-1 is the least depleted in LREE. The elemental distribution in RPCN-1 is more linear then the others and is less step-like.

Grand Canyon: Mount Emma

The overall incompatible element distribution trends (Fig. 5g) for the two xenoliths from the Grand Canyon's Mount Emma are similar. Generally, they show depletion among the most incompatible elements. Both samples have a positive K anomaly, that may not be real due to the values for K being low and close to the detectability level (Table 3). Sample GCME-2 has positive K, Sr, and Ti anomalies. GCME-1 may show slight positive anomalies for Sr and Hf. The Grand Canyon xenoliths show the most complex distributions among the total population of xenoliths studied, a feature that may be the result of metasomatic activity.

The REE distributions (Fig. 6g) for the Grand Canyon xenoliths are different from each other. Xenolith GCME-2 has a very distinct trend a positive Gd anomaly and enrichment in LREE compared to the HREE. Sample GCME-1 is enriched in LREE and decreases rather linearly to Gd then the trend curves up to Lu.

Lunar Crater Maar: Marcath Flow

The two xenoliths from Lunar Crater Maar have very similar incompatible element distributions (Fig. 5h). Both show enrichment in LREE but show a lack of enrichment in the most incompatible elements. They both have positive Ti anomalies. The xenoliths from Lunar crater Maar are most likely samples from the same upper mantle source material.

The xenoliths from Lunar Crater Maar have similar REE distributions (Fig. 6h). They show relative enrichment in LREE or a relative depletion in HREE. Xenolith LCM-1 shows enrichment from La to Tb then flattens out to Lu. Sample LCM-2 shows enrichment from La to Sm then shows depletion to Lu.

Between- Sites Comparisons

Incompatible Element Distributions

For the incompatible element distributions (Fig. 7) of the SW xenoliths there are four major trends. The trends are divided as follows: Group I – relatively strong depletion in the most incompatible elements, Group II – progressive depletion as incompatibility increases, Group III – horizontal trend similar to primitive mantle, and Group IV – relative enrichment in the most incompatible elements.

Group I (Fig. 7a) shows relatively strong depletion in the most incompatible elements compared to the least incompatible elements. There are anomalies present in Rb, Ba and K that are mostly positive but are in some cases negative. The ppm values for these elements are generally low and near their detection levels (Table 3), so that the values are not reliable. Rb, Ba and K are also the most mobile elements in aqueous solutions, therefore it is possible that metasomatic processes have affected these elements. This group consists mainly of southern Basin and Range xenoliths.

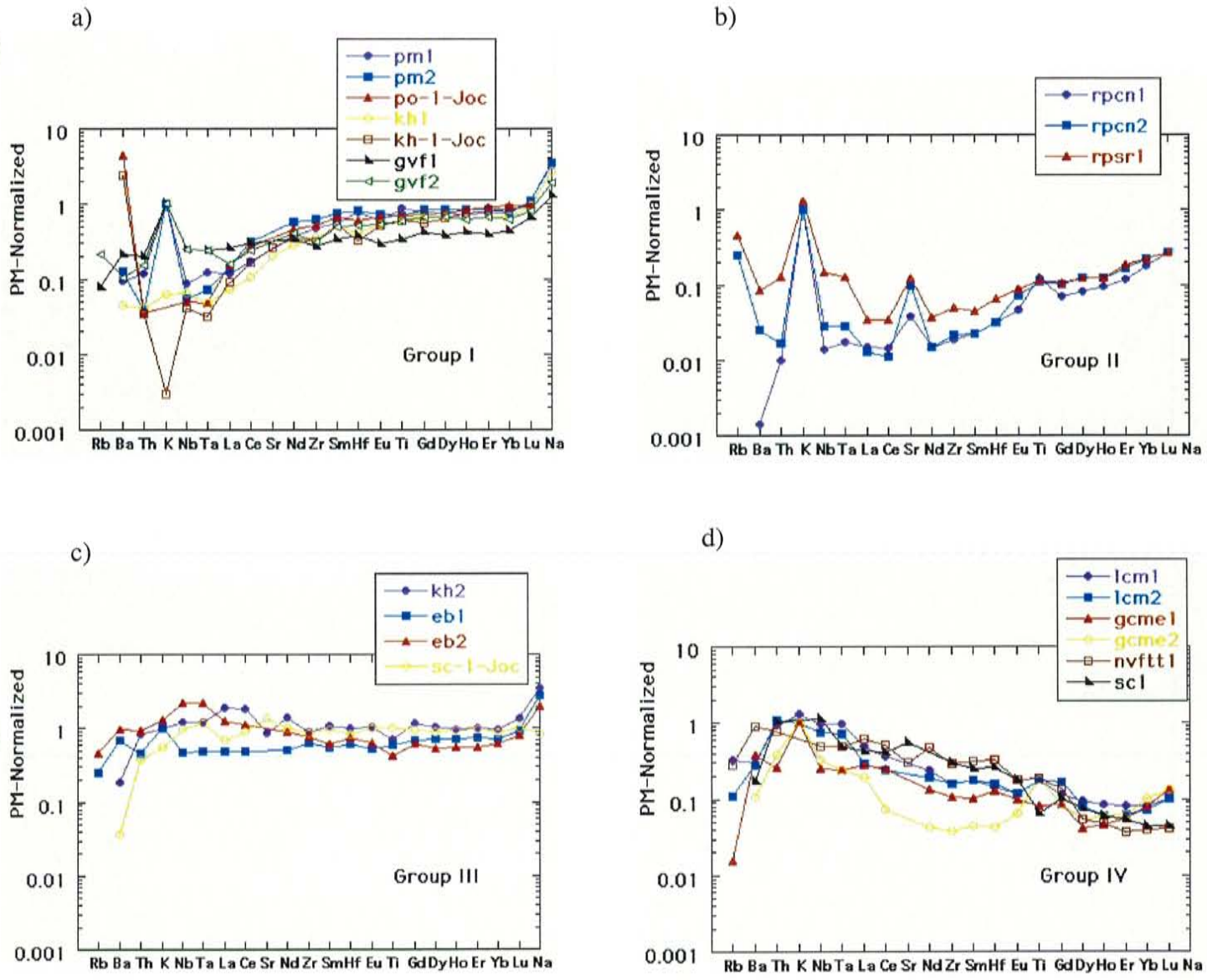

Figure 7 (a - d): Comparisons between sites of incompatible element distributions. Sample abbreviations are the same as in previous figures.

a) Group I: Relative strong depletion in the most incompatible elements

b) Group II: Regular depletion as incompatibility increases

c) Group III: Horizontal trend similar to that which would be expected from primitive mantle

d) Group IV: Relative enrichment in the most incompatible elements

Group II (Fig. 7b) shows progressive depletion as incompatibility increases. Comparatively, the values for all the elements in Group II are lower then those in Group I. There are some positive anomalies prevalent in the trend: K, Sr and Ti; one sample also has a low Ba value. The xenoliths in this group are all from the Rio Puerco Necks in the Mt. Taylor volcanic field, which lies in the Transition Zone between the Colorado Plateau and the Rio Grande Rift.

Group III (Fig. 7c) xenoliths exhibit primitive mantle-like element distributions. Some of the samples show negative Ti anomalies and there is some variation in values for the most incompatible elements. The xenoliths in this group are mostly from the southern Transition Zone between the Colorado Plateau and the Basin and Range Provinces.

Group IV (Fig. 7d) shows relative enrichment in the most incompatible elements compared to the least incompatible elements. This group shows greater variation in that individual trends show different anomalies. The xenoliths all show a relative depletion in Rb and Ba (two very mobile elements in aqueous solutions). Xenolith GCME-2 that is included in this group, exhibits a very different type of trend from the other xenoliths. It does, however, show an overall relative enrichment in the most incompatible elements and for that reason it is placed in Group IV. These samples are generally from the Colorado Plateau and Great Basin Provinces.

It is important to note that these groupings are not exclusive to each locality. For instance, Kilbourne hole and San Carlos xenoliths are divided amongst different groups.

Rare Earth Element Distributions

For the REE distributions (Fig. 8) the xenoliths seem to fall into the same four groupings. Group I (Fig. 8a) shows a strong relative depletion in the lightest of the REE. Group II (Fig. 8b) shows a trend of progressive depletion as the REE decrease in atomic number. Group III (Fig. 8c) shows a horizontal trend similar to primitive mantle (slightly elevated from what would be expected for average chondrite). Group IV (Fig. 8d) has a relative enrichment in the lightest REE.

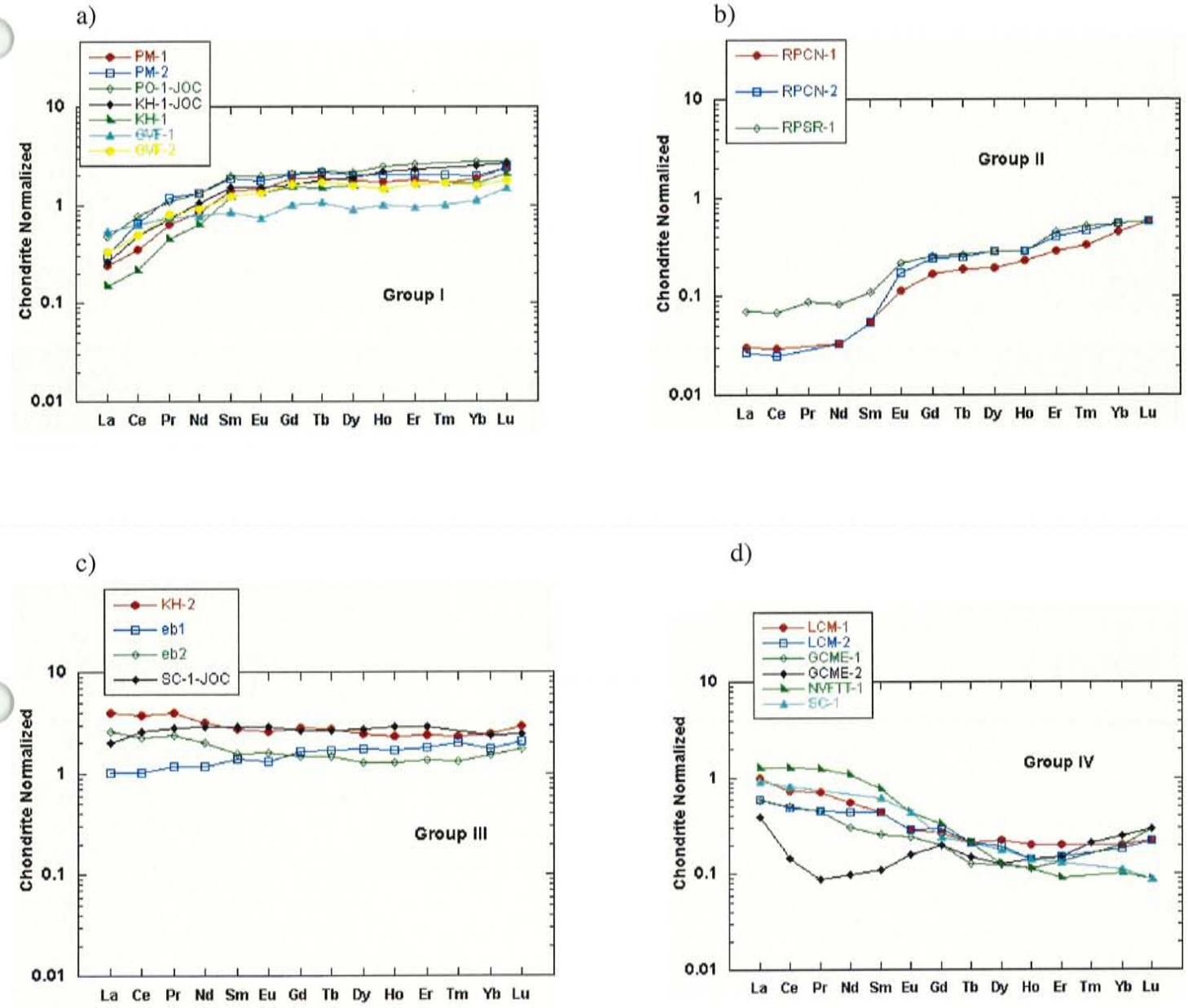

Figure 8 (a - d): Comparisons amongst rare earth distributions. Sample abbreviations are the same as in previous figures.

a) Group I : Relative strong depletion in the lightest REE
b) Group II : Progressive depletion as atomic number and mass decreases
c) Group III : Horizontal trend trend similar to that which would be expected from primitive mantle
d) Group IV : Relative enrichment in the lightest REE

V: Discussion

Introduction

The upper mantle is heterogenous with respect to trace element and isotopic composition (e.g. Roden & Shimizu, 1993; O'Reilly & Griffin, 1988; Roden et al., 1984; Frey & Prinz, 1978; Frey & Green, 1974). Several groups are currently studying processes that produce these heterogeneities. The topics that will be addressed in this section are the depth and the degree of melting, metasomatic processes that may have played a role in xenolith geochemistry, and possible tectonic settings. The discussion will be based on observations and results from this study and other studies.

Degree and Depth of Melting

Petrography

One indication of the degree of melting is the accessory minerals found in the lherzolites. Lack of spinel and garnet implies that a xenolith is more restitic and therefore has undergone a higher degree of melting. Samples from this study exhibit extremely low or no modal spinel are NVFTT-1, LCM-1, LCM-2, and EB-2. These samples may represent sources that have experienced a higher degree of melt extraction. Sample PM-1 contains both spinel and garnet, and the presence of garnet within this xenolith may indicate a less restitic source. The source for PM-1 may have undergone a lesser degree of melting than the other xenoliths in this study. The occurrence of garnet can also be an indicator for the depth of melting and possibly the depth of melt extraction. Within the lherzolite rock group, garnet lherzolite is most dense due to the high density of garnet. Spinel lherzolite (Fig. 9) is less dense than garnet lherzolite and is not stable to depths that garnet lherzolite is stable (Condie, 1997). Lherzolites without either garnet or spinel are the least dense and are stable at still shallower depths (Condie, 1997). Therefore, garnet lherzolites reside deepest in the upper mantle and lherzolites without garnet or spinel are

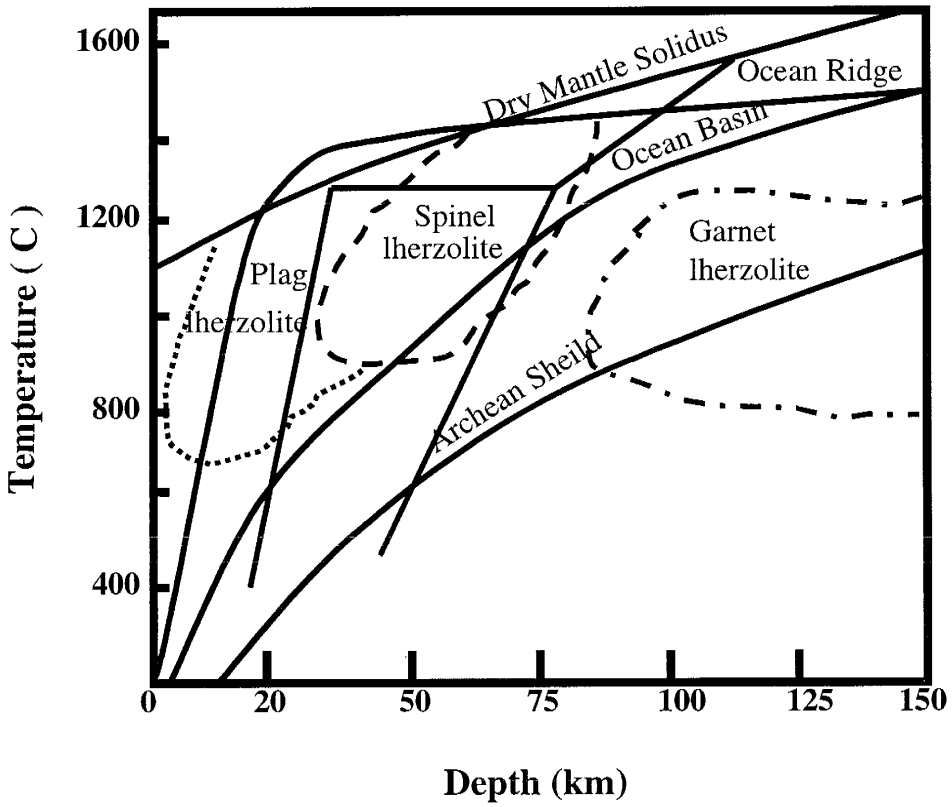

Figure 9: Temperature- Depth stability fields for lherzolites.
Also included for reference are some lithospheric geotherms and the dry mantle solidus. Garnet lherzolite zone is representative of kimberlite type xenoliths, spinel lherzolite zone of alkali basalt type, and plagioclase lherzolite of ophiolite type. From Condie, 1997

derived from the shallowest portions of the upper mantle, while spinel lherzolites are derived from an intermediate depth (Fig. 9). These relationships suggest that the source of PM-1 must have been the deepest of xenoliths included in this study. Samples with low or no modal spinel must have been derived from a source depth where spinel entered the melt, likely at a shallow depth.

Magnesium Number

The magnesium number (Mg #) is commonly utilized in degree of melting studies. The distribution of Mg #'s among the samples (Fig. 3) shows that the samples all plot above the convecting mantle (Mg # of 88) and are centered near the accepted value for primitive mantle (Mg # of 91). This indicates that the samples have sources that are from within the lithosphere.

The Mg # versus Al_2O_3 graph (Fig. 4a) shows the expected linear trend with a few outliers. Low Al_2O_3 values indicate that the sample source has experienced higher degrees of melt extraction because the aluminum is housed chiefly in garnet and clinopyroxene that enter the melt first. The xenoliths that are deficient in modal spinel (NVFTT-1, LCM-1, LCM-2 & EB-2) are the samples plotting lowest in Al_2O_3, while PM-1 (the sample with garnet) plots at a considerably higher Al_2O_3 value than the rest of the samples. These results are consistent with the previous observation that samples NVFTT-1, LCM-1, LCM-2 and EB-2 are derived from sources that are more restitic than a majority of the xenoliths and sample PM-1 is from a less restitic source.

Melting Curves and Oxide Variation Diagrams

The melting curves represent geochemical signatures of source restite after a melt removes a percentage of material from a system that has the composition of either N-MORB (Fig. 10 a-c, f) or island arc basalt (IAB, Fig. 10 d&e). The melting curves are REE distributions generated using partial melt equations. The primary equations used to determine the amount of each element at a given percentage of melt are as follows: $C_S / C_O = [1 / F] \exp [1 / D_O - 1]$ and $C_L / C_O = 1 / D_O [1 / F] \exp [1 / D_O - 1]$. C_O is the initial composition of an element in the solid with C_S being the final concentration of an element in the residual solid after melt has been extracted. C_L is the instantaneous concentration of the element in the liquid. F is the fraction of which partial melting has progressed (or how far one wants to model it) determined as the mass of melt divided by the mass of source. D_O is the bulk distribution coefficient and is related to the concentration of an element in the residual solid after a percentage of melt has been removed divided by the instantaneous concentration of an element in the liquid after a portion of melt has been removed.

The REE distribution melting curves based on work similar to McColluch and Gramble (1991) (Fig. 10) produce N -MORB based melts that show progressive depletion in the most incompatible elements with a negative La-Ce anomaly. While IAB based melts show depletion of the incompatible elements and a negative Nb-Ta anomaly. By comparing these produced distributions to the distributions from the Southwest xenoliths, it is possible to estimate that at least some of the xenoliths at Potrillo Maar and Kilbourne Hole underwent about 10% melting of a depleted mantle source (Fig. 10f). Other Group I xenoliths show the same degree of depletion and melt removal.

a)

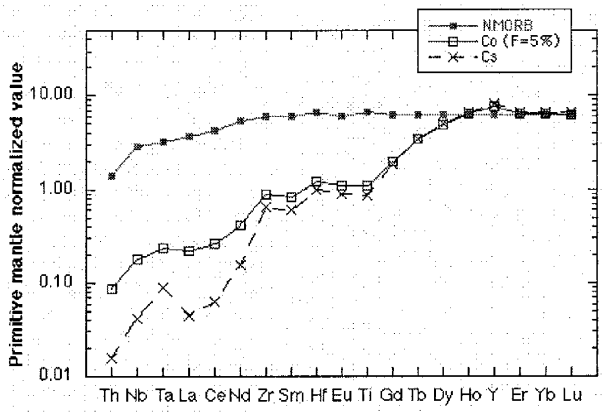

b)

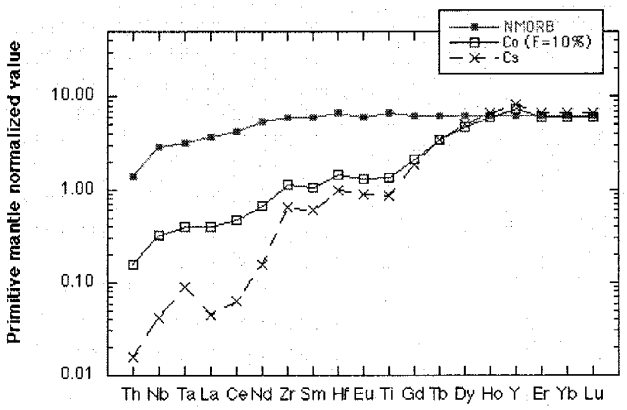

c)

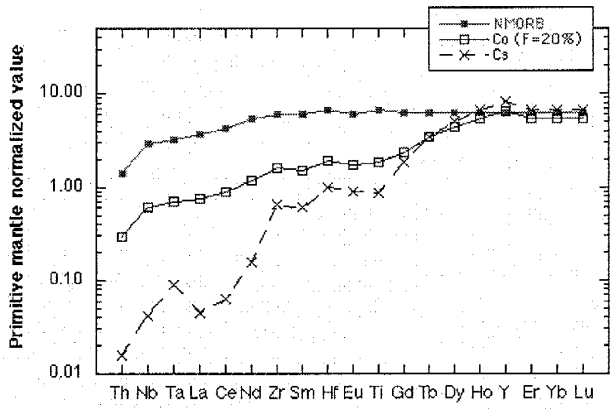

Figure 10 (a - c): Incompatible element distributions in restite (Cs), source (Co) and liquid (assume N-MORB) for varying degrees of batch melting. Restite is composed of cpx, opx, and olivine. Graph provided by K. Condie.

a) 5% melt

b) 10% melt

c) 20% melt

d)

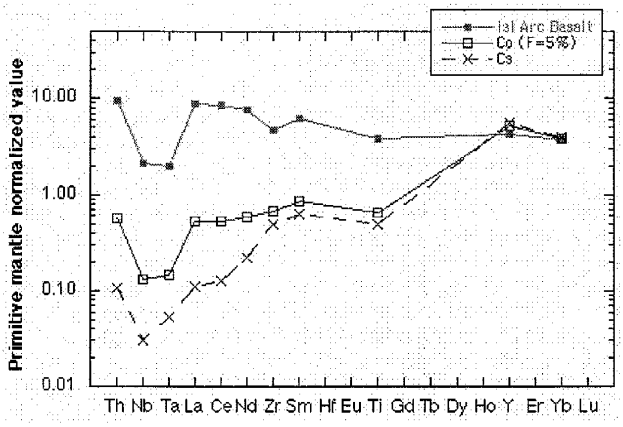

e)

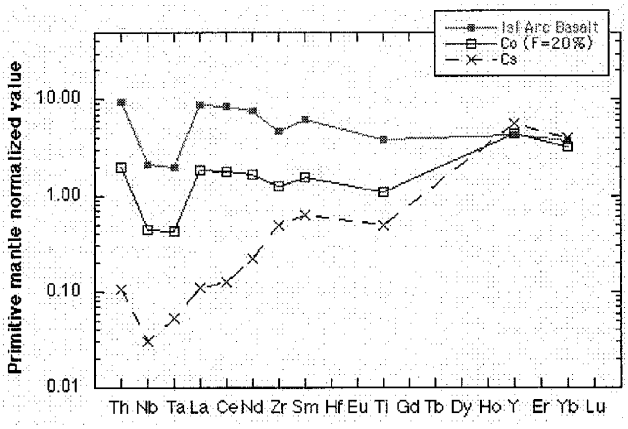

f)

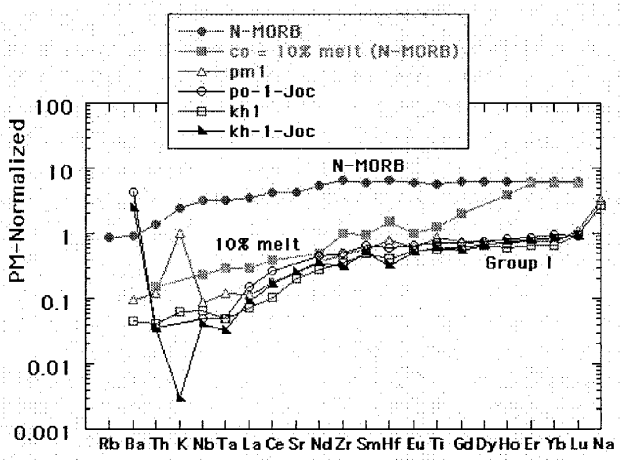

Figure 10 (con.): Incompatible element distributions in restite (Cs), Source (Co) and liquid (assume Arc Basalt) for varying degrees of Batch melting. Restite is composed of cpx, opx, and olivine. Graphs provided by K. Condie, 2002.

d) 5% melt

e) 20% melt

f) Group I xenoliths compared to 10% N-MORB melt

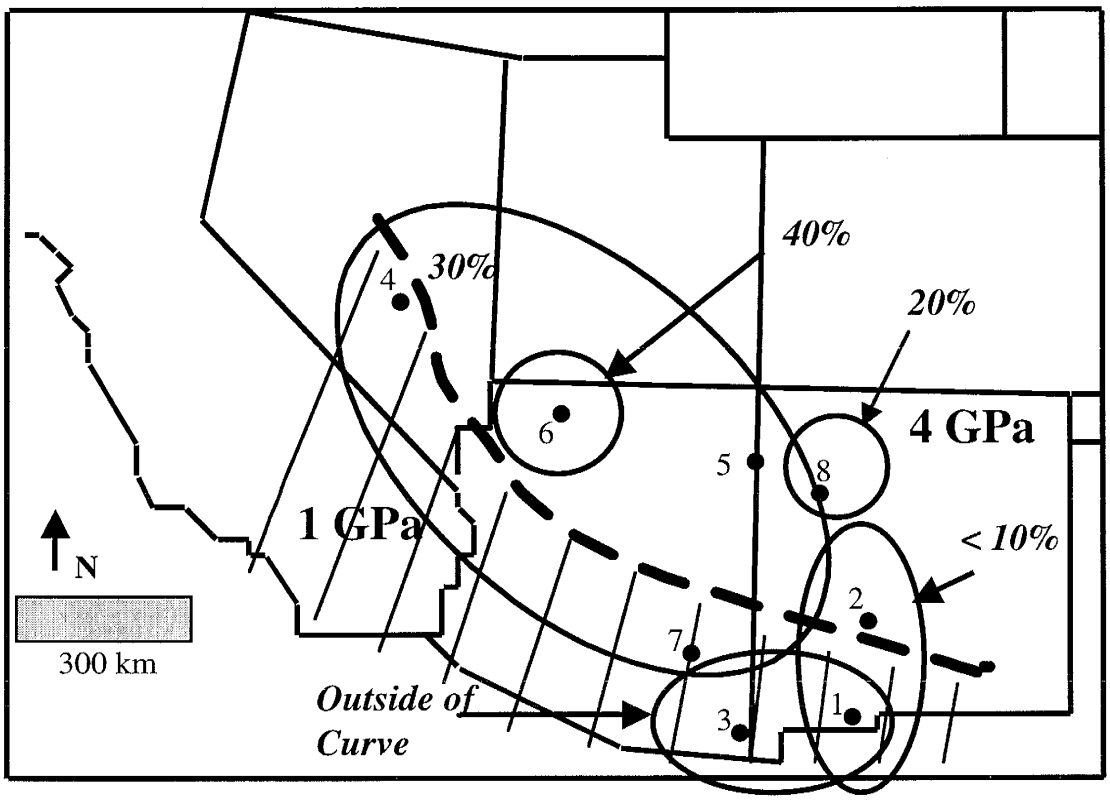

Figure 12: Map of xenolith sites in Southwest United States with percentages of Batch melt extraction and pressure regime as suggested by Walter's (1999) oxide variance diagrams. Dashed line seperates the 1 GPa and 4 GPa pressure regimes. Based on data from figure 11b.

1 Potrillo Maar & Kilbourne Hole, Potrillo volcanic field
2 Elephant Butte
3 Geronimo volcanic field
4 Marcath Flow, Lunar Crater Maar
5 The Thumb, Navajo volcanic field
6 Mount Emma, Grand Canyon
7 San Carlos
8 Rio Puerco Necks, Mount Taylor volcanic field

Oxide variation diagrams (Fig. 11) like those from Walter (1999) use weight percent values of oxides to plot restites and determine the degree of melt extraction and the pressures at which the melt was extracted. Heavy lines on the graph represent the unmelted residues of polybaric near-fractional extraction with pressures denoted along the line. Fractional extraction refers to immeasurable small percentages of melt that are extracted instantaneous without being allowed to interact with the remainder of the system. Thinner lines represent the isobaric batch melt extraction at given pressures and dashed lines represent the percentage of batch melt extraction. Batch melting refers to the process of extraction of melt that allows for measurable amounts (called batches) of melt to form before being removed from the system.

The Al_2O_3 versus FeO variation diagram (Fig. 11a) shows some differentiation among the SW xenoliths. Southern Basin and Range samples have batch melt extraction percentages less then 20% and pressures of about 1 GPa. Xenoliths from the Colorado Plateau and related Basin and Range sites record 20 to 40% batch melting and pressure upwards to 4 GPa. The Lunar Crater Maar and San Carlos samples show batch melt percentages of about 30% and both lie along the 1 GPa isobaric extraction line.

The MgO versus FeO variation diagram (Fig. 11b) shows similar differentiation among the SW xenoliths. Generally, the southern Basin and Range xenoliths show a lower percentage of batch melt extraction (< 20%), and lower average pressures, probably between 1 and 2 GPa. The Colorado Plateau xenoliths show a higher percentage of batch melt extraction from 20 to 40% and upwards to 3 or 4 GPa pressures. The Lunar Crater Maar and San Carlos samples fall at about 30% batch melt extraction and along the 1 GPa isobaric batch melt extraction line. Figure 12 is a map-view of the two basic pressure regimes 1 GPa and 4 GPa along with zones of batch melt percentages as related to xenolith localities.

a)

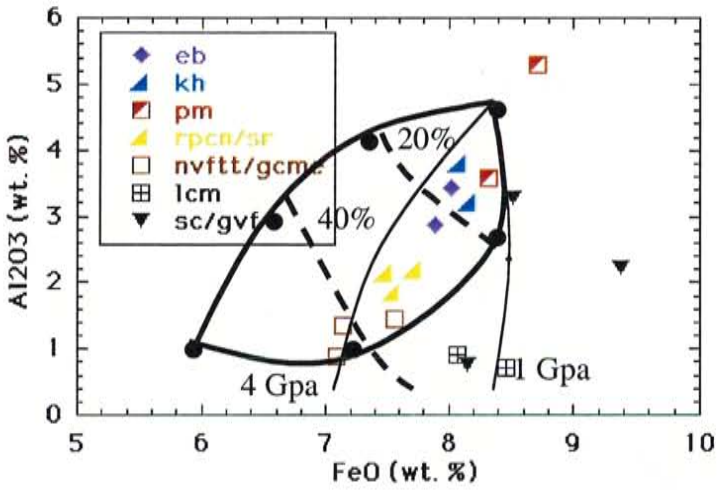

b)

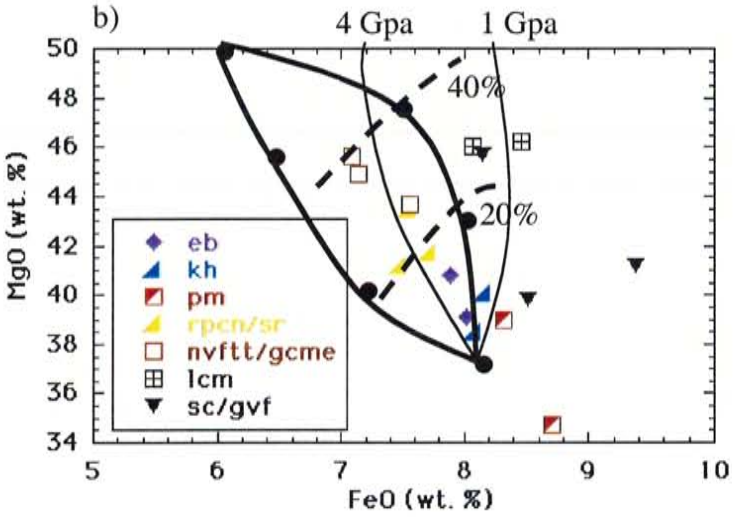

Figure 11 (a & b): Oxide variance diagrams. Thick lines represent residues of polybaric near-fractional extraction, thin lines represent residues of isobaric batch melt Extraction, an d dashed lines represent the percent of batch melt extraction. Based on Walter, 1999.
Abbreviations:
eb = Elephant Butte, kh = Kilbourne Hole, pm = Potrillo Maar
rpcn/sr = Rio Puerco Necks, nvftt = The Thumb, gcme = Grand Canyon
lcm = Lunar Crater Maar, sc = San Carlos
gvf = Geronimo volcanic field

Metasomatism

Introduction

A common means of introducing secondary minerals into mantle xenoliths is metasomatism resulting from fluid-rock interaction at elevated temperature and pressure. Metasomatism may involve either channelized or pervasive fluid flow. Channelized flow frequently uses fractures as conduits and these can become filled with secondary minerals such as carbonate, oxides, or silicate phases. During pervasive flow, fluids travel through broad regions along micro-cracks, grain boundaries, or crystal planes resulting in secondary minerals such as carbonate, oxide, and silicate phases which occur as secondary fluid inclusions or as micro-crystals. In extreme cases, entire minerals can be replaced forming psuedomorphs. There are several recognized types of metasomatism associated with xenoliths: carbonatite, potassium, iron – titanium, and sodium metasomatism (Kepezhinskas et al., 1993). Each of these types will be discussed below.

Loss on Ignition

A series of loss on ignition graphs (Fig. 13) are included to evaluate possible metasomatism in the xenoliths. Loss on ignition (LOI) is the mass difference after the heating (to 800°C) of the powdered samples. The mass difference is caused by a loss of structural volatiles such as H_2O, CO_2, and S (Winter, 2001). Metasomatism can cause increased LOI values by the addition of mineral phases such as carbonate, clay, or zeolites that bear water that is subsequently lost during heating. The four major element (in oxide form) versus LOI graphs that are presented here include SiO_2, MgO, Fe_2O_3, and CaO. The four trace element versus LOI graph include La/Yb, Zr/Y, Nb/Zr, and Nb/Y.

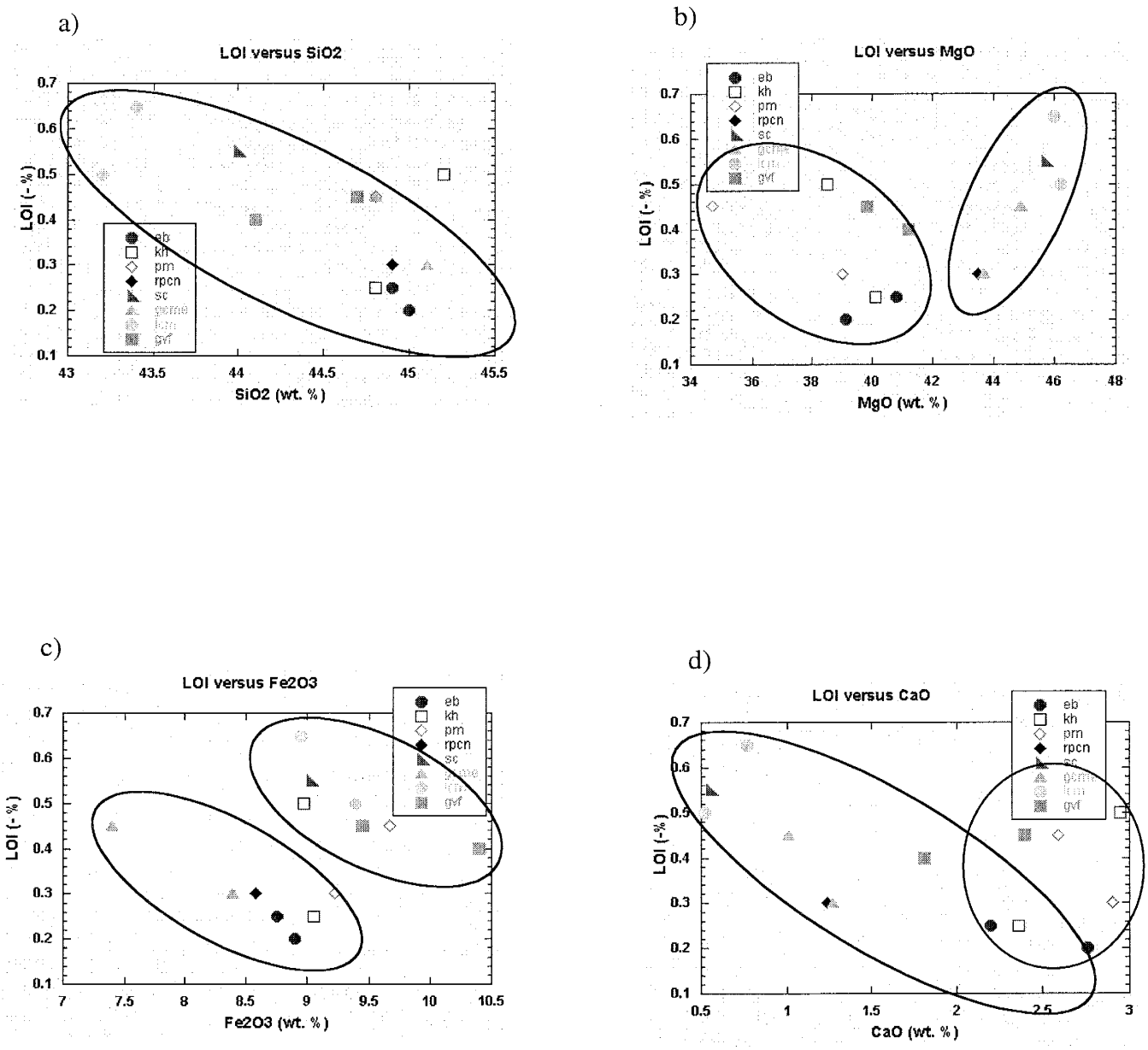

Figure 13 (a - d): Loss On Ignition (LOI) versus major element graphs. Major elements in the form of oxides. Trends discussed in text are circled for clarity.

eb = Elephant Butte, pm = Potrillo Maar, kh = Kilbourne Hole,
rpcn = Rio Puerco Necks, sc = San Carlos,
gcme = Grand Canyon, lcm = Lunar Crater Maar,
gvf = Geronimo volcanic field

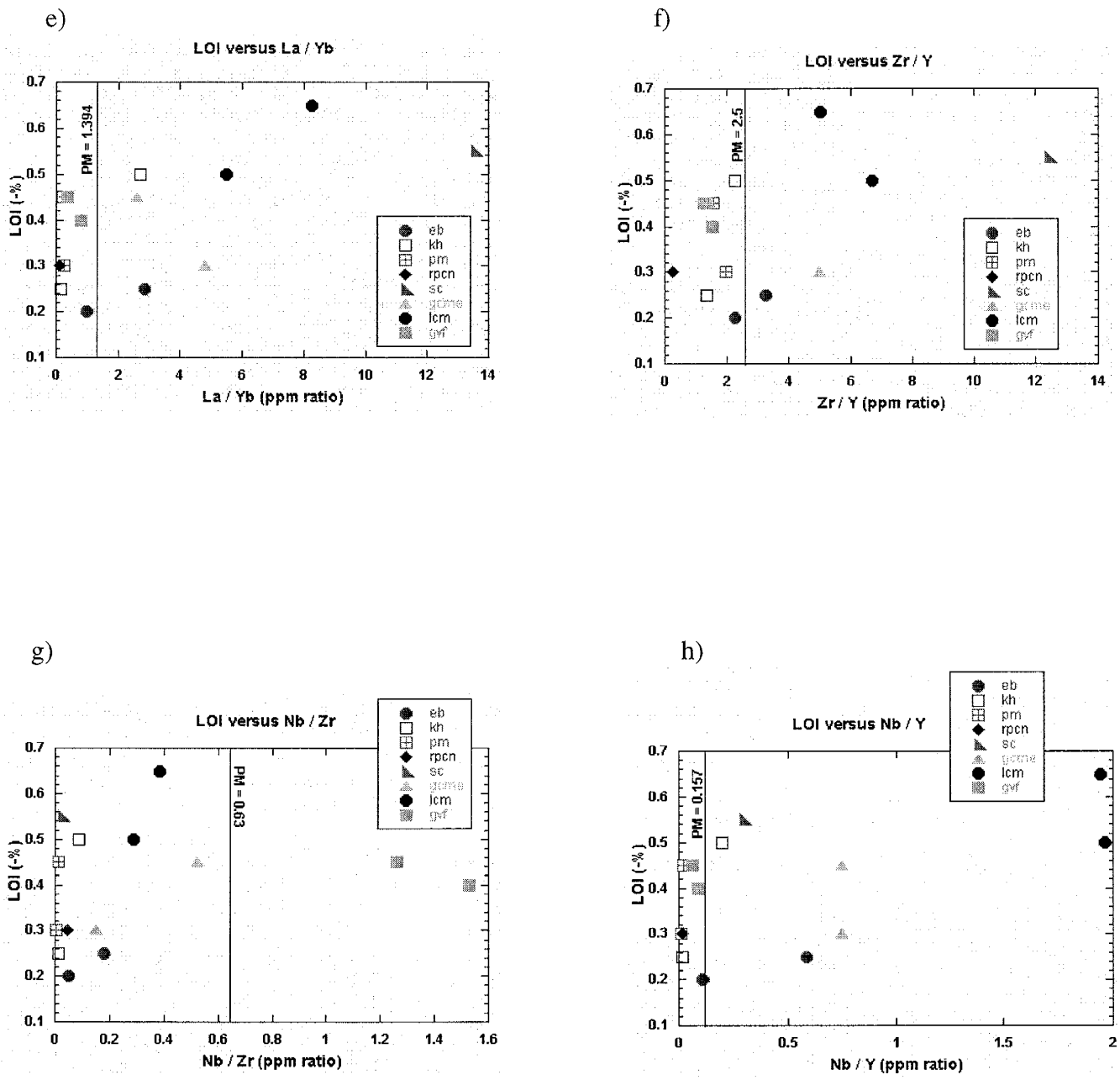

Figure 13 (e - h): Loss On Ignition (LOI) versus trace element graphs.

eb = Elephant Butte, pm = Potrillo Maar, kh = Kilbourne Hole,
rpcn = Rio Puerco Necks, sc = San Carlos,
gcme = Grand Canyon, lcm = Lunar Crater Maar,
gvf = Geronimo volcanic field

SiO_2 versus LOI (Fig. 13a) shows a general trend of increasing SiO_2 as LOI decreases. There seems to be a tighter grouping of the xenoliths with higher silica and lower LOI. This is indicative of LOI volatiles not being housed in the silicate minerals.

MgO versus LOI (Fig. 13b) shows two groupings. One trend showing an overall increase in LOI as MgO increases. These xenoliths are generally from the southern Basin and Range province. The other trend shows a general increase in LOI as MgO increases. The xenoliths in this trend are mostly from the Great Basin or Colorado Plateau.

Fe_2O_3 versus LOI (Fig. 13c) shows two general trends of increasing LOI as Fe_2O_3 decreases. One trend has overall higher iron oxide and LOI values.

CaO versus LOI (Fig. 13d) also shows two general groupings. One group has increasing LOI values as CaO values decrease consisting of xenoliths from the Great Basin or Colorado Plateau. The other group exhibits less variation in LOI as CaO changes and is generally defined by samples from the southern Basin and Range.

In the La/Yb versus LOI plot (Fig. 13e), most samples fall above the value for primitive mantle. This is due chiefly to for elevated La values in the xenoliths and therefore enrichment of LREE. The samples that plot in this region include those from the Transition Zone and the Great Basin.

In the Zr/Y versus LOI plot (Fig. 13f), most samples plot near or below the accepted value for primitive mantle. These are generally the Rio Grande Rift and Transition Zone (mostly New Mexican) xenoliths. In contrast, the Great Basin and Transition Zone (mostly Arizonan and Nevadan) xenoliths plot above or below primitive mantle.

In the Nb/Zr versus LOI plot (Fig. 13g), most samples plot below the accepted value for primitive mantle, except the samples from the Geronimo volcanic field. The Geronimo xenoliths plot above primitive mantle due to Zr depletion present in both samples.

In the Nb/Y versus LOI plot (Fig. 13h), most samples plot below or near the accepted value for primitive mantle. The exceptions that plot above the primitive mantle value are Grand Canyon, Lunar Crater, and one from Elephant Butte. The elevation is likely due to Nb enrichment. These samples show incompatible element enrichment in their trace element distributions.

Carbonatite Metasomatism

Carbonatite metasomatism occurs when fluid derived from carbonatite magmas in the mantle interacts with the surrounding mantle. Carbonatite magmas characteristically exhibit low viscosity; this may enable them to transport and release incompatible trace elements and other volatiles into the upper mantle (Watson et al., 1990; Green & Wallace, 1988; Baker & Wylie, 1992; Rudnick et al., 1993). Mantle rocks that have interacted with the fluids derived from these magmas may become enriched in trace elements and volatiles.

Rudnick et al. (1993) used several element ratios to graphically demonstrate the effects of carbonatite metasomatism on mantle xenoliths. Both a Ca/Al versus Ti/Eu graph (Fig. 14a) and a (La/Yb)n versus Ti/Eu graph (Fig. 14b) are reproduced with data from this study. In the Ca/Al versus Ti/Eu plot, a curve is included indicating the amount of carbonate interaction that has occurred by plotting two endmembers: average calcium carbonatite and average harzburgite. Most samples plot below 0.2% interaction with an average carbonatite endmember. Samples that plot above 0.5% interaction lie off the mixing curve and do not indicate carbonatite interaction. The (La/Yb)n versus Ti/Eu plot shows the values of the two ratios from the xenoliths along with average calcium carbonatite values and the Ti/Eu ratio line for chondrite for

a)

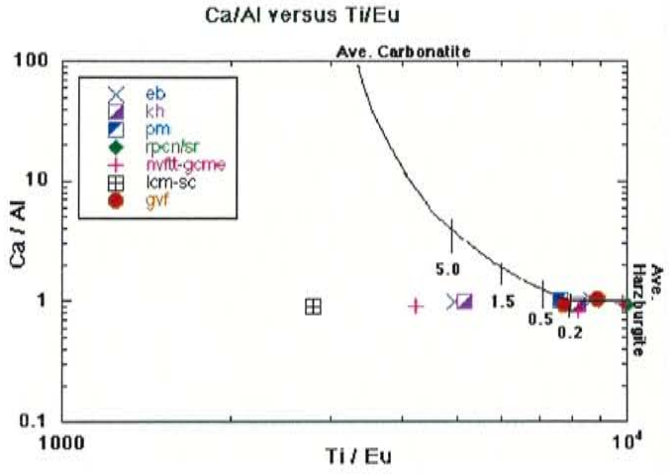

b)

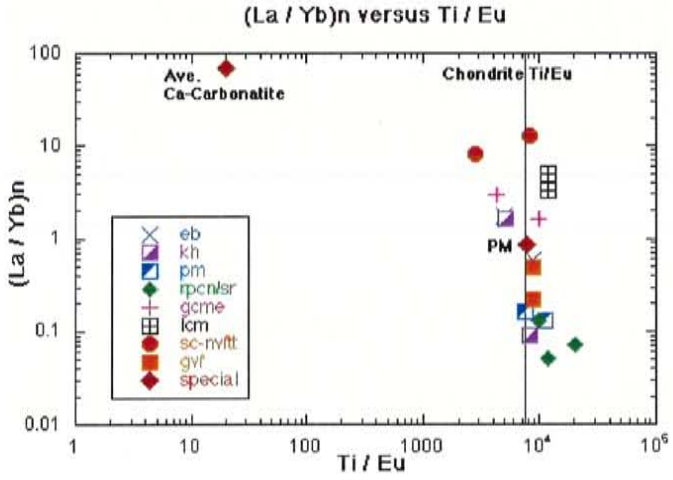

Figure 14 (a & b): Element ratio graphs for evaluation of carbonatite interactions with xenoliths based on Rudnick et al., 1993.

eb = Elephant Butte, kh = Kilbourne Hole, pm = Potrillo Maar
rpcn/sr = Rio Puerco Necks, gcme = Grand Canyon
lcm = Lunar Crater Maar, sc = San Carlos
nvftt = The Thumb, gvf = Geronimo Volcanic Field
PM = Primitive mantle

comparison. Most samples lie near the chondrite Ti/Eu line and below or near the value for primitive mantle. Some samples that plot above primitive mantle seem to show some evidence for carbonatite interaction – these are the same samples that plot off the mixing curve on the Ca/Al versus Ti/Eu graph.

It is also common for xenoliths that have experienced carbonatite metasomatism to have modal apatite due to elevated phosphorus levels. Though some primitive mantle normalized incompatible element distributions exhibit positive phosphorus anomalies, the amounts of P_2O_5 in the SW xenoliths are less than 0.04 weight percent, the value suggested by O'Reilly and Griffin (2000) needed for modal apatite. Modal apatite is not observed in the thin sections of any of the SW xenoliths. This supports the previous observations that provide no evidence for carbonatite metasomatism.

The incompatible element distributions from xenoliths of the Southwest are compared to those of xenoliths that are accepted as having undergone carbonatite metasomatism (Fig. 15a). Incompatible element distributions from xenoliths that experienced carbonatite metasomatism generally show positive Sr and Ce anomalies, as well as, relative enrichment in the most incompatible elements (such as Rb, Ba, Th, and K). Only the samples from the Rio Puerco Necks exhibited positive anomalies such as K, Sr, and Ti; that may indicate carbonatite metasomatism.

Iron - Titanium Metasomatism

Iron – Titanium (Fe-Ti) metasomatism is caused during interaction of CO_2-rich silicate melts with mantle phases (Kepezhinskas et al., 1995). A positive titanium anomaly is present on the PMn distributions of xenoliths accepted to have experienced Fe – Ti metasomatism. The comparison of the known Fe – Ti metasomatized xenoliths to the xenoliths from this study show positive titanium anomalies in xenoliths from Lunar Crater Maar and the Rio Puerco

a)

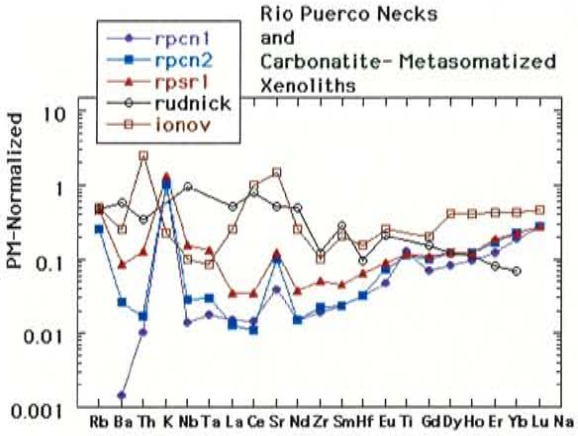

b)

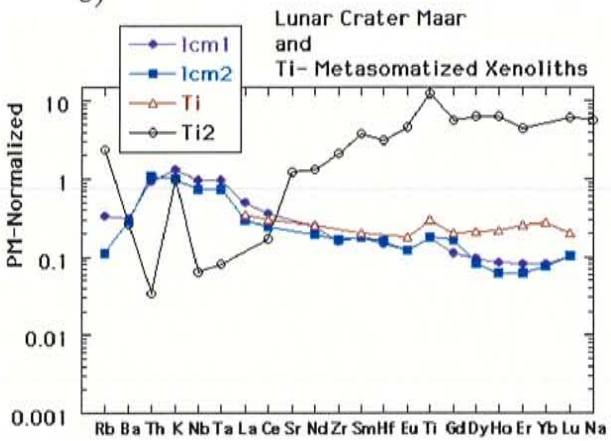

c)

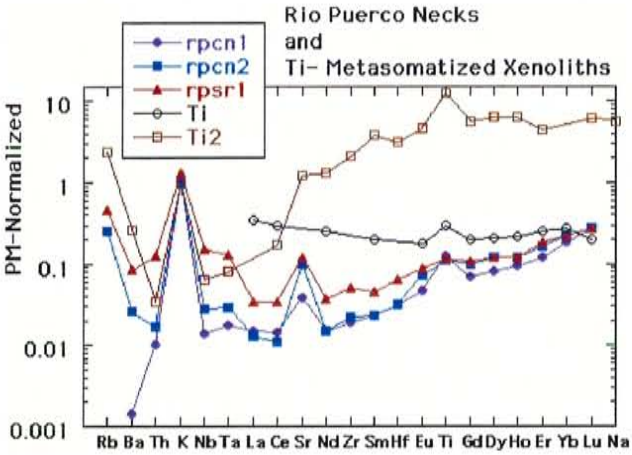

Figure 15 (a - c): Incompatible element distribution comparisons with known metasomatized xenoliths.
Abbreviations include: rpcn & rpsr = Rio Puerco Necks;
lcm = Lunar Crater Maar; rudnick = Rudnick et al., 1993 : carbonatite metasomatized sample; ionov = Ionov et al., 1993: carbonatite metasomatized sample #SB-3 , ti = Ionov et al., 1993: Ti-metasomatized sample; ti2 = McDonough et al., 1989: Ti-metasomatized sample # D-50

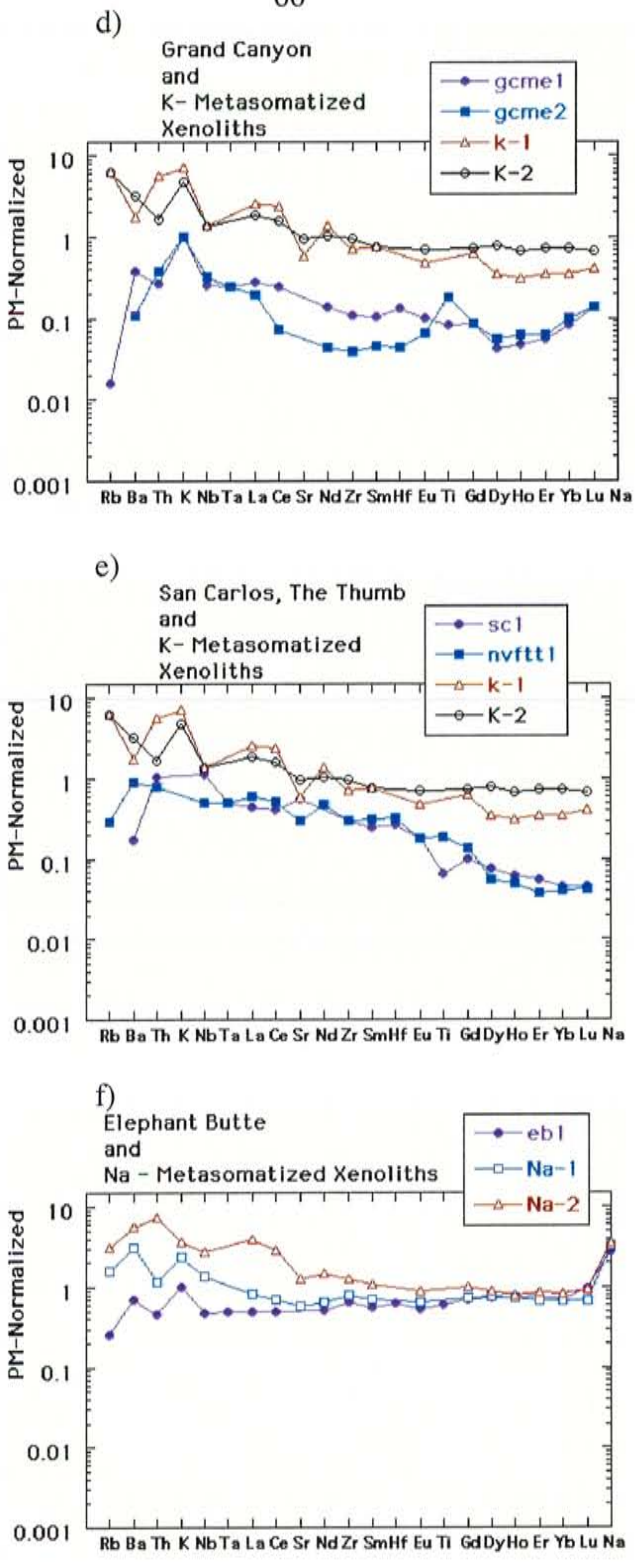

Figure 15 (d - f): Incompatible element distribution comparisons with known metasomatized xenoliths.
Abbreviations include: gcme = Grand Canyon, sc = San Carlos,nvftt = The Thumb, eb = Elephant Butte, k-1 = Beccaluva et al.., 2000:K-metasomatized sample, k-2 = Beccaluva et al., 2000:K-metasomatized sample; Na-1, Beccaluva et al., 2000: Na Metasomatized sample; Na-2, Beccaluva et al., 2000, Na metasomatized sample

Necks (Fig. 15b & c). Both the known metasomatized xenolith and xenoliths from this study share a strong positive K anomaly (though the K value is small and near the dectability limit (Table 3) and therefore suspect).

The Al_2O_3 versus FeO plot (Fig. 4b) and Al_2O_3 versus TiO_2 plot (Fig. 4c) show xenoliths LCM-1 and LCM-2 plotting with elevated values of iron and titanium versus their aluminum content. The linear trend of the other samples is controlled by the clinopyroxene and spinel in the xenoliths. This could be evidence for Ti- Fe metasomatism at Lunar Crater Maar. Otherwise, it is possible that the Lunar Crater Maar xenoliths have some Fe and/or Ti- rich accessory mineral phase that was not identified in thin section.

Potassium Metasomatism

Potassium (K) metasomatism is produced by alkali-rich fluids escaping from descending plates in subduction zones and interacting with the mantle wedge (Kepezhinskas et al., 1995). K metasomatism can be identified by positive K anomalies on PMn diagrams. Though some of the SW xenoliths' PMn diagrams (Fig. 5) show positive K anomalies, in all cases the values are so close to K detectability levels (Table 3) and hence, the anomalies may not be analytically real. Therefore, very little can be said about K metasomatism in the SW xenolith group. The xenoliths from San Carlos and the Thumb, like those that are known to have experienced K-metasomatism (Fig. 14 d & e), have very slight negative anomalies of Sr and Eu; and a relative enrichment in the most incompatible elements.

Sodium Metasomatism

Sodium (Na) metasomatism is caused by the interaction of felsic (Al-, Na-) rich melts with island arc mantle (Kepezhinskas et al., 1995). Na metasomatism is characterized by positive Nb and Na anomalies on PMn distributions. High La/Yb or high Sr/Yb ratios are also suggestive of Na metasomatism. There is little evidence for the presence of Na metasomatism among the PMn distributions and very few samples have Na values above the detection limits (Fig. 5). The only xenolith that appears to possibly be affected by Na metasomatism is EB-1 from Elephant Butte (Fig. 15f). This sample has positive Ba, K, and Na anomalies as do the samples of xenoliths known to have experienced Na metasomatism.

The Al_2O_3 versus Na_2O plot (Fig. 4e) shows a regular positive linear trend among the xenoliths plotted. PM-1 has greater Al_2O_3 values due to garnet. The linear trend among the other samples is controlled by the clinopyroxene in the samples. Most samples have Na_2O values below the detection level. Therefore, there is no evidence for Na metasomatism in the element ratio plots.

Summary of Metasomatism

The evidence of metasomatism in some of the samples is that the most restitic samples (the ones that should be most depleted in incompatible elements) are the most enriched in regards to incompatible elements. The PMn distributions for these samples suggest that that they are contaminated with an enriched (in incompatible elements) melt; however from both their mineralogy and Mg # (Fig.s 3 & 4a), it is apparent that they are restitic in melt nature.

A possible mechanism to allow for the addition of incompatible elements in the mantle xenoliths might be diffusion during decompression as parts of the lithosphere rose. Many of these samples show reaction rims around minerals that could be attributed to decompression. If there was an incompatible element-rich pore fluid (a pore fluid that was in contact perhaps with the melts that resulted in the formation of the restitic type xenoliths) as the buoyant garnet-free and/or spinel-free restite rises in the mantle, the lithostatic pressure lessens and decompression occurs, allowing a pervasive type fluid flow through the rock via micro-cracks and grain boundaries. To determine if this was the case, a careful study is necessary of the secondary minerals present along the grain boundaries and within fluid inclusions within mineral grains. Unfortunately, these mineral grains are extremely fine-grained and very difficult to properly identify by standard petrographic techniques.

Tectonic Setting and Lithospheric Characteristics

Introduction

One of the main focuses of this project is to characterize the ancient tectonic settings of the upper mantle from the spinel lherzolite xenoliths from the Southwest. It is also important to note how the current tectonic settings of the sample sites affect the xenolith populations.

Modern Tectonic Settings

As previously discussed the mantle xenoliths studied are from a variety of sites throughout the southwestern U.S. and include samples from the Basin and Range Province, the Colorado Plateau Province, and the Transition Zone between these provinces. It might be reasonable to expect that their current tectonic setting play a role in their geochemistry due to factors such as lithospheric heat flow or regional fluid flow. The localities sampled within the Basin and Range are Lunar Crater Maar, Geronimo volcanic field, Potrillo Maar, Kilbourne Hole, and Elephant

Butte (the last three are also part of the Rio Grande Rift). The localities considered from within the Transition Zone are San Carlos, Grand Canyon, and Rio Puerco volcanic necks. The only sample from the Colorado Plateau is the Thumb in the Navajo volcanic field.

In general, most of the Basin and Range xenoliths are depleted in LREE and incompatible elements, except those from Lunar Crater Maar. The Lunar Crater Maar samples are also the least restitic and show little evidence for metasomatism in the REE and PMn distributions.

The xenolith from the Colorado Plateau and those from the Transition Zone are more enriched in LREE and incompatible elements (Fig.s 5 & 6). They are more restitic and their REE and PMn distributions suggest evidence for metasomatism. Greater variation in REE and incompatible element distribution attributed to metasomatism amongst the Transition Zone xenoliths may be due to greater heat flow and fluid flow via fracturing in response to faulting related to the formation of the Rio Grande Rift. The Colorado Plateau is also an area of increased heat flow that could easily affect the metasomatism in the area.

The Al_2O_3 versus SiO_2 graph (Fig. 4d) shows two distinct populations. One trend has higher SiO_2 to Al_2O_3 ratios defined by xenoliths from the Colorado Plateau or the Transition Zone. The other population contains xenoliths that are more closely related to the Basin and Range Province.

Original Tectonic Settings

The original tectonic settings are difficult to constrain from the geochemical data due to metasomatic overprinting. Some observations, however, can be made.

Based on the comparison of REE distributions with melting curves (Fig. 10), it may be possible to attribute some of the xenoliths at Potrillo Maar and Kilbourne Hole as restite from which about a 10% melt of N-MORB composition has been extracted (Fig. 10b). None of the other samples, however, can be interpreted in this manner.

The lack of negative Nb – Ta anomalies among the PMn diagrams (Fig. 5 a, b & f), which is expected at Potrillo Maar, Kilbourne Hole, and the Puerco Necks (based on theories that the mantle should have experienced some mixing with material from subducting slab), does not favor a subduction zone source for the SW xenoliths, although Nb and Ta are low and near their detectability levels. The lack of evidence for Na or K metasomatism also does not suggest such a scenario.

A plot based on clinopyroxenes from spinel lherzolites comparing molar amounts of Al_2O_3 versus Na_2O (Fig. 16a) shows important trends. The data come from published sources cited in the figure caption and other samples that are not from this study are included for comparison. Lunar Crater Maar shows definite arc affinities while San Carlos plots within the plume or the plume/arc transition area.

Lithospheric Characteristics

General zones for Archean and Phanerozoic lithospheres are distinguished on a CaO versus Al_2O_3 graph (Fig. 16b) is also included for the SW xenolith samples. Lunar Crater Maar, Grand Canyon, San Carlos, and the Thumb plot within the accepted range for Archean lithosphere, while the Rio Grande Rift samples plot within the accepted range for Phanerozoic lithosphere.

a)

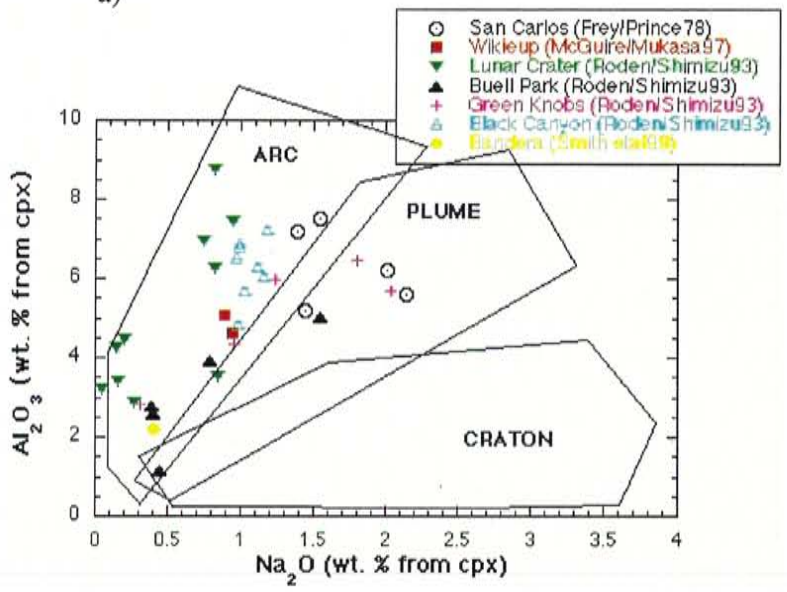

b)

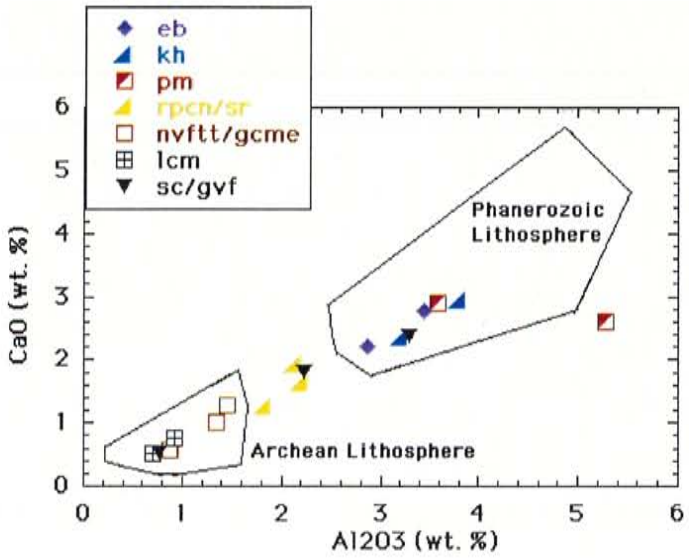

Figure 16 (a & b): Tectonic settings graphs

a) CPX's are from harburgites and lherzolites. References given above. Graph provided by K. Condie, 2001.

b) eb = Elephant Butte, kh = Kilbourne Hole, pm = Potrillo Maar
rpcn/sr = Rio Puerco Necks, nvftt = The Thumb
gcme = Grand Canyon, lcm = Lunar Crater maar
sc = San Carlos, gvf = Geronimo Volcanic Field
PM = Primitive Mantle
Values are whole rock from this study.

There is also evidence in the REE distributions for a heterogeneous mantle beneath Kilbourne Hole as previously discussed. In the REE and PMn distributions (Fig. 5b), two samples are depleted in LREE (Group I) and one is similar to primitive mantle (Group III). It is possible that this is an effect of metasomatism. However, Perry et al. (1988) also suggest a heterogeneous mantle at Kilbourne Hole based on Nd and Hf isotopic concentrations. Roden et al. (1988) also suggest a heterogeneous mantle beneath Kilbourne Hole by means of ^{143}Nd / ^{144}Nd versus ^{87}Sr / ^{88}Sr ratios. From their isotope data, it is suggested that one source is MORB related. However the trace elements show a relative LREE depletion, similar to Kh-1 and Kh-1-Joc in this study (Group I xenoliths, with a likely athenospheric source) (Roden et al., 1988). The second source of Roden et al. (1988), based on the isotope data, is non-MORB, possibly related to sample Kh-2 (Group III). Roden et al. (1988) suggest two possible models: multiple depletion events, or mixing of mantle sources.

Additionally, San Carlos appears to show evidence from this study of a heterogeneous mantle source. The San Carlos evidence comes from SC-1 xenolith and a sample analyzed by Jochum et al. (1989). These two xenoliths have different trace element distributions. The sample from Jochum et al. (1989) is similar to primitive mantle (this study's Group III). The xenolith from this study shows enrichment in the most incompatible elements (Group IV).

One of the most important implications of the trace element distributions is that the xenoliths seem to be sampling distinct mantle sources (Fig. 17 shows their spatial / regional relationship). The sources include two LREE depleted sources, a LREE enriched source, and a source similar to primitive mantle estimates (Fig. 18). Group I (Fig. 18a) shows a relatively strong depletion in the most incompatible elements. Group II (Fig. 18b) shows a more regular depletion as incompatibility increases. The xenoliths of Group II are more depleted but show distributions similar to the restite expected after removal of a 5% melt of N-MORB suggested by Walter (1999). Group III (Fig. 18c) exhibits a horizontal trend similar to that of primitive

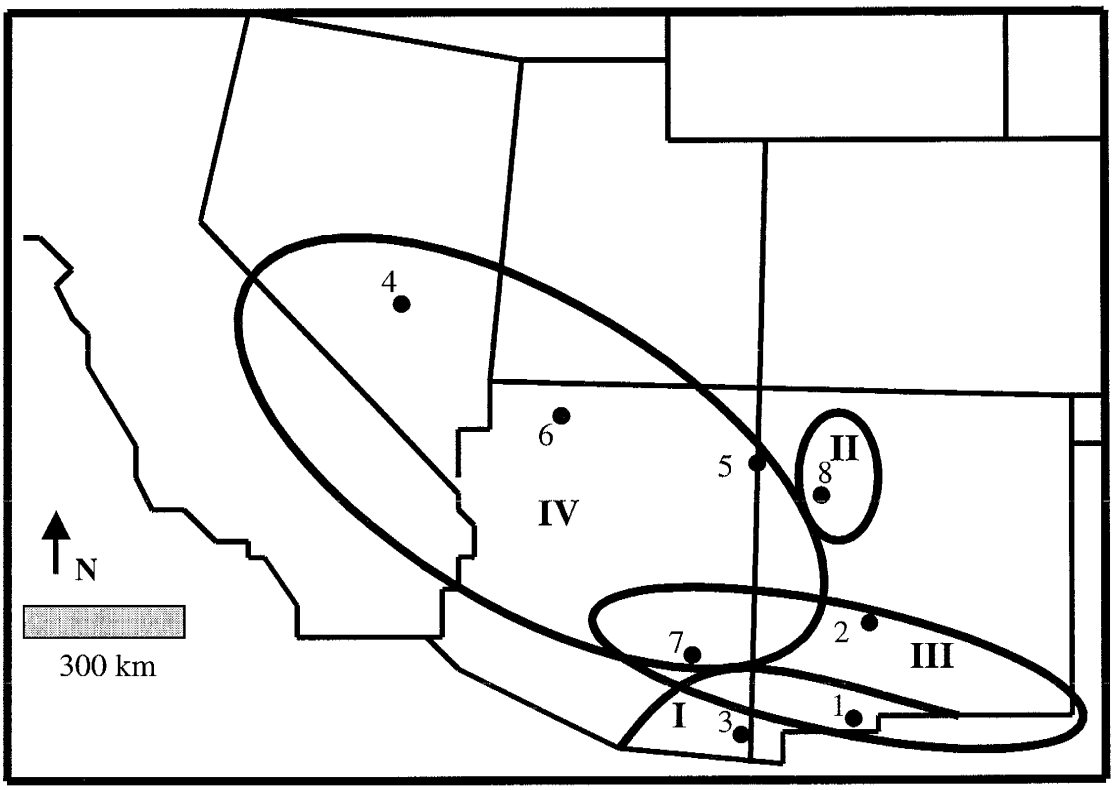

Figure 17: Map of xenolith sites in Southwest United States with mantle sources from this study shown.
Group I = Strong relative depletion in the most incompatible elements,
Group II = Relative depletion in the most incompatible elements,
Group III = Horizontal trend similar to primitive mantle, and
Group IV = Relative enrichment in the most incompatible elements

1. Potrillo Maar & Kilbourne Hole, Potrillo volcanic field
2. Elephant Butte
3. Geronimo volcanic field
4. Marcath Flow, Lunar Crater Maar
5. The Thumb, Navajo volcanic field
6. Mount Emma, Grand Canyon
7. San Carlos
8. Rio Puerco Necks, Mount Taylor volcanic field

mantle as suggested by Sun and McDonough (1989). Group IV (Fig. 18d) shows a relative enrichment in the most incompatible elements (Ocean Island Basalt (OIB) is included for comparison).

From this study the groupings appear spatially related but this could be an artifact of sampling (i.e. there could be more variation in groups present at each site but this study was limited to one or two xenoliths per locality). There appears to be some overlap of upper mantle sources for xenoliths from the same site (Fig. 17). In some cases, xenoliths seem to have been derived from different mantle sources at the same location such as Kilbourne Hole and San Carlos.

It appears that the xenoliths from Group I and Group III are related to athenospheric mantle sources (Livacarri & Perry, 1993) (Fig. 1 & 17). Group IV xenoliths sample both the athenospheric and lithospheric mantle sources, while Group III probably comes from the lithospheric mantle source (Livacarri & Perry, 1993). However Group III is extremely close to the suggested athenospheric mantle source (Livacarri & Perry, 1993).

Ongoing Work

It has been discovered that a majority of the REE and HFSE reside in the grain boundary alteration, not in the major minerals (K. Condie, 2002, Pers. Communication). Depending on the method in which the grain boundary alteration occurred, this could have some implications in this study's discussion and conclusions.

Other studies have noted the same phenomenon of grain boundary microphases controlling trace element signatures. Bedini and Bodinier (1999) used mineral separates and leachates of grain boundary microphases to determine where trace elements are housed in upper mantle

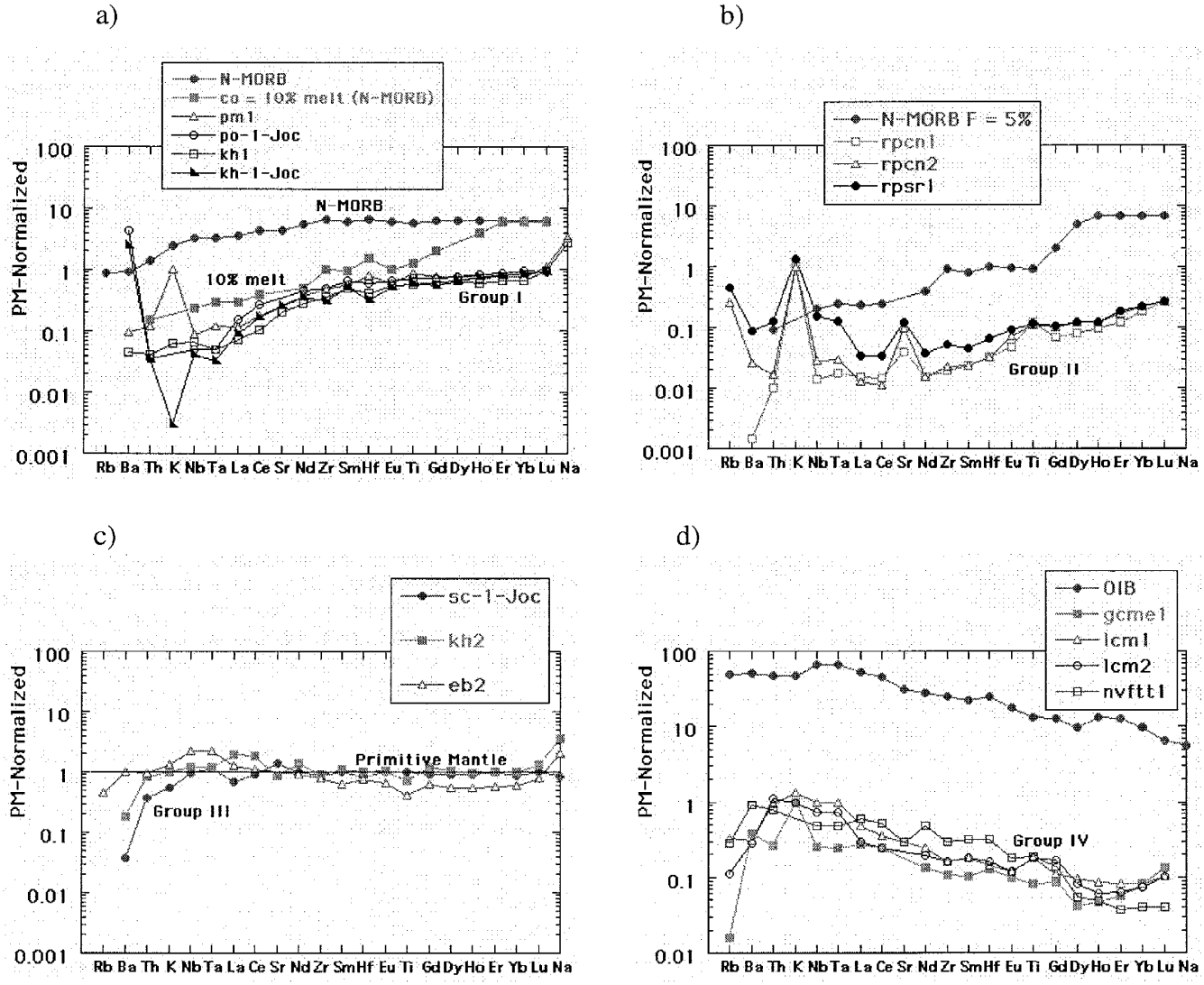

Figure 18: Incompatible element distributions compared to average known source materials. Known sources from Sun and McDonough, 1989.
Abbreviations are as follow:
N-MORB = N-type Mid-Ocean Ridge Basalt, OIB = Oceanic Island Basalt
gvf = Geronimo volcanic field, kh = Kilbourne Hole
sc = San Carlos, eb = Elephant Butte
gcme = Grand Canyon, lcm = Lunar Crater Maar

xenoliths. Bedini and Bodinier (1999) conclude that silicate minerals account for the total HREE abundances, 50 –90% of the LREE, Sr and Zr – Hf in apatite free samples. Mineral hosted fluid inclusions house about 20 – 25% Rb and to lesser degrees for the other LILEs (Bedini and Bodinier, 1999). Grain boundary microphases are selectively enriched the most incompatible elements and house 25 – 90% of the whole rock budget of Th, U, and Sr, as well as 10 – 50% of Nb and LREE (Bedini and Bodinier, 1999).

The textures of the Southwest xenoliths also may reflect the distribution of certain trace elements. Deformed (tabular grained) xenoliths form channels for fluids to move through and precipitate secondary minerals (Bedini and Bodinier, 1999). Bedini and Bodinier (1999) noted that the deformed xenoliths from their study are more enriched in LILE. Specifically, granular xenoliths have lower LILE to HREE ratios than deformed xenoliths.

If one believes that the grain boundary microphases are produced in the mantle possibly as a result of the volcanic event that carried the xenolith to the surface, then the grain boundary microphases are dependant on the mantle source from which a xenolith is derived. But if one believes that grain boundary microphases are emplaced post-eruption or during the travel time through the crust or other crustal processes, then the elemental distributions are not necessarily related to the mantle source.

In this case, the grain boundary microphases may be related to the characteristics of the crust or of the volcanic event that brought the xenolith to the surface. There is little evidence based on the geochemical groupings that eruption style has any effect on the geochemistry of the signatures. There is no evidence that transport mechanismn has any affect on the xenolith's geochemical composition. Xenoliths from the two sites that are volcanic necks do not share similar elemental distributions and the basalt flows and the volcanic fields contain xenoliths from all groups except Group II.

VI: Conclusions

1) Textural evidence for metasomatism in the spinel lherzolite mantle xenoliths from the Southwest include: 1) some micro-fractures are filled with secondary minerals, 2) decompression reaction rims on pyroxene and olivine,grains and 3) some grain boundaries contain fine-grained microphases.

2) None of the known mantle metasomatic styles (carbonatite, Na, Fe, or Ti) can wholly be responsible for any of the xenolith trace element signatures. Irregular incompatible element distributions with positive Ti anomalies suggest that xenoliths from Lunar Crater Maar may have been affected by Ti-metasomatism. Grand Canyon xenoliths appear to have undergone one or more metasomatic events as evidenced by highly irregular incompatible element distributions. There is no evidence for carbonatite metasomatism based on incompatible element distributions and Ca/Al and Ti/Eu ratios.

3) There is little evidence that current tectonic settings have much affect on the geochemical signatures of the spinel lherzolite xenoliths. There does, however, seem to be greater variation in the composition of xenoliths from the Rio Grande Rift and the southern Basin and Range than from Colorado Plateau and Great Basin Provinces.

4) There is no evidence that transport mechanism of xenoliths to the surface affects trace element distributions of the southwest xenoliths.

5) Major element diagrams based on weight percent oxides show that Lunar Crater Maar xenoliths have arc affinities, and xenoliths from San Carlos have arc or arc/plume transition characteristics. Tectonic affinities of xenoliths from other localities are nondefinitive.

6) Major element analyses show groupings based on batch melt extractions and pressures. Southern Basin and Range xenoliths have batch melt extraction less then 20% with pressures of about 1 GPa. Xenoliths from the Colorado Plateau and northern Basin and Range sites show batch melt extraction of 20 – 40% and pressures up to 4 GPa. Lunar Crater Maar and San Carlos samples have batch melt extractions of about 30% and 1 GPa pressure.

7) Since metasomatism, current tectonic regimes, and eruptive styles seem to have little effect on the trace element distributions, it can be assumed that the variations in the trace element distributions are due to source differences. The xenoliths fall into four distinct mantle source groupings based on their trace element distributions. Group I shows strong depletion in the most incompatible elements; this group occurs in the southern Basin and Range and the Rio Grande Rift Provinces. Group II xenoliths show progressive depletion as incompatibility of elements increase; this group is occurs only in the Mt. Taylor volcanic field in New Mexico. Group III

xenoliths have incompatible element distributions similar to primitive mantle and these xenoliths occur in the southern Basin and Range and Rio Grande Rift, overlapping Groups I and IV. Group IV xenoliths show relative enrichment in the most incompatible elements and occur in the Great Basin, Colorado Plateau, and southern Basin and Range.

8) Trace element distributions in the spinel lherzolites from Group I are similar to restite with 10% melt of N-MORB composition having been removed. Elemental distributions in Group III xenoliths are similar to those of primitive mantle (Sun & McDonough, 1989). Group IV xenoliths show incompatible element patterns similar to the source of OIB, but depleted by at least 2 orders of magnitude.

9) Both Kilbourne Hole and San Carlos xenoliths have trace element signatures that are distinct from one another suggesting multiple mantle sources at these localities. Also, it is of interest to note that the mantle source groupings are not exclusive to single localities.

Appendices

Appendix A: Basic Igneous Geology maps for Southwest Xenolith Collection

Appendix B: Petrography: Thin Section Descriptions

Appendix C: Analytical Methods

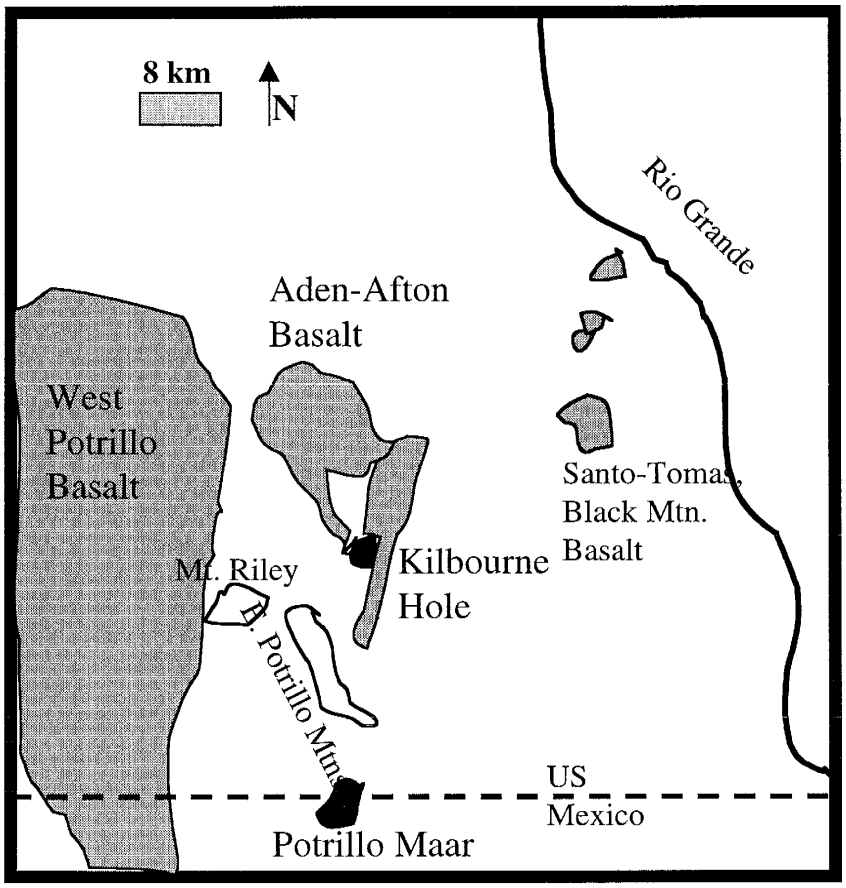

Map of Potrillo Volcanic field and other sites of interest.
Black sites are those sampled for this study, gray sites are basalt flows and other igneous localities in the area.
From Hoffer, 1975

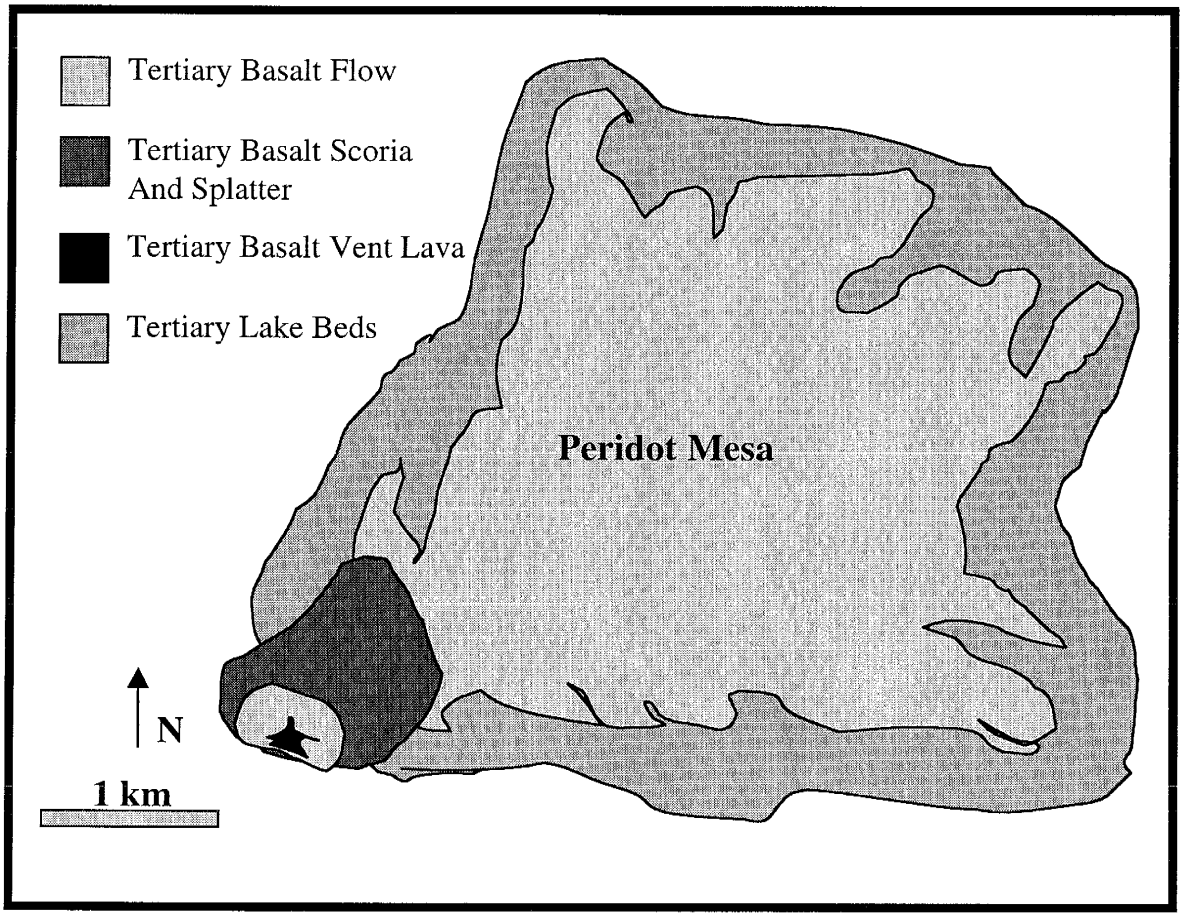

Map of the San Carlos volcanic area.
Based on a map by Ken Wolletz, 1977

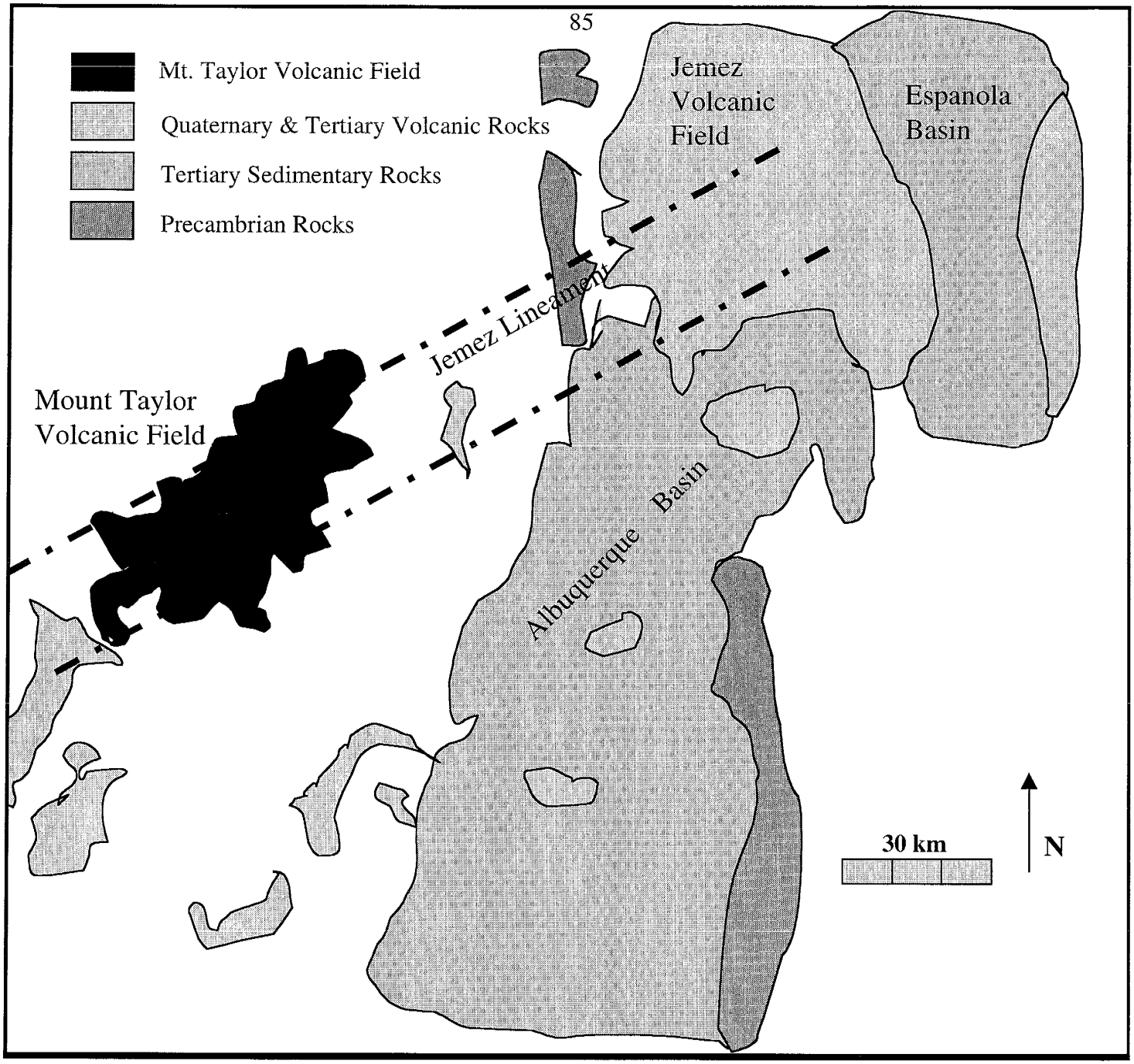

Map of Mount Taylor volcanic field and other local spots of interest.
From Pazzaglia et al., 1999

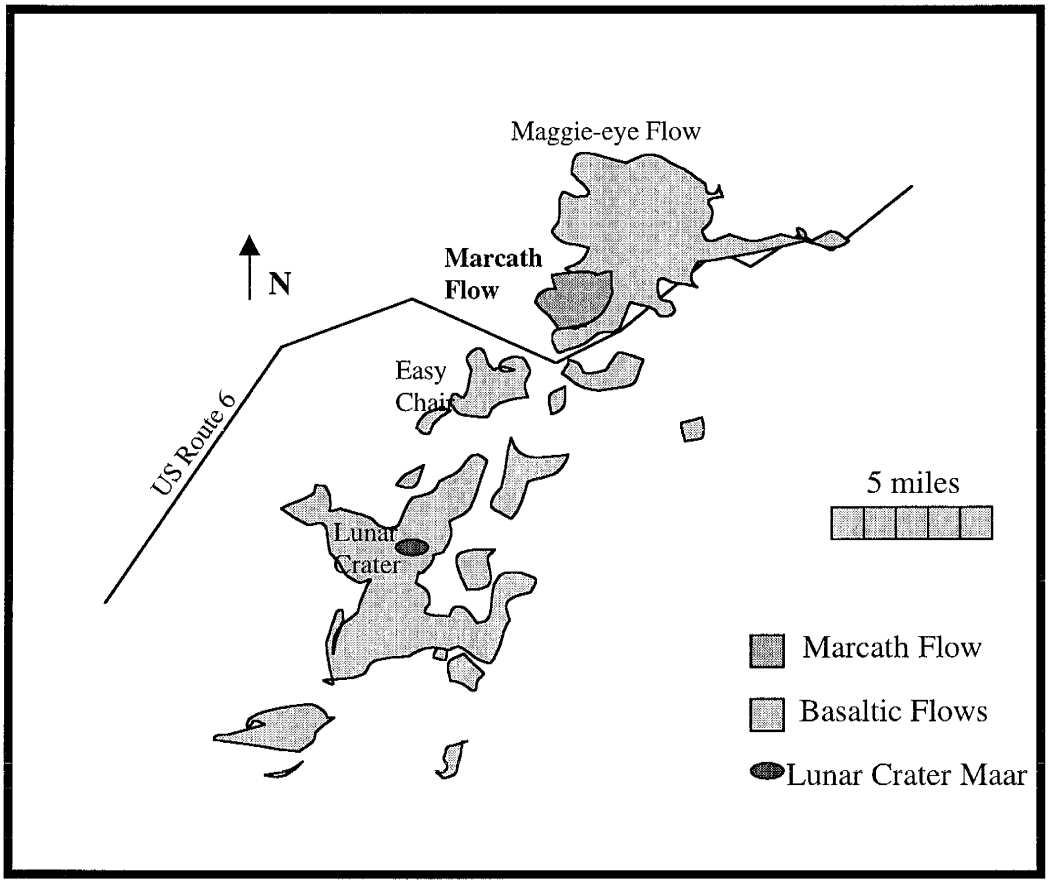

Map of Lunar Crater Maar showing lava fields. Marcath flow is slightly darker and was the site sampled in this study.

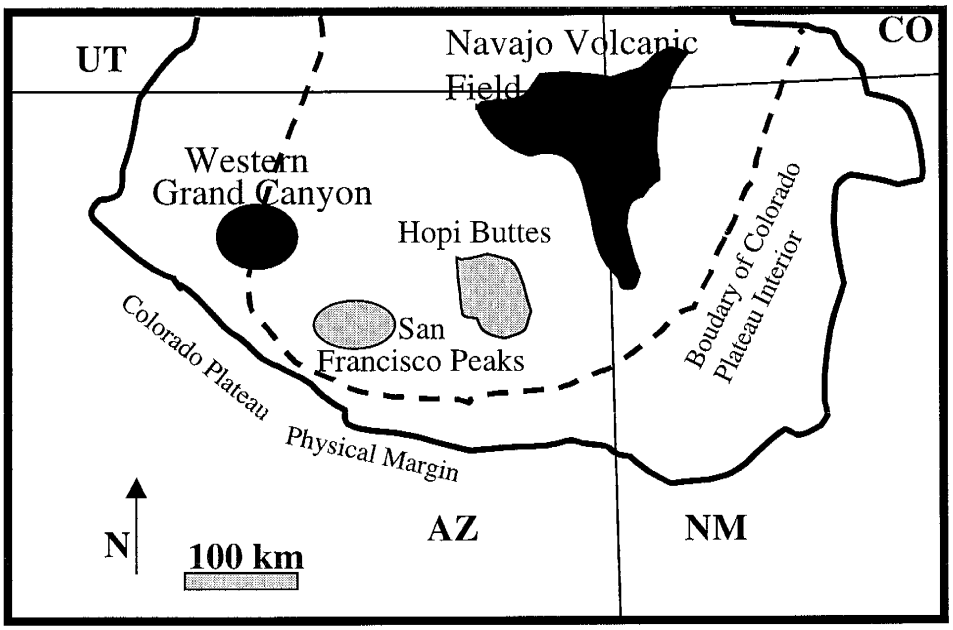

Map of Navajo volcanic field and Grand Canyon volcanic area and other sites of interest.
Black sites are those sampled for this study. Gray sites are other igneous localities in the area.
Map after Alibert et al., 1986
Boundary of Plateau interior from Zoback & Zoback, 1980

Appendix B: Petrography

Introduction

Seventeen thin sections were made from the seventeen samples used in this study. The summaries below include the modal mineral percentages and other petrographic and textural details that may be of interest. After the individual thin section descriptions, there are sections on various signs of alteration or metasomatism.

Most of the samples used in this study are spinel lherzolites. The basic lherzolite mineralogy is olivine, both ortho and clino pyroxenes, and accessory minerals such as spinel or garnet.

Petrographic Summaries

Potrillo Maar

Sample PM-1 is a spinel lherzolite with a modal distribution of 50% olivine, 25% orthopyroxene, 15% clinopyroxene, about 5% spinel, and 5% fracture fill (which includes oxides, glass/isotropics, and sericite). There is about 1% modal primary garnet. Texturally this sample shows equilibrium triple junctions, poikolitic pyroxenes with olivine & spinel, also pyroxene in spinel; and reaction rims on the pyroxenes.

Sample PM-2 is a spinel lherzolite with a modal distribution of 50% olivine, 30% orthopyroxene, 10% clinopyroxene, <5% spinel; and 5% opaques (oxides), glass and maybe some iron carbonate. Texturally the sample exhibits poikolitic texture with olivine and spinel in pyroxenes, alignment of mineral long axes, reaction rims on pyroxenes and olivine, and there were also some inclusion tracks some are melt inclusions.

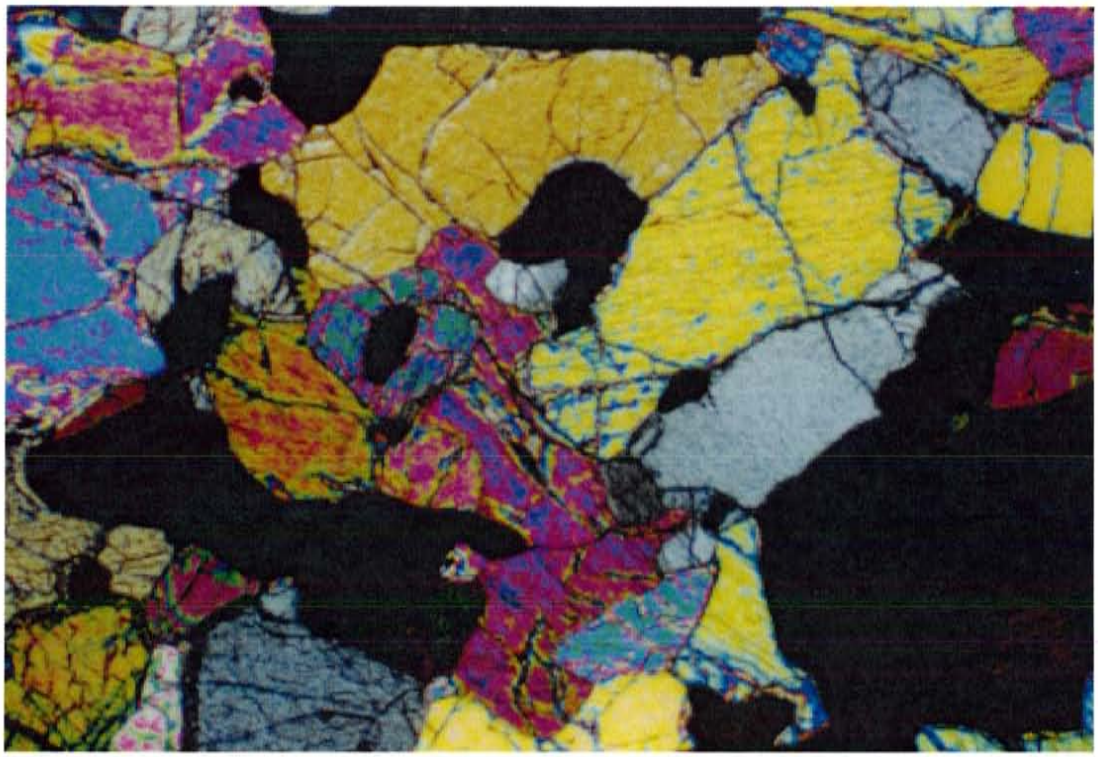

Texture Picture for PM-1, 10 X power, XPL

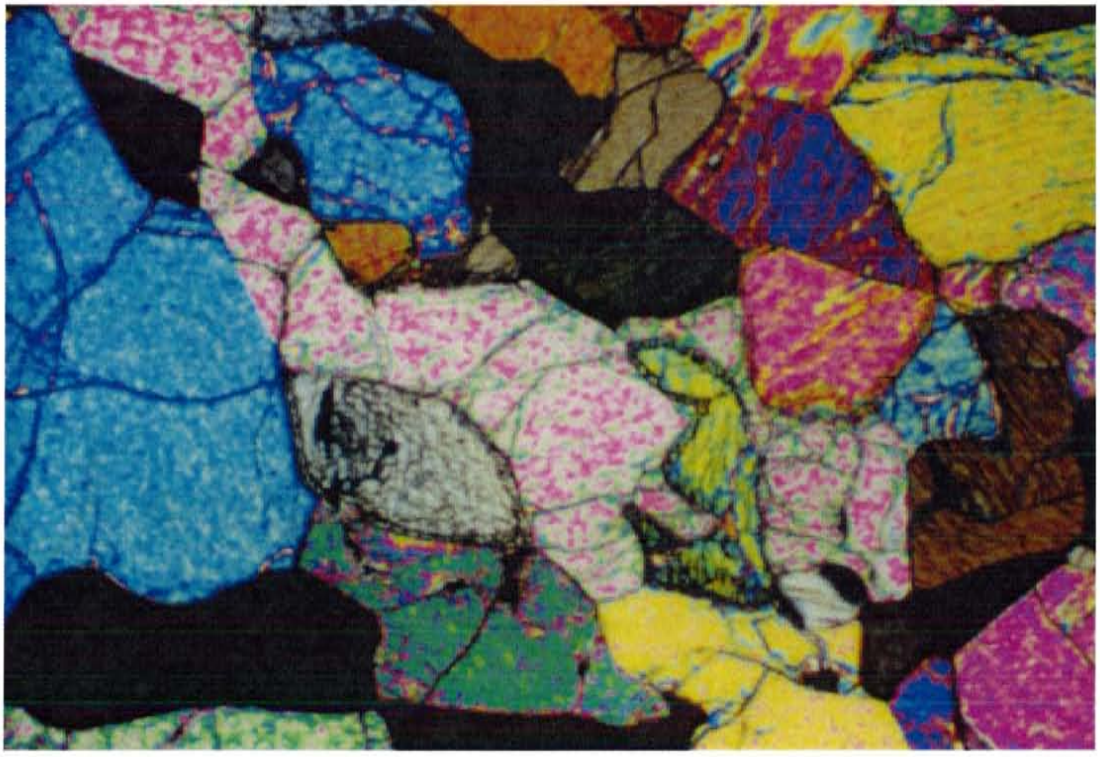

Texture Picture for PM-2, 10X, XPL

Kilbourne Hole

The sample KH-1 is a spinel lherzolite with a modal distribution of 50% olivine, 40% orthopyroxene, 5% clinopyroxene, about 3% spinel; and 2% secondary minerals along grain boundaries and as fracture fill including some glass and possibly some quartz. This sample shows equilibrium triple junctions, dissolution of some grain boundaries, poikiloblastic texture with orthopyroxene bearing orthopyroxene, olivine, and spinel; and possible some melt pockets.

Sample KH-2 is a spinel lherzolite with a modal distribution of 45% olivine, 35% orthopyroxene, 5% opaques and oxides as fracture fill, <5% clinopyroxene; and <5% spinel. Texturally this sample exhibits equilibrium triple junctions, reaction rims on olivine and orthopyroxene, and large scale fracturing. There are some grains that have formed pseudomorphs that are now containing $CaCO_2$, $FeCO_2$, some oxides, and glass/isotropics. There are some occurrences of poikiloblastic spinel bearing olivine.

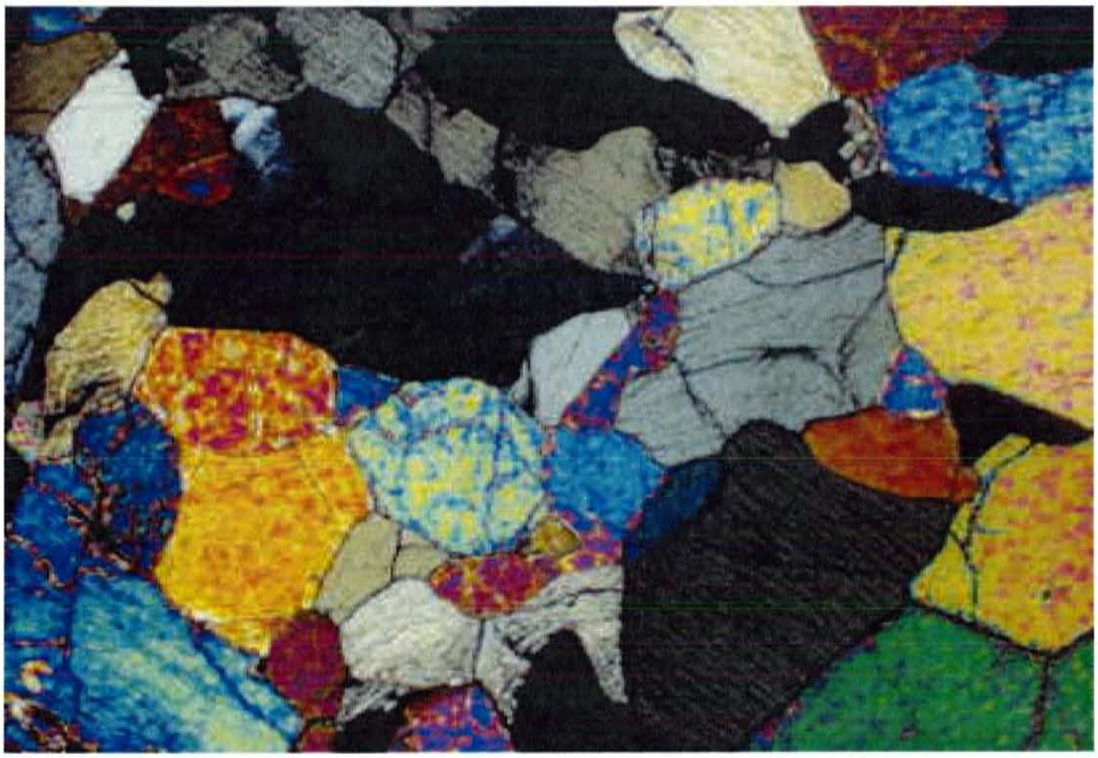

Texture Picture for KH-1, 10X, XPL

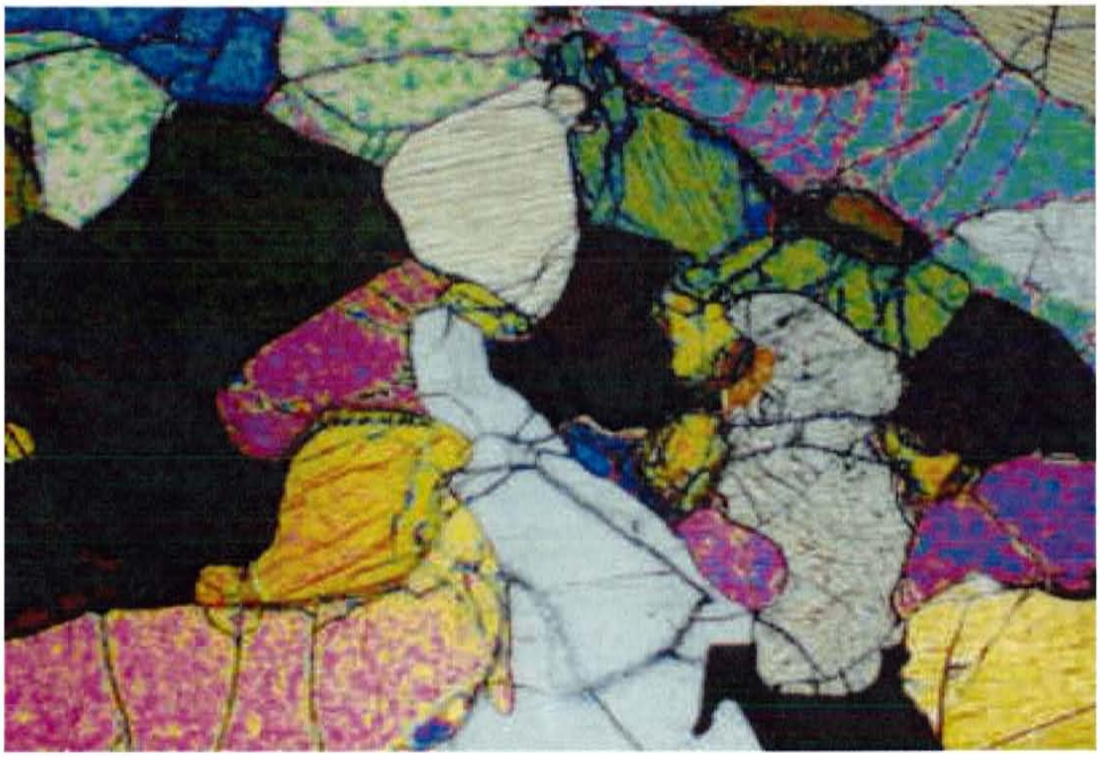

Texture Picture for KH-2, 10X, XPL

Elephant Butte

Sample EB-1 is a spinel lherzolite with a modal distribution of 50% olivine, 20% orthopyroxene, 20% clinopyroxene, 5% fracture fill; and <5% spinel. Texturally this sample shows equilibrium triple junctions, poikiloblastic pyroxene with pyroxene, olivine & spinel, poikoblastic olivine bearing olivine, and large scale fracturing with carbonate and oxide fill. There is some grain boundary and crystal plane alteration including $CaCO_2$, $FeCO_2$, and some oxides. There maybe some recrystallization of pyroxene and olivine grains. Some inclusion tracks are apparent, some may be melt inclusions.

Sample EB-2 is a lherzolite with a modal distribution of 55% olivine, 20% orthopyroxene, 20% clinopyroxene; and 5% fracture fill. The textures apparent in this section include equilibrium triple junctions, some poikiloblastic pyroxene with olivine & pyroxene, some poikiloblastic olivine with olivine, large scale fracturing filled by carbonate and opaques; and some inclusion tracks (some of which maybe melt). There is grain boundary and crystal plane alteration that includes $CaCO_2$, $FeCO_2$, some oxides, and glass/isotropic. There are some areas where serpentization or sericitization seem to have occurred.

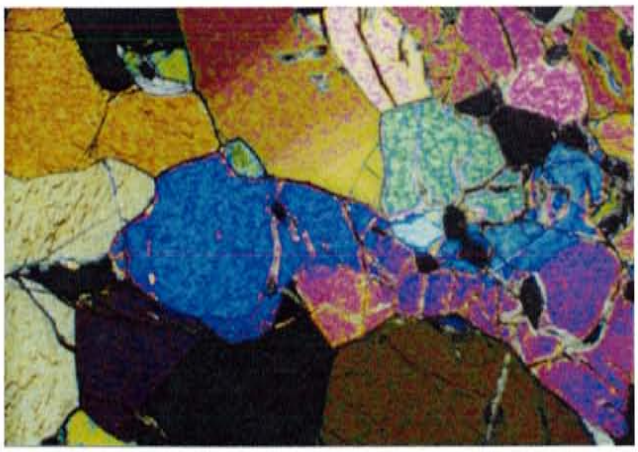

Texture Picture for EB-1, 10X, XPL

Texture Picture for EB-2, 10X, XPL

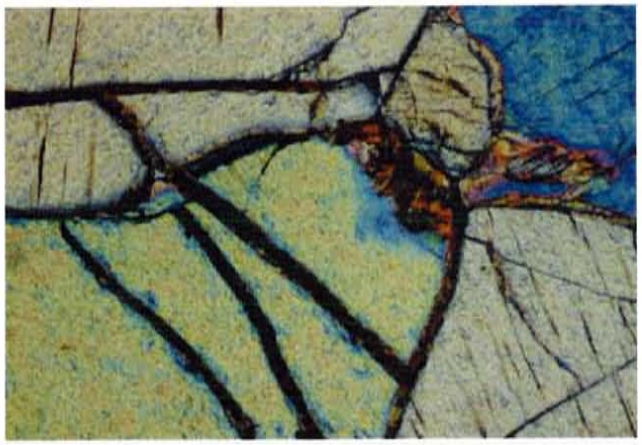

EB-1 oxide rich veining around and through grains, 20X, XPL

Geronimo Volcanic Field

Sample GVF-1 is a spinel lherzolite with a modal distribution of 60% olivine, 25% orthopyroxene, 10% clinopyroxene; and <5% spinel (2 phases). Texturally this sample shows equilibrium triple junctions, embayment of grain boundaries, reaction rims, and alignment of mineral long axes. There are some zones of pervasive alteration that include glass/isotropics, oxides, carbonates, and possible plagioclase glomercrysts. There is melt pockets within fractures. The two phases of spinel include a primary phase that seems to predate olivine and pyroxene and a secondary phase occurring within fractures.

Sample GVF-2 is a spinel lherzolite with a modal distribution of 50% olivine, 23% orthopyroxene, 23% clinopyroxene; and 3% spinel. The textures apparent in this thin section include equilibrium triple junctions, poikiloblastic pyroxene with olivine & pyroxene, and oversized pyroxene grains.

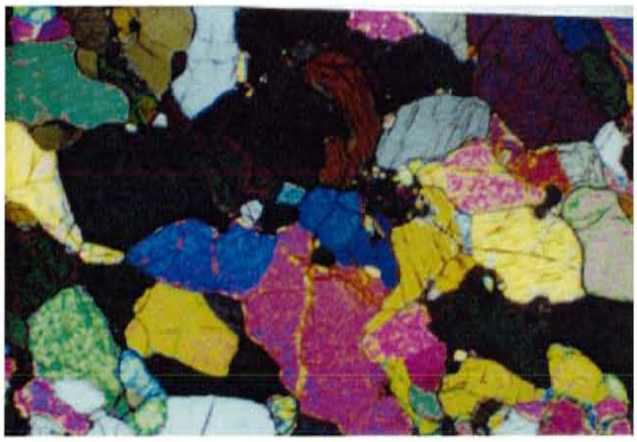

GVF-1 Texture picture, 10X, XPL

GVF-1 Picture of glass pocket, 20X, PPL

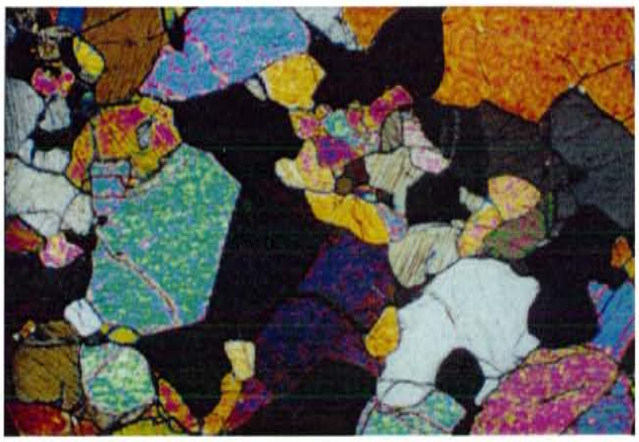

GVF-2 Texture picture, 10X, XPL

Lunar Crater Maar: Marcath Flow

Sample LCM-1 is a (spinel) lherzolite with a modal distribution of 65% olivine, 15% orthopyroxene, 15% clinopyroxene, <5% fracture fill; and <1% spinel. Texturally this sample shows equilibrium triple junctions, embayment of grain boundaries, poikiloblastic pyroxene with olivine & pyroxene, some oversized olivine grains, pyroxene appears to form compositional bands; and large scale fracturing filled by carbonate. There is some recrystallized olivine that occurs around grain boundaries. There are also some inclusion tracks, some of which are probably melt inclusions.

Sample LCM-2 is a lherzolite with a modal distribution of 60% olivine, 25% orthopyroxene, 10% clinopyroxene; and 5% fracture fill. Texturally this sample shows equilibrium triple junctions, poikoblastic olivine with pyroxene & olivine, reaction rims, some pyroxene grains have inclusion tracks (some may be melt inclusions, inclusions in general are most common in pyroxenes), grain size varies for all minerals (including some very oversized olivine & pyroxene grains); and the sample may show some banding. The secondary alteration includes zones of oxides, carbonates, and some plagioclase grains.

LCM-1 Texture picture, 10X, XPL

LCM-2 Texture picture, 10X, XPL

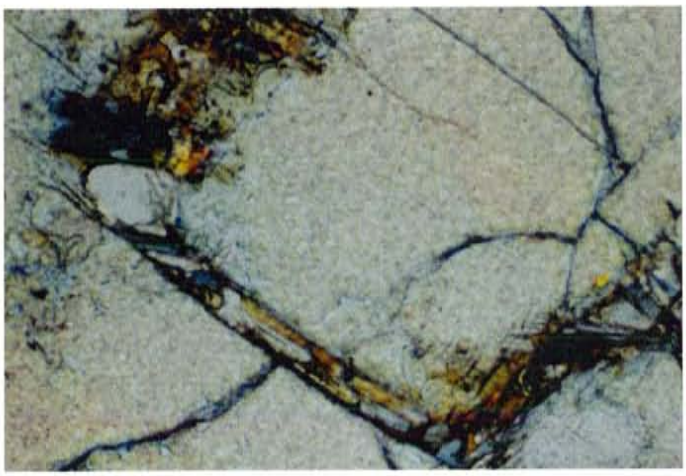

LCM-2, Crystal plane/ internal fracture oxide-rich vein, 20X, PPL

Navajo Volcanic Field: The Thumb

Sample NVFTT-1 is a lherzolite with a modal distribution of 65% olivine, 20% orthopyroxene, 10% clinopyroxene; and 5% opaques, oxides, and isotropics. The textures apparent in this sample include some equilibrium triple junctions but mostly curved or irregular grain boundaries, poikiloblastic texture of both olivine in pyroxene and pyroxene in olivine; and the sample may be banded and the opaques appear to favor the areas of prevalent pyroxene. Some zones of prevalent pervasive alteration exist in this sample secondary alteration minerals include carbonates, chlorite (maybe), glass/isotropics, and some oxides. The alteration causes pseudomorphs of what is now carbonate to occur.

San Carlos

Sample SC-1 is a (spinel) lherzolite with a modal distribution of 50% olivine, 30% clinopyroxene, 20% orthopyroxene; and <2% spinel. Texturally this sample shows equilibrium triple junctions, poikiloblastic pyroxene bearing pyroxene & olivine, poikiloblastic olivine bearing pyroxene, exsolution in larger orthopyroxene grains; and grain size variance amongst all the minerals.

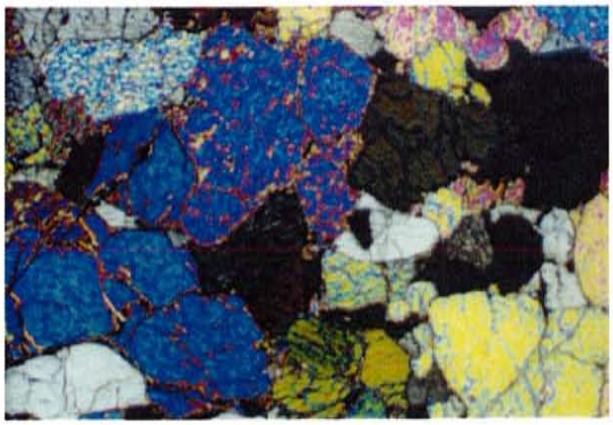

NVFTT-1 Texture picture, 10X, XPL

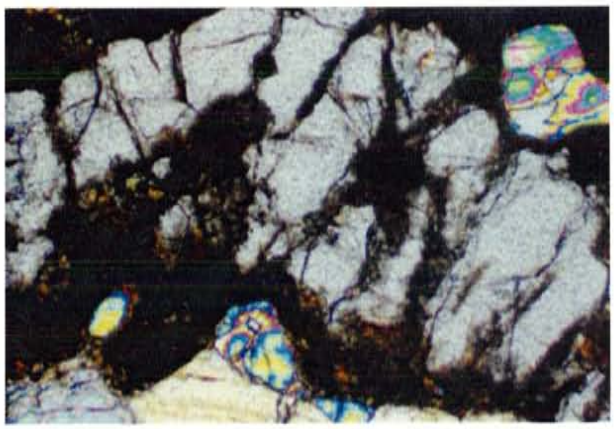

NVFTT-1 Grain boundary alteration (oxide-rich), 20X, XPL

SC-1 Texture picture, 10X, XPL

Grand Canyon: Mount Emma

Sample GCME-1 is a spinel lherzolite with a modal distribution of 60% olivine, 15% orthopyroxene, 15% clinopyroxene, <4% spinel; and >6% fracture fill. Texturally this sample shows equilibrium triple junctions but also curved and irregular grain boundaries, poikiloblastic texture of both olivine & pyroxene in pyroxene and a pyroxene in olivine, also small red crystals included in both olivine and pyroxene (maybe siderite) and there was also a degree of grain size variance. There is some evidence for pervasive alteration causing pseudomorphs to occur into what is now probably an oxide rich carbonate. There is also grain boundary and fracture filling alteration that includes various carbonates, oxides, glass, and some plagioclase. There are some pyroxene grains showing exsolution. Some olivine and iron carbonate recrystallizations.

Sample GCME-2 is a spinel lherzolite with a modal distribution of 60% olivine, 25% orthopyroxene, 16% clinopyroxene; and <4% spinel. Texturally this sample shows equilibrium triple junctions, sutured grain boundaries, spinel concentrated in areas of prevalent pyroxene, some inclusion tracks (some maybe melt inclusions) especially in olivine; and olivine grains show variable size. Pervasive alteration is evident due to pseudomorphs including what are now carbonates, oxides, and possibly some recrystallized olivine. There are the same fine-grained red crystals included in the olivine and pyroxene.

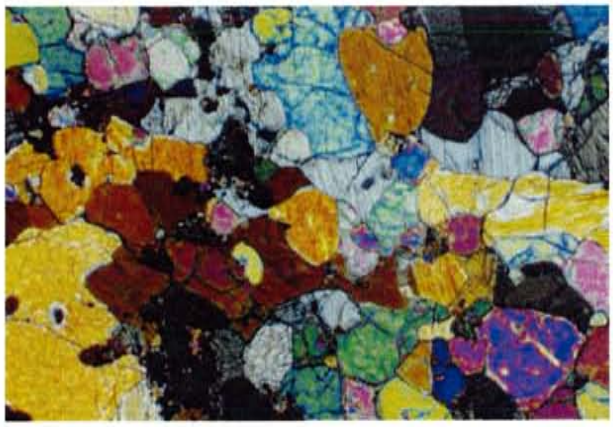

GCME-1 Texture picture, 10X, XPL

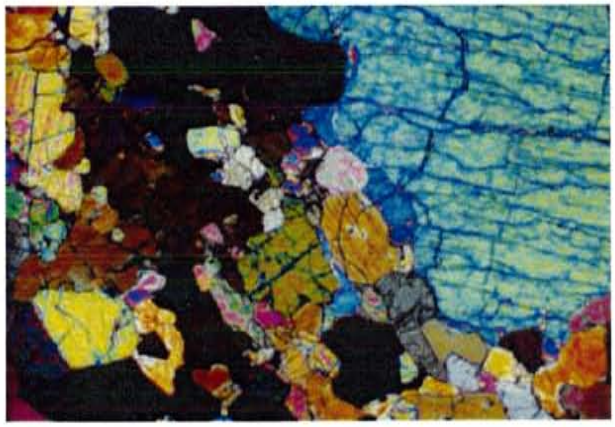

GCME-2 texture picture, 10X, XPL

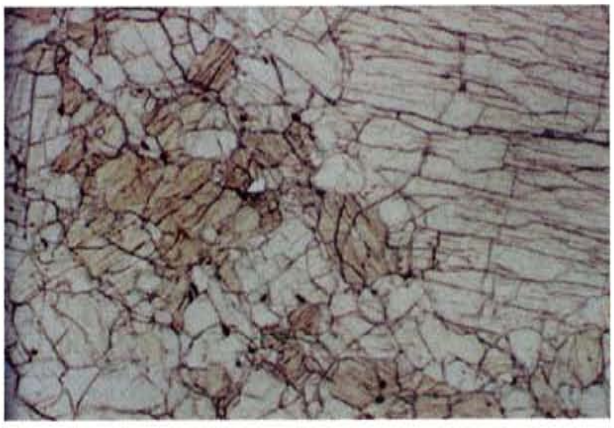

GCME-2 Texture picture same view as above in PPL, note variation in color and fine-grained spinel.

Rio Puerco Volcanic Necks: Cerro Negro & Santa Rosa

Sample RPCN-1 is a spinel lherzolite with a modal distribution of 60% olivine, 25% clinopyroxene, 5% orthopyroxene, <4% spinel; and >6% fracture fill. Textures apparent in this thin section include equilibrium triple junctions, curved grain boundaries, poikoblastic pyroxenes with olivine & pyroxenes, some poikoblastic olivine with pyroxene & olivine, clustered spinel, exsolution within the pyroxenes, some inclusion tracks (some maybe melt inclusions) within the olivine; and the fracture fill is composed of carbonate and sericite. There is also some grain boundary and fracture filling alteration that is mostly carbonate.

Sample RPCN-2 is a spinel lherzolite with a modal distribution of 50% olivine, 25% clinopyroxene, 15% orthopyroxene, >6% fracture fill; and <4% spinel. Texturally this sample shows equilibrium triple junctions, inclusion tracks (some of which maybe melt inclusions) in olivine and pyroxene, and poikoblastic pyroxenes bearing pyroxenes & olivine. Some grains have been replaced by serpentine and/or chlorite as pseudomorphs; and fracture fill includes carbonate, serpentine, opaques, and quartz. There is some grain boundary and crystal plane alteration that includes chlorite and/or sericite.

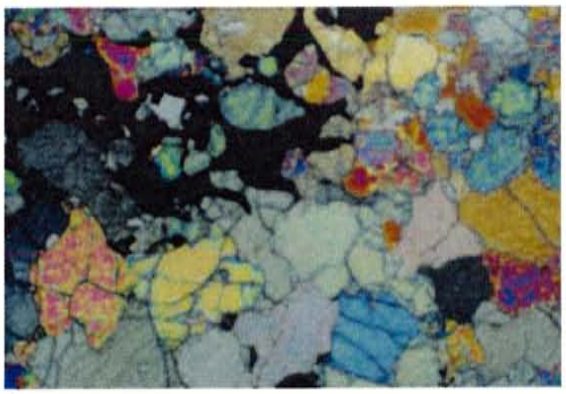

RPCN-1 Texture picture, 10X, XPL

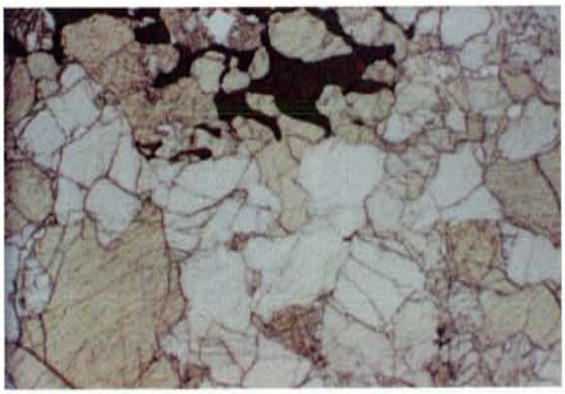

RPCN-1 Texture picture slightly unaligned but same area as above PPL, note variation in grain color and intercumulus grouping of spinel.

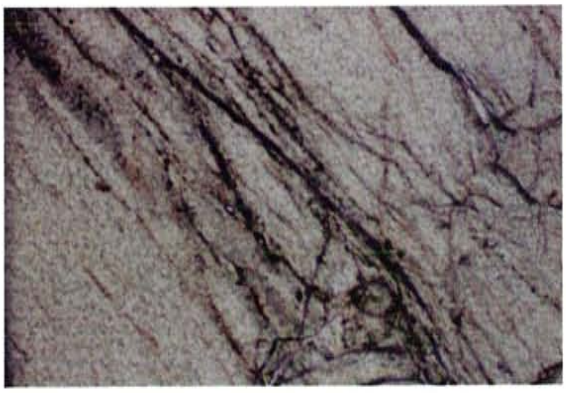

RPCN-1 Picture of inclusion tracks and fractures, 20X, XPL

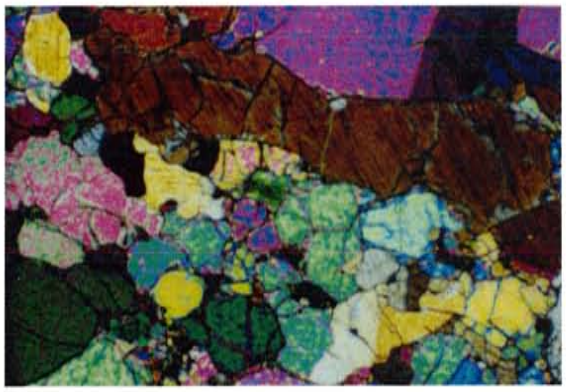

RPCN-2, Texture picture, 10X, XPL

RPCN-2, Texture picture, 10X, PPL, note oxide-rich pervasive alteration

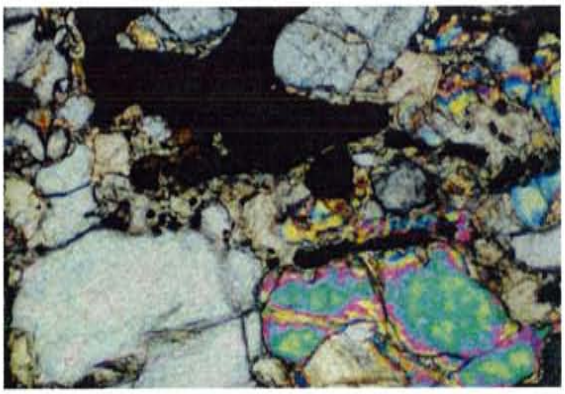

RPCN-2, Alteration picture, 20X, XPL

Sample RPSR-1 is a spinel lherzolite with a modal distribution of 60% olivine, 20% clinopyroxene, 10% orthopyroxene, <4% spinel; and >6% fracture fill. Texturally this sample shows equilibrium triple junctions, deformation bands, poikiloblastic pyroxene with olivine & pyroxene, darkened channels of alteration, psuedomorphed grains, inclusion tracks (some of which maybe melt inclusions) within olivine and pyroxene; and a zone of carbonatization bearing grain sized carbonate. The zone of carbonatization is evidence of pervasive alteration and contains calcium and iron carbonates, oxides, and some probable rutile crystals.

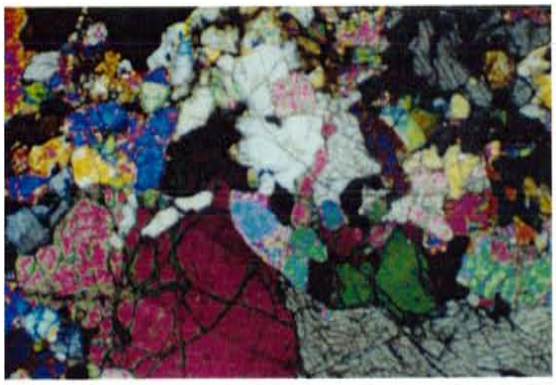

RPSR-1 Texture picture, 10X, XPL

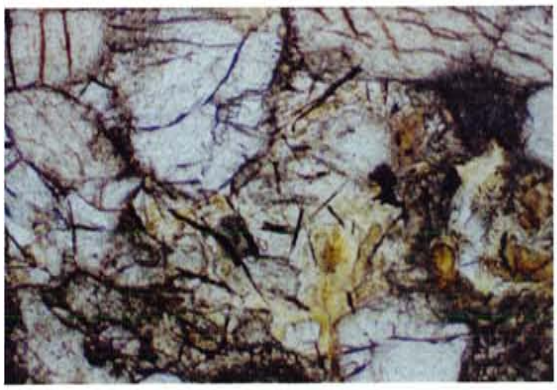

RPSR-1 Zone of pervasive alteration, oxide-rich, silicate minerals

Secondary Minerals

Introduction

One means of introducing secondary minerals into a rock is through the process of metasomatism. Metasomatism is alteration that affects the geochemistry of the minerals involved. Metasomatism generally involves fluid flow processes and travels along fracture conduits. Alteration minerals include those that are easily carried and redeposited by fluids, or are caused by interaction of minerals with fluid.

Carbonate Mineralization

Carbonate mineralization is found in several samples as larger scaled fracture veining, pseudomorphs, grain boundary mineralization, or micro-veining (small scale veining present in solitary mineral grains): EB-1 & 2, RPCN-1 & 2, RPSR-1, GCME-1; and LCM-1 & 2. Some of the carbonate present in these samples may be iron rich carbonate based on its orange or brown colors in plain light. Sample RPSR-1 has a zone of carbonitization; this zone of carbonitization implies that fluid flow permeated through the rock itself rather then in fractures. This would allow for greater interaction with in situ mineral grains.

Opaque and Oxide Mineralization

Opaque minerals are hard to distinguish and properly identify without using reflected light techniques. In general, opaques tend to be oxides or sulfides that might be attributed to some magmatic type fluid source. Some of these sample show opaques and oxides within larger scaled fracture veining, others as grain boundary mineralization, and some appear to be

intercumulus or primary. Samples that contained opaques or oxide minerals include EB-1, NVFTT-1, LCM-2, PM-1, RPCN-2, RPSR-1; and KH-1.

Retrograde Alteration

Retrograde alteration type minerals found in samples RPCN-1 & 2 include serpentine, chlorite, and sericite. Retrograde alteration is associated with low temperature, low pressure regimes with ample fluid available for mineral degradation. Retrograde minerals can either be transported by fluids and then precipitated within larger scaled fractures forming veins, within individual grains as micro-veining, along grain boundaries, or can occur by altering in situ grains within a sample forming pseudomorphs.

Fluorite Mineralization

Fluorite may be present in samples RPCN-1 & 2. Fluorite is an obvious sign of minerals transported and deposited within larger scaled fractures or along grain boundaries because fluorite and the elements needed to produce fluorite would not exist at mantle depths. The possible fluorite grains in these samples were extremely small but appeared cubic and isotropic.

Inclusions

There were also some inclusion tracks visible in some samples. The tracks are of course very small and it would be very hard to determine if these were primary, secondary fluid inclusions, or melt inclusions. Some of these inclusions may be melt inclusions and that may represent the melt that was removed from the restite that became the xenolith. The samples

that seemed to have some inclusion tracks within some of the grains were PM-2, KH-1, EB-2, LCM-2, GCME-2, RPCN-1 & 2; and RPSR-1.

Deformation

Introduction

Deformational textures are signs that a rock has undergone a change in pressure or temperature regimes. In xenoliths that were expelled from depth this can include an increased pressure during expulsion and on impact with the surface of the crust but a xenolith can also show evidence of a decrease in pressure from the mantle pressure to atmospheric pressure. The temperature can also show either an increase during expulsion and a rapid decrease upon exposure to the atmosphere or the cool upper crustal zone. Deformation features can be readily used by fluids as conduits leading to alteration or the addition of secondary mineralization.

Deformational Banding

It is normal to expect to see signs of physical deformation in xenolith samples. Deformational banding that is the zones of finer grained minerals separating zones of average size grained minerals like that seen in sample RPSR-1. The finer grained zones are zones of recrystallization through increased pressure. Deformational banding is not to be confused with compositional banding that occurs during slow cooling when minerals are allowed to concentrate themselves with other similar or favorable minerals like in samples LCM-1, NVFTT-1 and others.

Long Axes Alignment

Long axes alignment seemed to be present in samples PM-2 and GVF-1. This type of alignment indicates pressure exerted perpendicular to the long axes, tensor motion moving parallel to the long axes, or that the minerals had sufficient time to cool and be affected by gravity to fall into their lowest potential energy level.

Decompressional Type Reaction Rims

The decompressional type reaction rims present in many of the samples is also a deformational texture. Decompression may occur during a lowering of pressure. The rims are present around olivine and pyroxene grains and seem to be the same mineralogy as the principle grain. The reaction rims seem to be in optical continuity however they appear to have some deformational alteration affecting them.

Fracturing

Fracturing is found in to styles in these samples either micro-fracturing or larger scaled fracturing. Micro-fracturing is small fracturing that is unique to a solitary grain and generally widespread throughout many of the samples. Micro-fracturing can lead to micro-veining if fluid flow allows for mineral precipitation to occur. Micro-fracturing can be caused by the quick cooling of xenoliths or upon impact with the crust. The larger scaled fracturing cross cuts grains and other features and appears to be latest occurrence of deformation. These fractures are used by fluids to form larger scaled veining through the precipitation of minerals.

Appendix C: Analytical Methods

Introduction

Seventeen samples were selected for chemical analysis based on their apparent lack of secondary mineralization and being of sufficient size to provide sample material for x-ray fluorescence (XRF), inductively coupled plasma mass spectrometry (ICP-MS), thin sections, and microprobe slabs. Major element analysis was done at XRAL Laboratories, Don Mills, Ontario via standard XRF spectrometry. Trace element analysis was done by the geochemical laboratory at the University of Saskatchewan (overseen by Qianli Xie) via ICP-MS on a Perkin Elmer Elan 5000 spectrometer.

X-Ray Fluorescence

Portions of each of the ground samples were sent for XRF analysis. XRF was done for the major elements. The process of XRF uses an x-ray beam to excite the atoms of the elements within a sample. The excited atoms emit secondary x-rays known as fluorescence whose characteristics are unique to each element (Rollinson, 1993). The instrumentation determines percentages of elements from collected secondary x-rays. The detection limits are given in Table 3.

ICP- Mass Spectrometry

The remainder of the ground samples was sent out for ICP-MS for trace element analysis. Dual sample preparation methods were preformed because samples that contain refractory minerals such as zircon and baddleylite that contain Zr and Hf (Xie

and Kerrich, 1995) may not dissolve completely by means of the HF-HNO_3 closed vessel dissolution (Xie, Pers. Commun., 2000). Data for HFSEs such as Zr, Nb, Y, Hf & Ta, as well as the REEs were collected using solutions made by Na_2O_2 sinter method. While the rest of the trace elements were collected using solutions produced by HF-HNO_3 method. The inductively coupled plasma mass spectrometry method extracts ions from a plasma state through a very small opening into a vacuum pumped system and focused into the mass spectrometer by means of an ion lens (Rollinson, 1993). The descriptions of methods that follow are based on information provided by Quanli Xie (by way of Frey, 2001).

Na_2O_2 Sinter Digestion Method

The Na_2O_2 sinter digestion method mixes 200 mg of each powdered sample with about 800 mg of ground Na_2O_2 in a dry, HCl washed nickel crucibles are subsequently heated to about 480°C for 1 1/2 hours in a muffle furnace. After being allowed to cool, each sample is then removed from this crucible by the addition of distilled de-ionized (DDI) water closely followed by scraping with a glass stirring rod. The resultant slurry is then centrifuged at 1750 rpm for 10 minutes and decanted. Centrifuging and decanting is repeated. 2 1/2 ml of 8N HNO_3 was added to every sample (in centrifuge tubes). Tubes were then allowed to sit in an ultrasonic water bath for 30 minutes. Any remnant solids were treated with ultra-pure oxalic acid, which wasn't allowed to react with solids for more then 3 hours. The sample batch included the samples, one blank, one reference standard, and one duplicate sample.

The reference standard material was MRG-1, an augite-olivine gabbro from Mount Royal in Montreal, Quebec.

HF-HNO_3 Closed-Vessel Digestion Method

The HF-HNO_3 closed-vessel digestion uses 100 mg of each powdered sample (weighed in Teflon beakers, which were washed with HNO_3 and heated HCl, then rinsed with ultra-pure water). Each sample was mixed with 1 ml of concentrated 16N HNO_3, also twice-distilled HF was added. Each sample with treatment was heated to 100°C for 3 days. If at this point a sample still bears any solids, the solution is dried and the process is repeated. Once all the solids are dissolved, each sample is evaporated, 2 ml of 8N HNO_3 is added and the resulting solution is heated for 30 minutes (then this last vaporization through heating process is repeated). The solution was allowed to cool and was then transferred to a 125 ml bottle and diluted to 80 – 100 g using DDI water and shaken. The sample batch included the samples, one blank, one reference standard (MRG-1), and one duplicate sample.

Calibration Solutions

As the samples were analyzed by ICP-MS, several calibration solutions were prepared and ran. Two external calibration standards were used 6 g each of STDA and STDB. Other calibration solutions included an unspiked samples consisting of 3.5 g sample and 3.5 g of 0.2N HNO_3; and spiked samples consisting of 3.5 g sample plus 3.5 g spike. Acid blanks contain 6 g of 0.2N HNO_3. Elemental concentrations for

standards are listed in Table 4. The run was concluded by the two standards plus DDI water blank.

Detection Limits and Reference Standard

Detection limits for trace elements (listed in Table 3) are specific for each element and are a measure of instrumental accuracy. The limits are determined based on the average acid blank values plus one standard deviation. The reference standard MRG-1 is an augite-olivine basalt from Mount Royal in Montreal, Quebec. The standard was run during both sample runs. Standard accepted values for MRG-1 come from Govindavaju (1994) and are compared to the values for MRG-1 from the University of Saskatchewan laboratory averages in order to determine this study's accuracy (Table 5).

Table 4: Elemental Concentrations for the Calibration Standards used in the ICP-MS Analysis (after Jenner et al., 1990)

Element	STDA (ppb)	STDB (ppb)	Spike (ppb)
Rb	200	200	
Ba	600		10000
Sr	600		10000
Th	100		1500
U	100		1500
Sc	200		
Y		100	
Zr	200		5000
Hf	100		
La	100		2000
Ce	100		
Pr	100		2000
Nd	400		4000
Sm	400		4000
Eu		200	
Gd		400	
Tb		100	
Dy		300	
Ho		100	
Er	200		2000
Tm	100		700
Yb	100		
Lu	100		

Table 5: Reference Standard MRG-1 Data

Element	MRG-1 (run 1) Analysis 1	Analysis 2	MRG-1 (run 2)	Standard Deviation	U of S Average	% RSD	Gorvindaraju (1994)
Rb	7.9	7.7		0.07	7.6	8	8.5
Ba	48	47		0.5	49	3	61
Sr	305	300		2.7	291	6	266
Th	1.14	1.05		0.045	0.89	11	0.93
U	0.25	0.29		0.020	0.26	10	0.24
Sc	56	62		2.9	61	8	55
Y	12.0	12.4	11.5	0.35	12.7	8	14.0
Zr	101	103	100	1.1	107	5	108
Nb	22	19	23	1.7	22	7	20
Hf	4.0	3.9	4.2	0.11	3.9	5	3.8
Ta	0.88	0.82	0.96	0.057	0.63	7	0.80
La	8.8	8.9	9.3	0.21	9.0	4	9.8
Ce	25	25	26	0.4	26	3	26
Pr	3.6	3.7	3.7	0.03	3.8	3	3.4
Nd	17.8	17.8	18.2	0.18	18.2	3	19.2
Sm	4.3	4.3	5.0	0.34	4.5	6	4.5
Eu	1.4	1.4	1.6	0.08	1.4	3	1.4
Gd	4.3	4.3	4.5	0.09	4.1	3	4.0
Tb	0.63	0.65	0.56	0.039	0.56	3	0.51
Dy	2.9	3.0	3.0	0.03	3.1	3	2.9
Ho	0.48	0.50	0.50	0.009	0.52	4	0.49
Er	1.17	1.22	1.19	0.021	1.23	4	1.12
Tm	0.15	0.14	0.14	0.005	0.15	5	0.11
Yb	0.82	0.79	0.85	0.024	0.85	5	0.60
Lu	0.14	0.14	0.15	0.005	0.11	6	0.12

References

Alibert, C.; Michard, A.; Albarede, F., 1986. Isotope and trace element geochemistry of Colorado Plateau volcanics. Geo. et Cosmo. Acta, 50: 2735- 2750

Baldrige, W.S., 1979. Mafic and ultramafic inclusion suites from the Rio Grande Rift (New Mexico) and their bearing on the composition and thermal state of the lithosphere. Jour. Vol. Geotherm. Res., 6: 319- 351

Bedini, R.M. & Bodinier, 1999. Distribution of incompatible elements between the constituents of spinel peridotite xenoliths: ICP-MS data from the East African Rift. Geo. et Cosmo. Acta, 63 No. 22: 3883-3900

Best, M.G., 1975. Migration of hydrous fluids in the upper mantle and potassium variation in calc-alkalinic rocks. Geology, 3: 429-432

Best, M.G., 1974. Contrasting types of chromium – spinel peridotite xenoliths in Basanitic lavas, Western Grand Canyon, Arizona. EPSL, 23: 229-237

Best, M.G., 1970. Kaerustite – Peridotite Inclusions and Kindred Megacrysts in Basanitic lava, Grand Canyon, Arizona. Contrib. Mineral. & Petrol., 27: 25-44

Best, M.G. & Brimhall, W.H., 1974. Late Cenozoic alkalic basaltic magmas in the western Colorado Plateau and the basin and range transition zone, U.S.A., and their bearing on mantle dynamics. GSA Bull., 85: 1677- 1690

Bodell, J.M. & Chapman, D.S., 1982. Heat flow in the north- central Colorado Plateau. JGR, 87: 2869- 2884

Bussod, G.Y. & Williams, D.R., 1991. Thermal and kinetic model of the southern Rio Grande rift : inferences from crustal and mantle xenoliths from Kilbourne Hole, NM. Tectonophys.,197: 373-389

Chapin, C. E., 1971. Rio Grande Rift, I. Modifications and additions. In: Guidebook to the San Luis Basin. NMGS Field Conf. Guidebook, 22: 191- 201

Chapman, D.S. & Pollack, H.N., 1977. Regional geotherms and lithospheric thickness. Geology, 5: 265- 268

Christiansen, R.L. & Lipman, P.W., 1972. Cenozoic volcanism and plate- tectonic evolution of the Western United States. II. Late Cenozoic. Phil. Trans. Roy. Soc. London, A271: 249-284

Condie, K.C., 1997. Plate Tectonics and Crustal Evolution. Butterworth Heinemann, GB

Condie, K.C., 1992. Poterozoic terranes and continental accretion in southwestern North American. In Proterozoic Crustal Evolution (ed. K.C. Condie) Ch. 12, pp. 447-480, Elsevier Sceint. Publishers, Amsterdam

Condie, K.C., 1982. Plate- tectonics model for Proterozoic continental accretion in the Southwestern United States. Geology, 10: 37- 42

Cross, T.A. & Pilger, R.H., 1978. Constraints on absolute motion and plate interaction inferred from Cenozoic igneous activity in the western United States. Amer. J. Sci., 278: 865-902

Ehrenberg, S., 1982. Petrogenesis of Garnet Lherzolite and Megacrystalline Nodules from the Thumb, Navajo Volcanic Field. J. Petrol., 23: 507-547

De Paolo, D.J., 1981. Neodynium isotope in the Colorado Front Range and crust- mantle evolution in the Proterozoic. Nature 291: 193- 196

Frey, F.A. & Green, D.H., 1974. The mineralogy, geochemistry and origin of lherzolite inclusions in Victorian basanites. Geochim. Cosmochim. Acta, 38: 1023- 1059

Frey, F.A. & Prinz, M., 1978. Ultramafic Inclusions from San Carlos, Arizona: petrologic and geochemical data bearing an their petrogenesis. EPSL, 38: 129-176

Green, D.H. & Wallace, M.E., 1988. Mantle metasomatism by ephemeral carbonatite melts. Nature, 336: 459- 461

Hawley, J.W. & Kottlowski, F.E., 1969. The Santa Fe Group in the south- central New Mexico border region. In: Border Stratigraphy Symposium, NMBMMR, Circular 104: 52- 67

Hoffer, J.M., 1976. The Potrillo basalt field, south- central New Mexico. NMGS. Spec. Pub., 5: 89- 92

Hoffer, J.M., 1975. The Aden- Afton basalt; Potrillo volcanics, south- central New Mexico. Texas J. Sci., 26: 380- 390

Hoffer, J.M., 1971. Mineralogy and petrology of the Santo Thomas- Black Mountain basalt field, Potrillo volcanics, south- central New Mexico. GSA Bull., 82: 603- 612

Hallet, R.B., 1992. Volcanic geology of the Rio Puerco Necks. NMGS Guidebook, 43rd Field Conf., pp. 135-144

Ionov, D.A.; Dupuy, C.; O'Reilly, S.Y.; Kopycova, M.G.; Genshaft, Y.S., 1993. Carbonated peridotite xenoliths from Spitsbergen: implications for trace element signature of mantle carbonate metasomatism. EPSL, 119: 283-297

Ionov, D.A.; Gregoire, M.; Prikhod'ko, V.S., 1999. Feldspar- Ti- oxide metasomatism in off-cratonic continental and oceanic upper mantle. EPSL, 165: 37-44

Ionov, D.A.; Hofmann, A.W.; Shimizu, N., 1994. Metasomatism- induced Melting in Mantle Xenoliths from Mongolia. J. Petrol., 35 part 3: 753-785

Jochum, K.P.; McDonough, W.F.; Palme, H.; Spettel, B., 1989. Compositional constraints on the continental lithospheric mantle from trace elements in spinel peridotite xenoliths. Nature, 340: 548-550

Kempton, P.D. & Dungan, M.A., 1989. Geology and petrology of basalts and included mafic, ultramafic, and granulitic xenoliths of the Geronimo Field, SE Arizona. NMBMMR, Memoir 46: 161-172

Kempton, P.D.; Harmon, R.S.; Hawkesworth, C.J.; Moorbath, S., 1990. Petrology and geochemistry of lower crustal granulites from the Geronimo Volcanic Field, SE Arizona. Geochim. & Cosmochim. Acta, 54: 3401- 3426

Kempton, P.D.; Menzies, M.A.; Dungan, M., 1984. Petrography, petrology and geochemistry of xenoliths and megacrysts from the Geronimo Volcanic Field, southeastern Arizona. In: Kimberlites II: Mantle and Crust- Mantle Relationships (ed. J. Kornprobst). pp. 71- 83. Elsevier

Kepezhinskas, P.K.; Defant, M.J.; Drummond, M.S., 1995. Na metasomatism in the island arc mantle by slab melt – peridotite interaction. J. Petrol., 36: 1505-1527

Laughlin, A.W. & Charles, R.W., 1992. Lamprophyric dikes of the Navajo Volcanic Field. In: Western Slope Conf. Field Guide pp. 41 – 47. Four Corners, Navajo Community College, Shiprock, NM

Lee, C.T.; Yin, Q.; Rudnick, R.L.; Jacobsen, S.B., 2001. Preservation of ancient and fertile lithospheric mantle beneath the SW US. Nature, 411: 69-73

Livacarri, R.F. & Perry, F.V., 1993. Isotopic evidence for preservation of Cordilleran lithospheric mantle during the Sevier-Laramide Orogenywestern United States. Geology, 21, 719-722

Mattie, P.D.; Condie, K.C.; Selverstone, J.; Kyle, P.R., 1997. Origin of the continental crust in the Colorado Plateau: geochemical evidence from mafic xenoliths from the Navajo Volcanic Field, SW USA. Geochim. & Cosmochim. Acta, 61: 2001-2021

Menzies, M.A.; Rogers, N.; Tindle, A.; Hawkesworth, C.J., 1987. Metasomatic and enrichment processes in lithospheric peridotites, and effect of athenosphere- lithosphere interaction. In Mantle Metasomatism (ed. M.A. Menzies & C.J. Hawkesworth), pp. 313-361, Academic Press, San Diego, CA

Menzies, M.A.; Kempton, P.D.; Dungan, M.A, 1985. Interaction of continental lithosphere and athenospheric melts below the Geronimo volcanic field, Arizona.
J. Petrol., 26: 663-693

Mercier, J.C.C., 1977. Natural Peridotites: Chemical and Rheological Heterogeneity of the Upper Mantle. PhD Thesis. State Univ. of New York at Stony Brook, Stony Brook, N.Y. 669pp

Olsen, K.H.; Baldridge, W.S.; Callender, J.F., 1987. Rio Grande rift: an overview. In: Continental Rifts- Principal and Regional Characteristics. Tectonophys. 143: 119- 139

O'Reilly, S.Y. & Griffin, W.L., 2000. Apatite in the mantle: implications for metasomatic processes and high heat production in the Phanerozoic mantle. Lithos. 53: 217-232

O' Reilly, S.Y.; Griffin, W.L.; Ryan, C.G., 1991. Residence of trace elements in metasomatized spinel lherzolite xenoliths: a proton microprobe study.
Contrib. Mineral. Petrol., 109: 98-113

O'Reilly, S.Y. & Griffin, W.L., 1988. Mantle metasomatism beneath Victoria, Australia I: metasomatic processes in Cr- diopside lherzolites. Geochim. Cosmochim. Acta. 52: 433-447

Padovani, E.R. & Carter, J.L., 1977. Aspects of the deep crustal evolution beneath south central New Mexico. Am. Geophys. Union Mon., 20: 19-55

Padovani, E.R. & Reid, M., 1989. Field guide to Kilbourne Hole maar, Dona Ana County, New Mexico. In: From Silicic Calderas to Mantle Nodules: Cretaceous to Quaternary Volcanism, Southern Basin and Range Province, Arizona and New Mexico (ed.s J. Pallister & D. Sawyer), NMBMMR Mem. 46: 174- 179

Pazzaglia, F.; Woodward, L.; Lucas, S.; Anderson, O.; Wegman, K.; Estep, J., 1999. Phanerozoic Geologic Evolution of the Albuquerque Area. NMGS Guidebook, 50th Field Conference. Albuquerque Geology

Perry, F.V.; Baldrige, W.S.; De Paolo, D.J.; 1988. Chemical and isotopic evidence for lithospheric thinning beneath the Rio Grande Rift. Nature. 332: 432- 434

Pike, J.E. Neilson, 1976. Pressures and temperatures calculated from Chromium- rich pyroxene compositions of megacrysts and peridotite xenoliths, Black Rock Summit, Nevada. Jour. Geol., 61: 725- 731

Reeves, C.C. & de Hon, R.A., 1965. Geology in Potrillo maar, New Mexico and northern Chihuahua, Mexico. Amer. J. Sci., 263: 401- 409

Reid, J.B. & Woods, G.A., 1978. Oceanic mantle beneath the southern Rio Grande rift.

EPSL, 41: 303-316

Roden, M.F. & Shimizu, N.S., 1993. Ion microprobe analyses bearing on the composition of the upper mantle beneath Basin and Range and Colorado Plateau Provinces. JGR, 98: 14091-14108

Roden, M.F.; Smith, D.; Murthy, V.R., 1990. Chemical constraints on lithosphere composition and evolution beneath the Colorado Plateau. JGR, 95 No. B3: 2811-2831

Roden, M.F.; Irving, A.J.; Murthy, V.R., 1988. Isotopic and trace element composition of the upper mantle beneath a young continental rift: results from Kilbourne Hole, NM.

Rudnick, R.L., McDonough, D.A., Chappel, B.W., 1993. carbonatite Metasomatism in the Northern Tanzanian Mantle: petrographic and geochemical characteristics. EPSL 114: 463-475

Rudnick, R.L., 1992. Xenoliths – samples of the lower continental crust. In: Continental Lower Crust (ed.s D.M. Fountain; R. Arculus; R.W. Kay) pp. 269-316, Elsevier

Scherer, E.E.; Cameron, K.L.; Jonhson, C.M.; Beard, B.L.; Barovich, K.M.; Collerson, K.D., 1997. Lu- Hf geochronology applied to dating Cenozoic events affecting lower crustal xenoliths from Kilbourne Hole, New Mexico. Chem. Geol. 142: 63- 78

Scott, D.H.; Trask, N.J., 1971. Geology of Lamar Crater volcanic field, Nye County, Nevada. USGS Prof. Paper, 599- I: I1- I22

Scott, D.H., 1969. The geology of the southern Pancake Range and the Lunar Crater volcanic field, Nye County, Nevada. PhD thesis. Univ. of California, Los Angeles, Ca. 127 pp

Seager, W.R. & Morgan, P., 1979. Rio Grande rift in southern New Mexico, west Texas, and northern Chihuahua. In: The Rio Grande Rift: Tectonics and Magnatism (ed. R.E. Rieker) . pp. 87- 106. AGU

Smith, D. & Boyd, F.R., 1989. Compositional heterogeneities in minerals of sheared lherzolite inclusions from African kimberlites. In: Kimberlites and Related Rocks, Vol. 2. Their Mantle / Crust Setting, Diamonds and Diamond Exploration (ed. S.Y. O'Reilly). Spec. Pub., Geol. Soc. Of Australia, 14: 429-432

Smith, D. & Levy, S., 1976. Petrology of the Green Knobs diatreme and implications for the upper mantle beneath the Colorado Plateau. EPSL, 116: 23-43

Sun, S.S. & McDonough, W.F., 1989. Chemical and isotopic systematics of oceanic basalts: implications for Mantle composition and processes. In: Magmatism in the ocean basins (ed.s A.D. Saunders & M.J. Norry), Geol. Soc. London. Spec. Pub., pp. 313- 345

Thompson, G.A. & Zoback, M.L., 1979. Regional geophysics of the Colorado Plateau. Tectonophys., 61: 149- 161

Trask, N.J., 1969. Ultramafic xenoliths in basalt, Nye County, Nevada. USGS Prof. Paper 650-D: D43-D48

Walter, M.J., 1999. Melting residues of fertile peridotite and the origin of crtonic lithosphere. Mantle Petrology: Field Observations and High Pressure Experimentation. Ed.s Fei, Y.; Bertka, C.M.; Mysen, B.O., The Geological Society, Spec. Pub. No. 6

Watson, E.B.; Brenan, J.M.; Baker, D.R., 1990. Distribution of fluids in the Continental Mantle. In: Continental Lithosphere (ed. M.A. Menzies). Pp. 111- 125, Claredon, Oxford

Weichert, U., Ionov, D.A., Wedepohl, K.H., 1997. Spinel peridotite xenoliths from Atsagin-Dush volcano, Darianga lava plateau, Mongolia: a record of partial melting and cryptic metasomatism in the upper mantle. Contrib. Mineral. Petrol. 126: 345- 364

Wilshire, H.G., et al., 1988. Mafic and ultramafic xenoliths from volcanic rocks of the western United States. USGS Prof. Paper 1443

Wood, D.A., 1979. A variably veined suboceanic upper mantle- genetic significance for mid-ocean ridge basalts from geochemical evidence. Geology 7: 499-503